UC San Diego
UC San Diego Electronic Theses and Dissertations

Title

Spectral and Spatial Light Field Encoding for Tissue Imaging, Drug Delivery and Focused Field Shaping

Permalink

https://escholarship.org/uc/item/8wc3j8gs

Author

Baghdadchi, Saharnaz

Publication Date

2017

Peer reviewed|Thesis/dissertation

UNIVERSITY OF CALIFORNIA, SAN DIEGO

Spectral and Spatial Light Field Encoding for Tissue Imaging, Drug Delivery and Focused Field Shaping

A dissertation submitted in partial satisfaction of the
requirements for the degree
Doctor of Philosophy

in

Electrical Engineering (Photonics)

by

Saharnaz Baghdadchi

Committee in charge:

Professor Sadik C. Esener, Chair
Professor Michael Berns
Professor Mohammad Eghtedari
Professor Michael Heller
Professor Zhaowei Liu
Professor Yu-Hwa Lo

2017

The dissertation of Saharnaz Baghdadchi is approved, and it is acceptable in quality and form for publication on microfilm and electronically:

_____

_____

_____

_____

_____
Chair

University of California, San Diego

2017

To my husband, who has been by my side through life's ups and downs.

To my son, who made me proud at every stage of his life.

To my father, who taught me to never give up, no matter how hard

achieving my goals appeared to me.

To my mother, who was always there for me whenever I needed her no

matter how far away she was from me.

EPIGRAPH

It's Not That I'm so Smart, It's Just That I Stay with Problems Longer.

—Albert Einstein

TABLE OF CONTENTS

LIST OF FIGURES

LIST OF TABLES

ACKNOWLEDGEMENTS

I am very grateful for the opportunity to work with many talented and inspiring individuals during my PhD program at UC San Diego. Each one of these people supported me beyond my expectation.

First and foremost, I would like to thank Professor Sadik Esener for believing in me and giving me the opportunity to work in his lab. His passion toward finding new solutions to scientific problems is truly inspiring and he conveys this passion to his students especially during the group meeting discussions. His composure and patience is remarkable and he always finds a way to inspire and encourage his students even in the midst of difficult situations.

I am grateful to Professor Michael Heller for his valuable lectures and insightful discussions. I appreciate that he always made the time to stop by my office and ask if I need help with anything. I learned a lot from our discussions and more importantly, was inspired by his enthusiasm toward exploring the science.

I would like to thank Professor Michael Berns for his support and valuable advice on my projects. I appreciate his willingness to answer my questions at different stages of my graduate program. His expertise and guidance has been an important resource for me.

Professor Zhaowei Liu deserves special gratitude for being a supportive member of my committee. His valuable suggestions and comments on my projects have been very helpful in shaping the direction of my projects.

Professor Yu-Haw Lo has my sincere appreciation for his support and sharing his unique perspective and expertise in bio-optical experiments with me. I appreciate his attention to the details of my projects and his helpful feedback.

Dr. Mohammad Eghtedari has my utmost appreciation. I had the privilege of working with him since the early years of my PhD program. He always found the time to meet with me and help me in interpreting the research results. We had many discussions

I have been lucky to work with two bright undergraduate students, Anup Tank and Zijun Chen. They helped me in the lab with my imaging and optical trapping experiments. I enjoyed running those experiments and discussing the results with them. The questions that they asked truly challenged me to better understand the physics behind our observations.

I am grateful to Professor George Papen for keeping his door open to me for our several optics related discussions. I admire him as a passionate professor who is willing to share his knowledge and expertise with the students. I appreciate that he trusted me enough to hire me as the Teaching Assistant for his Lasers and Modulators course. It was the starting point of my journey of teaching undergraduate courses.

Dr. Peter Ilinykh deserves much recognition for helping me set up optical experiments in the undergraduate photonics labs and for sharing his expertise and experience with me.

I would like to thank Professor Joseph Ford for several discussions that we had about my 3D imaging project. He kindly shared his expertise and insights with me and patiently answered all my questions.

Professor Quest deserve special recognition. I appreciate his support and encouragement through my teaching endeavors. He provided a support letter for my nomination for the Graduate Teaching Scholarship and trusted me enough to ask me to continue his summer course in his absence.

I am grateful to Professor Paul Siegel for giving me the opportunity to help the students in his course for two quarters as his Teaching Assistant. I also appreciate his confidence in the results of my teaching experience and implementing the Peer Instruction using clicker questions in his course.

Dr. Robert Mattrey deserves recognition for his advice and guidance in the areas of radiology, bio-imaging and tissue biopsy. I appreciate his feedback and edits on our

joint paper.

I am grateful to Dr. Joe Carson for always making the time to meet with me both in-person and virtually. He never hesitated to teach me the image processing algorithms. I had the pleasure of closely working with him on the 3D imaging project.

I would like to thank Professor Pamela Cosman for mentoring me through the PRIME program and for the discussions that we had about my future research and teaching plans. I appreciate her tremendous support and guidance.

I also would like to thank Professor Tina Ng, Professor Duygu Kuzum and Professor Farinaz Koushanfar, the Graduate Women in ECE (WeCe) faculty advisors. They were my role models and went out of their way to help me and my team to organize the WeCe events during the past couple of years.

I am grateful to Dr. Peter Newberry for all scholarly teaching workshops and classes that he held for us during the Summer Graduate Teaching Scholars Program. I also appreciate his guidance and insights in my Teaching as Research project. Erilynn T Heinrichsen, Emily Grossman and Tiffany Dunbar deserve recognition for their support during my summer teaching assignment. I appreciate their help with designing surveys for my class and our discussions at the summer reflection sessions.

I am grateful to my other colleagues and friends at UCSD including Somayeh Imani, Hannah Grant, Lorraine Hossain, Najme Ebrahimi, Sonika Osborn, Alex Zhang, David Hall, Anna Bezryadina, Julian Ramirez, Daniel Rodriquez, Benjamin Sarno and many others. I appreciate their support, research and career advice and all the conversations and laughter we had together.

I appreciate the ECE and Nanoengineering departments staff members for helping me in many instances during my PhD program. I would like to thank Eric Lara, Shana Slebioda, Charmaine Samahin-Manns, Kacy Vega, Dimple Bhatt, Christopher Shenton, Mary Duarte, Myda Prado, Stefanie Battaglia, Dana Jimenez, Ji Song and many others.

Finally, I would like to thank my husband, son, Mom, Dad and sister for their continuous support and encouragement throughout my education. Their confidence in me and support of my interests made a big difference in my life.

2005	B. S. in Electrical Engineering *Control*, University of Tabriz, Iran
2008	M. S. in Electrical Engineering *Electronic Devices*, Azad University, Iran
2012-2017	Graduate Teaching Assistant, University of California, San Diego
2016	Associate-In Lecturer, University of California, San Diego
2017	Ph. D. in Electrical Engineering,*Photonics*, University of California, San Diego
2017	Assistant Teaching Professor in the Electrical and Computer Engineering department, University of California, San Diego

PUBLICATIONS

Baghdadchi, Saharnaz; Liu, Kimberly; Knapp, Jacquelyn ; Prager, Gabriel ; Graves, Susannah ; Akrami, Kevan ; Manuel, Rolanda ; Bastos, Rui ; Reid, Erin ; Carson, Dennis; Esener, Sadik; Carson, Joseph; Liu, Yu-Tsueng., "An innovative system for 3D clinical photography in the resource-limited settings", *Journal of translational medicine*, 12, 2014.

Baghdadchi, Saharnaz; Esener, Sadik; Mattrey, Robert; Eghtedari, Mohammad. "Fiber sensor assisted in-vivo needle guidance for minimally invasive procedures"

Schutt, Carolyn; Baghdadchi, Saharnaz; Ibsen Stuart;Esener, Sadik. "Detection and activation of a light activatable prodrug using a dual fiber optic System"

Baghdadchi, Saharnaz; Preece, Daryl; Esener, Sadik. "Fast Vectorial Incident and Focused Field Calculations with High NA Lenses"

Baghdadchi, Saharnaz; Preece, Daryl; Esener, Sadik. "Imaging through scattering using spatially encoded optical beams"

Baghdadchi, Saharnaz. "Effect of Peer Instruction, Guided Pre-Reading and Post-Lecture Assignments on Engineering Students' learning "

ABSTRACT OF THE DISSERTATION

Spectral and Spatial Light Field Encoding for Tissue Imaging, Drug Delivery and Focused Field Shaping

by

Saharnaz Baghdadchi

Doctor of Philosophy in Electrical Engineering (Photonics)

University of California, San Diego, 2017

Professor Sadik C. Esener, Chair

Optical signatures of the biological tissues and spectral characteristics of the chemotherapy agents provide distinctive information on the nature of these tissues and the chemical properties of the chemotherapy drugs delivered at the tumor sites. Equipping the tools routinely used in interventional procedures, with optical guidance could provide real-time feedback on the characteristics of the tissues and the drugs under examination by acquiring and evaluating their spectral information. A new optically guided needle system is designed here that transmits the spectrally encoded modulated light to the medium at the tip of the needle and processes the detected backscattered light to sense

the presence of the blood or bile within the liver parenchyma, differentiate the benign and malignant breast tissue, activate a photocleavable prodrug and estimate the amount of the drug accumulated at the tumor site.

In addition to spectral imaging of the tissues, spatially encoded light fields were used to generate images of the objects hidden within scattering materials and methods were proposed to calculate and generate the desired spatially encoded vectorial fields at the focus of high NA lenses. The results of the imaging through scattering experiments showed that utilizing the designed set of spatially encoded projection patterns significantly reduced the number of measurements required to reconstruct an image of the hidden objects. The developed reflective imaging setup is compatible with the majority of the bio-imaging settings.

To generate the desired spatially encoded vectorial light fields at the image plane of the high NA lenses, a new method was proposed to calculate the required incident fields with spatially varying polarizations in the back focal plane of the lenses. With the refresh rate of 40 Hz for calculating 128×128-pixel incident fields, this method could be used to update and adjust the designed focused fields in near real time. The application of this method in generating line traps for imposing translational movement on the trapped particles was also discussed.

Chapter 1

Fiber sensor based needle biopsy guidance and drug delivery monitoring

1.1 Fiber sensor assisted in-vivo needle guidance for minimally invasive procedures

Abstract

Interventional Radiologists use image guidance, commonly x-ray fluoroscopy or computed tomography, to insert a needle into a target, such as tumor, fluid collection, or to gain access to the lumen of vessels or ducts. When targeting vessels or ducts in the liver, the location of the needle tip as it is advanced is determined by injecting small quantities of contrast material. We have designed an optically guided needle system that constantly interrogates the optical signature of tissue in the immediate vicinity of the tip to provide real-time feedback minimizing radiation exposure and eliminating the need for contrast media injections during some of the commonly used interventional procedure. Our system replaces the steal needle core with transmitter and receiver fiber cables to

deliver a low power modulated light to the needle tip and capture the backscattered light to determine the tissue's optical properties. A prototype was tested using a cow's liver, ex vivo. We were able to not only determine when the needle tip was in liver parnechyma, blood vessel, or bile duct based on their optical signature in real time, but also determine the tissue type a few millimeters ahead of the needle tip.

1.1.1   Introduction

Interventional radiologists use real-time imaging to guide small needles, wires, and tubes within the body to perform a variety of procedures such as biopsies, drainage of a fluid collections, or accessing vessels to place stents [3]. The challenge in these procedures is to identify whether the needle tip is within the target space. Identifying the exact location of the needle tip may be difficult, particularly when aiming for small targets, lengthening the procedure, increasing radiation exposure to the patient and medical personnel when using x-ray fluoroscopy or computed tomography for guidance, and increased risk of injury to intervening tissues.

Percutaneous Biliary Drainage (PBD) is one of the common procedures that is performed to decompress the biliary system that is obstructed by tumor, stone or scarring [4]. During PBD, the interventionalist inserts a thin needle percutaneously into the liver and uses x-ray fluoroscopy to guide the needle into a bile duct. To identify the location of the needle tip, iodinated contrast media is continually injected and the pattern of contrast diffusion assessed until the biliary tree is identified. Once in the duct, the steal needle core is exchanged with a guide wire that is advanced into the bile duct and used as a guide to advance a drainage tube. The challenge is recognizing when the needle tip is in a bile duct especially when ducts are small, or when the field of view becomes obscured by contrast media from previously failed passes.

The biochemical components and structure of tissues determine their optical

properties, allowing their recognition by assessing light absorption and scattering coefficients, anisotropy factor, and index of refraction. Several investigators have shown the feasibility of performing an optical tissue biopsy using a fiber optic core inside a needle. Lubawy and Ramanujam developed a fiber-optic based biopsy probe for near-infrared spectroscopic sampling of in vivo breast tissues [5]. Stephen A. Boppart, et al. [6] used near-infrared fiber optics integrated breast biopsy needle to perform tissue classifications based on measurement of the optical refractive index and scattering. Irving J. Bigio, et al. [7] provided an extensive review of common methods of diagnostic optical spectroscopy that were translated to the clinic to aid gastrointestinal endoscopy, as well as detection of breast and cervical cancer.

In this project, we performed a series of Monte Carlo simulations to determine whether optical spectroscopy would provide a unique signature for liver parenchyma, blood and bile, the three tissues encounter during PBD. We then built a prototype system using the needle that is commonly used for PBD, and replaced the core with 2 fibers to transmit and receive light. We then tested the system using a cow's liver, blood and bile, ex vivo. We not only show that optical spectroscopy successfully recognizes the three tissue types at the needle tip, but also recognizes when the needle tip is approaching bile or blood a few millimeters before the interface is reached.

1.1.2   Methods and materials

Mathematical Simulation

In our model, the propagation of photons inside the target tissue and the amount of backscattered light were simulated using the Monte Carlo method. We used an open source software offered by Lihong Wang and Steven L. Jacques [8], and assumed that the tissue is cylindrically symmetrical, has a radius of 10 mm and depth of 4 mm and

calculated the photon fluence map as a function of radius (r) and depth (z) (Figure 1.1). We used two 200 *μm* fibers separated by 50 *μm* and calculated the diffused reflectance, R(r), as the number of photons reaching each grid point along the surface of the detection fiber.

To test the hypotheses that backscattered light from bile, blood, and liver provides unique optical signatures to allow their recognition, we performed three simulations one at each wavelengths (R(λ)) of 520, 630, or 700 nm and calculated diffuse reflectance. We used the tissue properties reported by Ritz, et al.[9] and Faber, et al.[10] for the simulations.
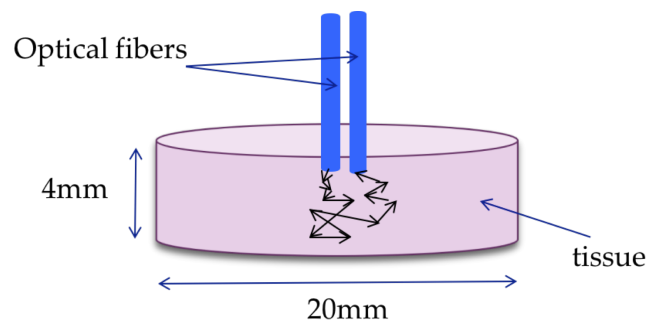
Figure 1.1: Schematic of the model used for the Monte Carlo simulation.

To test whether the system can recognize that a different tissue lies ahead and at what distance (the Look Ahead Distance (LAD) as defined by Hanli Liu et al.[11]), we used a two-layer model with the liver as the current tissue and the layer ahead is either blood or bile. Monte Carlo simulations were performed as the tissue, 4mm ahead, was changed from all liver to all blood or bile in graded increments, and the absorption spectrum and diffused reflectance for each condition calculated. For the simulations we used a 4mm cylindrical tissue model and 520 nm wavelength.

Needle Assembly

The prototype fiber sensor based biopsy needle consisted of two optical fiber cables with 200 μm core diameter and 0.22 numerical aperture (FG200UEA, Thorlabs) inserted in a standard 15 cm 20-gauge biopsy needle (BD 405211 Quincke Spinal Needle, 600 μm inner diameter). After removing the buffer and coating of two optical fibers, they were inserted into the needle, and under microscopy guidance, black epoxy (J-B Weld KwikWeld, www.homedepot.com) was used to fix the tips at 50 μm apart and to eliminate light cross-contamination. One of the fibers was used to transmit and the other to receive backscattered photons that were captured by a detector (Ocean-Optics spectrometer USB4000) for analysis.

Tissue Phantom Experiments

Cow's liver and goat's blood were purchased from a local grocer. Bile phantom was made by adding green color to a diluted milk solution. Using the needle system just constructed, xenon light was delivered through one optical fiber when the tip was inserted in each of the three tissues. The received optical signal was used to generate a spectrum to identify distinct bands for liver, blood, and bile. We then constructed look-up tables for the ratio of backscattered light intensity at each of the characteristic bands for each pair of tissues. To normalize the collected intensities, we used the ratio of the backscattered light at two wavelengths instead of using an absolute value of backscattered light.

Since data from the xenon light indicated that the three tissues can be recognized by interrogating at only 520 and 630 nm, the remaining experiments were performed using low power red and green laser diodes with center frequencies at 671 and 532 nm, respectively (Quartet Classic Comfort Laser Pointers, www.walmart.com). The two laser diodes were controlled by a custom current driver circuit connected to a propeller microcontroller (www.parallax.com), combined using a long pass dichroic

mirror at 605 nm cutoff frequency (DMLP605T, www.thorlabs.com), and coupled to the transmit fiber in the needle system. Collected backscattered light was measured using a PIN photodiode (OPF480, Optek Technology Inc.), amplified by an op-amp based integrating amplifier (IVC102, Burr-Brown), captured by a sample and hold circuit (LF198, National Semiconductor Corporation), converted to a digital output (MCP3202, Microchip Technology Inc., Chandler, Arizona), which was used by the propeller microcontroller to modulate the two laser diodes output and the reset/read integration circuit (Figure 1.2). Spin software was used to program the two lasers as follows: turn on one diode, wait 50 ms for stabilization, reset the integration circuit, integrate the subsequent backscattered photons for 0.3 ms, set the sample and hold circuit to update the signal level, turn off the diode, digitize the sample/hold signal level, transmit the result to the computer and repeat the same steps for the second diode. The exception is that the integration time was shortened to 0.1 ms for the red light because of the larger backscattered signal. Data was collected for 500 ms as the needle system was inserted in each of the three tissues and the ratios of backscattered red and green signal calculated.
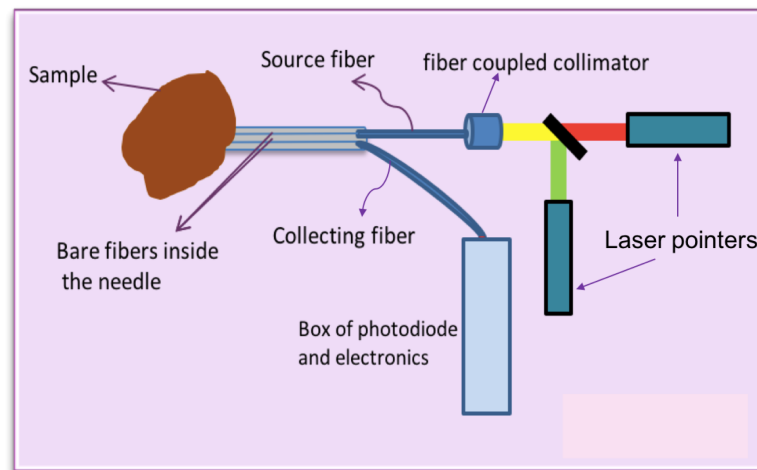
Figure 1.2: Needle system and electronic setup.

For the LAD experiments, we filled one of the clearly visible veins inside the

cows liver with blood, mounted the needle system on a micro positioning stage and placed its tip inside the liver, and slowly advanced it towards the vein, punctured and went through the vein back into the liver. To simulate advancing towards a bile duct, we placed two liver slices near each other and filled the space in between with simulated bile and performed the same experiment as above. The ratio of red to green backscattered signal was recorded in both experiments.

1.1.3 Results

Monte Carlo Simulations

The single layer Monte Carlo simulation shows different fluence maps backscattered from liver, blood, and bile at 520nm, 630 nm and 700 nm (Figure 1.3). Note that each tissue shows a different pattern at each wavelength.
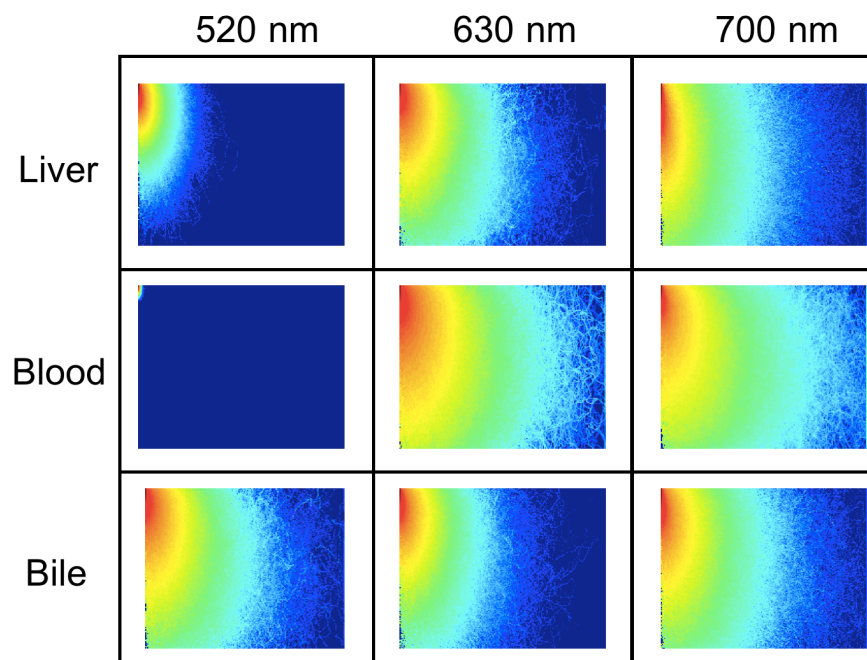
Figure 1.3: Simulation generated fluence maps for the liver, blood, and bile at 520, 630, and 700 nm.

When the ratios of signals at each pair of wavelengths were calculated for each tissue (Table 1.1), blood had the lowest at R(520 nm)/R(630 nm) and liver at R(700 nm)/R(630 nm), while bile has the highest at R(520 nm)/R(630 nm). Note that the ratio of signals received at 520 and 630 nms relative to liver are 2.37 and 75.77 times greater for blood and bile, respectively.

Table 1.1: Simulated reflectance ratio for blood, liver, and bile for each wavelength pair.

	R(520)/R(630)	R(520)/R(700)	R(700)/R(630)
Blood	0.0539	0.0569	0.947
Liver	0.0227	1.02	0.0221
Bile	1.72	1.43	0.705

The LAD as defined by Hanli Liu et al.[11] is the distance when the probing tip can recognize an approaching interface of a different tissue. We defined the LAD as the distance when reflectance normalized to the underlying tissue decreased by 2 standard deviations from baseline. The dual layer Monte Carlo simulation fluence maps when the needle tip is advancing within the liver and approaching blood is shown in Figure 1.4. Note the dramatic change as the needle tip approaches the blood interface allowing the recognition of its impending puncture, which is best appreciated when signal normalized to liver and plotted as a function of distance from the interface (Figure 1.5). The LAD for an approaching blood interface was 200 μm.

In-vitro Experiments

Using the needle system illuminated with a xenon light source, distinct full absorption spectra were observed for the liver, blood, and bile (Figure 1.6). Based on the Monte Carlo simulations and this spectral data three wavelengths were selected 520 nm and 630 nm when bile and blood are different, and 700 nm when all three
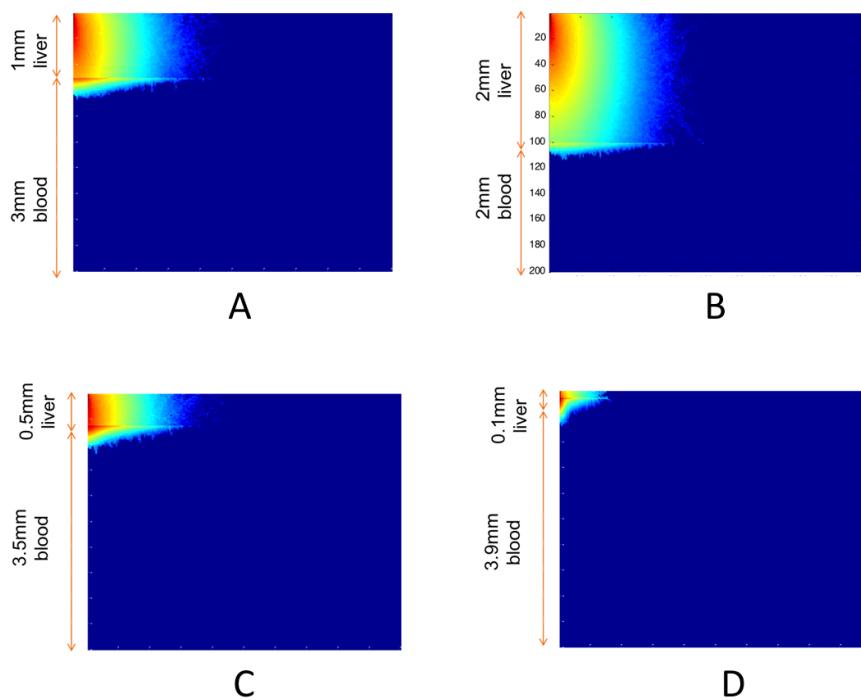
Figure 1.4: Simulation generated fluence maps for the liver, blood, and bile at 520, 630, and 700 nm.

tissues are similar and calculated absorption ratios (Table 1.2). Similar to the simulation, experimental results also allowed the distinct recognition of blood and bile from liver. Note however, that the ratio of blood signals received at 520 and 630 nms is 22.65 time smaller, and bile 56.99 times greater than liver, and nearly 3 orders of magnitude greater for bile than blood.
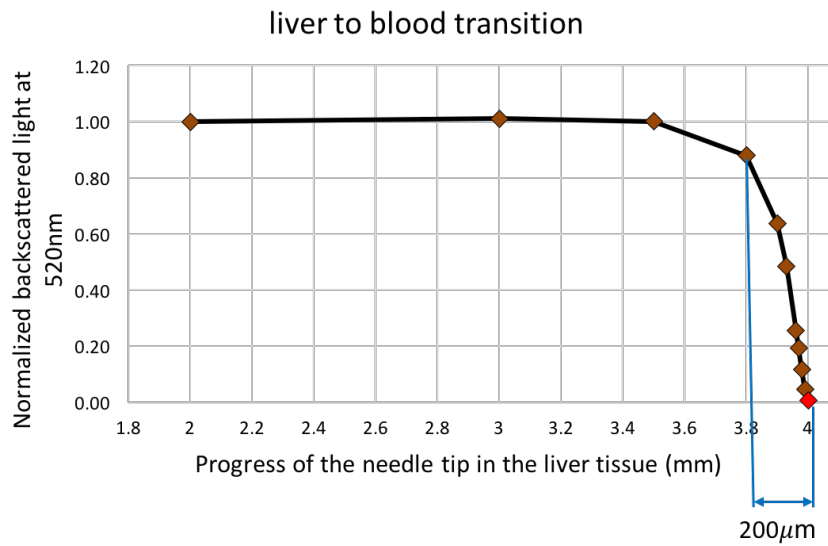
Figure 1.5: Intensity normalize to liver at 520nm as the needle tip is approaching a blood interface.
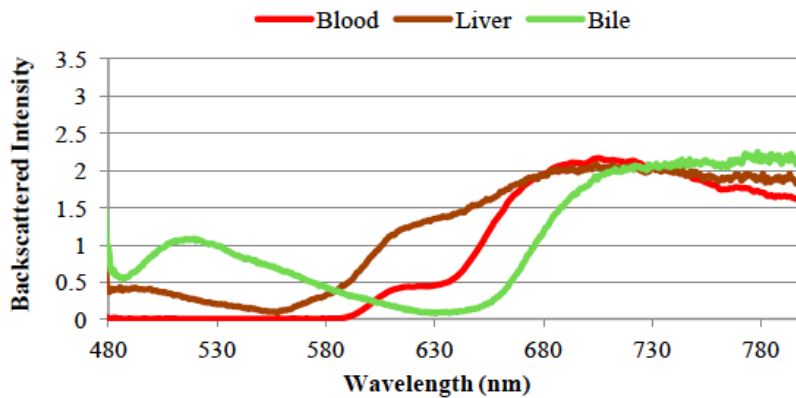
Figure 1.6: Spectra of backscattered light in liver, blood and bile phantom.

Table 1.2: Measured ratios for blood, liver, and bile for each wavelength pair.

	R(520)/R(630)	R(520)/R(700)	R(700)/R(630)
Blood	0.008725	0.001871	4.662362058
Liver	0.197623	0.132811	1.488004158
Bile phantom	11.26195	0.587519	19.16864188

Using the needle system illuminated with the red and green laser diodes, the ratio of the red to green backscattered lights were recorded when the needle was placed in the liver, blood or bile (Figure 1.7). Note that blood had the highest ratio, which was 10 times larger than the case in liver and 200 times larger than the case in bile.

Intensity ratio of red to green backscattered photons in different samples
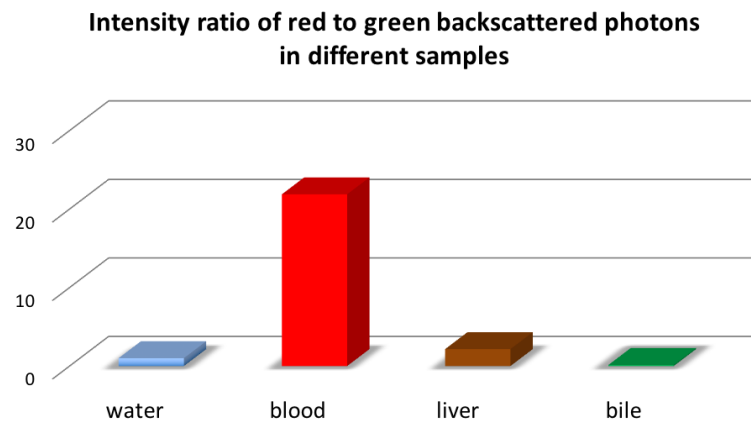
Figure 1.7: Ratio of red to green backscattered light intensities for the liver, blood, bile, or water.

The backscattered red to green signal ratio was recorded as the needle was mechanically advanced from liver into and through blood, or into and through bile are shown in Figure 1.8. Note again, that the ratio for blood is very high relative to liver, while bile was approximately 4.5 times lower. However, as the needle advanced from liver to blood the ration increased, and when it entered bile the decreased allowing their clear distinction.

A

Intensity ratio of red to green backscattered light in liver to blood to liver transition

red/ green intensity ratio

100
80
60
40
20
0

Liver ⟹ Blood ⟹ Liver

B

Intensity ratio of red to green backscattered light in liver to bile to liver transition

red/ green intensity ratio

2
1.5
1
0.5
0
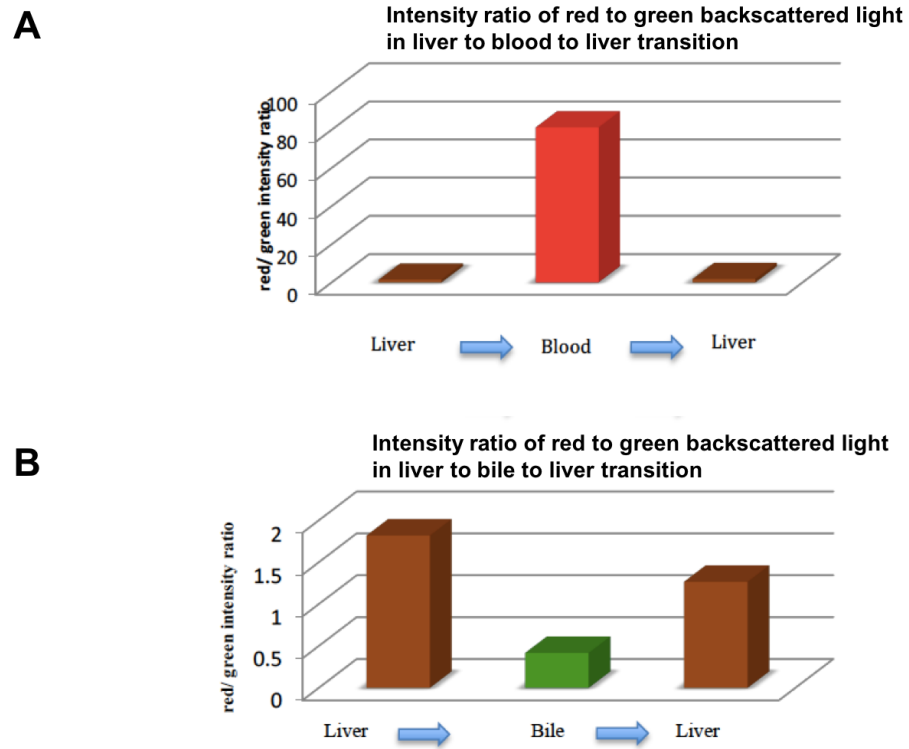
Liver ⟹ Bile ⟹ Liver

Figure 1.8: The ratio of red to green backscattered signal are shown as the needle tip was advanced through the liver into and through blood (**A**) and into and through bile (**B**).

To assess the LAD as the needle was advanced from liver to blood or bile, the red to green signal ratio recorded continuously and normalized to the liver signal was plotted as a function of distance from the approaching interface and shown in Figure 1.9. The LAD was 3.5 and 8 mm for blood and bile respectively (Figure 1.9).
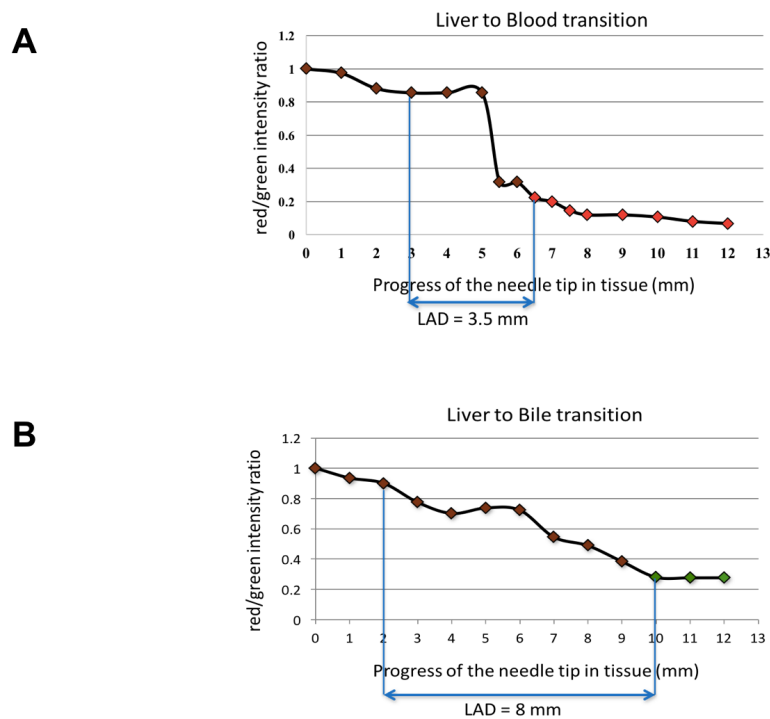
Figure 1.9: The ratio of red to green backscattered signal are shown as the needle tip was advanced through the liver into blood **(A)** and into bile **(B)**. The LAD is shown as the band during which there was a change equal to 2 standard deviations from baseline.

1.1.4 Conclusions

The Monte Carlo simulations and experimental data were concordant. They showed that liver, bile and blood have distinct backscatter spectra allowing their distinction. Using alternating red (671 nm) and green (532 nm) light laser diodes our prototype needle system was able to specifically distinguish the three tissue types at the needle tip. More important, the ratio allowed the recognition and distinction of an approaching interface with blood or bile at 3.5 and 8 mm, respectively. This system can be further refined by use of a laser diode closer to 630 nm and a device that can steer the needle away from blood vessels and towards bile ducts during percutaneous biliary drainage procedures, particularly since signals can be monitored in real-time. Further, because

initial needle placement can be done with ultrasound guidance, our approach would not only eliminate radiation altogether, but would also allow the procedure to be done at the bedside. While this study focused on percutaneous biliary drainage, the same approach can be used in antegrade nephrostomies or lumbar puncture. Future experiments will test the hypothesis that real-time optical monitoring is faster than the current method and results in less unintended complications.

Acknowledgment

1.2   Optical spectroscopy capable biopsy needle tip to seek high tumor content areas

Abstract

Biopsies are fundamental to the diagnosis, management and treatment of most cancers. Tissue samples enable a pathologist to make a diagnosis of cancer, to determine its type and nuclear grade, and to evaluate for cancer specific biomarkers that would affect the plan of action for proper treatment. Despite imaging guidance, up to 12% of image-guided needle biopsies are non-diagnostic. Non-diagnostic biopsies result from not sampling the lesion or sampling non-viable portions of the lesion. The results of simulations indicate that our proposed method can supplement current biopsy techniques with providing real-time non-destructive optical sampling at the tip of the biopsy needle to enable the operator to locate and sample from the most cellular and most suspicious areas of a lesion. Specifically, our proposed system can detect areas of high cellularity (i.e. higher DNA content in a specific volume), increased blood content, and decreased oxygen saturation, which are all associated with malignant cells. This approach takes advantage of the intrinsic optical contrast between benign and malignant tissue; thus there won't be any need for any exogenous contrast agent to be injected.

1.2.1   Introduction

Over 1.5 million breast biopsies are performed each year. According to American Cancer Society estimates, these biopsies will lead to the detection of 231,840 new cases of invasive breast cancers and 60,290 new cases of carcinoma in situ in women in the US in 2016 [12]. Although medical imaging is a tremendous screening device, tissue samples are usually necessary for identifying potentially concerning lesions or masses.

Examining tissue sample enables a pathologist to make a diagnosis of cancer and, if cancer, the type of cancer. After performing the biopsy, the samples are fixed and stained with Hematoxylin and Eosin (H and E) to evaluate the cellular morphology and tissue architecture under microscope. Immunohistochemical stains are applied to the samples to evaluate them for conventional breast cancer biomarkers such as Estrogen receptor (ER), Progesterone Receptor (PR), Her2/neu (a protein encoded by ERBB2, a known proto-oncogene; a cancer biomarker) [13] and Ki-67 (a marker for cellular proliferation) [14]. Pathologists use several important discriminating factors to distinguish a benign lesion from malignant. One of the most useful criteria is the presence of large number of cells with an increased size of their nucleus (N) compared to the cytoplasm (C) (increased N/C ratio). The differential pattern of scattering and absorption of the photons between normal tissue and tumor enables localization of the tumor. Figure 1.10 illustrates the microscopic H&E appearance of increased nuclei per volume in breast cancer relative to the normal breast tissue. An increased number of nuclei per volume will significantly increase the extent of backscattering of light, resulting in a distinct UV-visible reflectance pattern.

Reflectance spectroscopy has been extensively investigated to distinguish benign from malignant tumors in the breast [15]. The main limitation of reflectance optical spectroscopy is the poor penetration of light in vivo along with extensive light scattering, resulting in poor spatial resolution. For instance, the penetration of the UV light into the skin is limited to a few millimeters. Uncontrolled cell division of cancer cells results in an increased number of nuclei per volume of tissue. The absorbance profiles of the DNA (contained in nuclei) and protein (contained in cytoplasm) are very distinct at the wavelengths between 240 to 290 nm. Pure DNA strongly absorbs light at 257 nm while the peak absorbance of proteins is located at longer wavelengths such as 277 nm (Figure 1.11).

The distinct and strong light absorption of DNA has long been used to determine the purity of the DNA samples in vitro with commercially available kits, which routinely use the ratio of light absorption at 260 nm to 280 nm to quantify the amount of nucleic acid [16]. Since cancer cells have increased N/C ratios with increased DNA content per volume, the UV absorption at 250-265 nm (peak absorption of DNA) of a sample containing cancerous tissue should be higher when compared to equivalent volume of normal tissue. Figure 1.12 demonstrates that the light absorption of malignant tumor at 265 nm is much higher than benign or normal tissue mainly due to an increased DNA content; thus, confirming that UV spectroscopy is able to distinguish malignant from benign or normal breast tissue [1]. These data were obtained of normal breast tissue, fibroadenoma (benign lesion), and malignant breast lesion using reflectance spectroscopy. However, given the poor depth of penetration of UV light, this study was limited to in vitro samples.
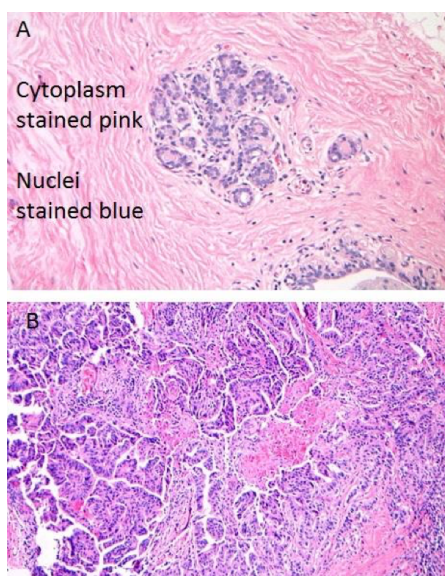
Figure 1.10: H&E stains of **(A)** Normal breast cell with nuclei stained blue and cytoplasm stained pink; **(B)** Invasive ductal carcinoma cells with increased N/C (nuclei/cytoplasm) ratio as indicated by increased blue staining relative to pink staining.

In addition to reflectance UV spectroscopy, the visible spectroscopy has also been

widely used for breast cancer detection. Cancer cells have a higher metabolic rate than normal cells, requiring more nutrients and oxygen. Tumor cells have angiogenic factors to enhance vessel formation in and around the viable tumor. Although this leads to an increase in blood content of a tumor, the tremendous consumption of oxygen by tumor cells still results in an overall decrease in oxygen saturation of the blood within tumor cells. Many groups have extensively investigated this characteristic and have published algorithms to detect higher blood content of tumors based on their light absorption at visible and near-infrared portion of the spectrum. Using diffuse reflectance spectroscopy, Brown et al. quantified oxygenation levels in blood vessels supplying breast cancer. They found prominent β-carotene absorption bands between 550 - 580 nm, an indicator of presence of oxygenated hemoglobin, in benign tissue, but these absorption bands were absent in the spectrum of malignant tissues.

Furthermore, diffuse reflectance spectroscopy has been shown to allow one to measure the total hemoglobin (blood) content of tissue as well as the oxygen saturation of the tissue [2]. Figure 1.13 demonstrates the results of the research developed by Zuzak et al. [2] in which the distincts absorption spectrum of oxy- versus deoxy-hemoglobin is depicted. By looking at this graph, one could appreciate that at wavelengths close to 570 nm, the absorption of oxy and deoxy-hemoglobin is similar while at longer wavelengths such as 600 nm, deoxy-hemoglobin shows a higher light absorption. Decrease in the hemoglobin oxygen saturation due to excess need of the tumor to oxygen will result in the higher absorption at 572 nm and thus will decrease the ratio of backscattered photons at this wavelength when compared to 600 nm.

In our proposed method, using the previously developed fiber-based sensor, a series of modulated light at 260 nm, 280 nm, 525 nm, 575 nm and 593 nm (the desired and commercially available wavelengths in LEDs) is sent into the breast tissue to perform UV-Vis reflectance spectroscopy at the tip of the needle by recording the backscattered light.

This provides localized optical sampling of the breast tissue to determine high tumor content areas for subsequent biopsies. In this work, a set of Monte Carlo simulations were performed to investigate the feasibility of using the ratio of backscattered light at the proposed wavelengths to distinguish the malignant from the benign breast tissue. In addition, the effect of cutting angle at the fiber tip on the detected signal at different wavelengths is investigated.
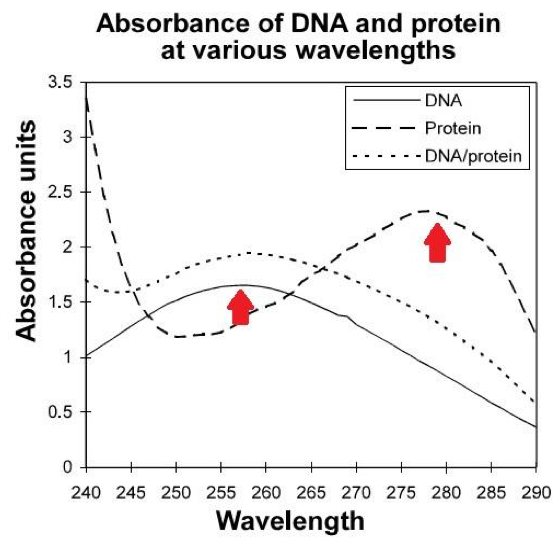
Figure 1.11: Peak absorbance of DNA is at 257 nm, while the peak absorbance of protein is around 280 nm [16].
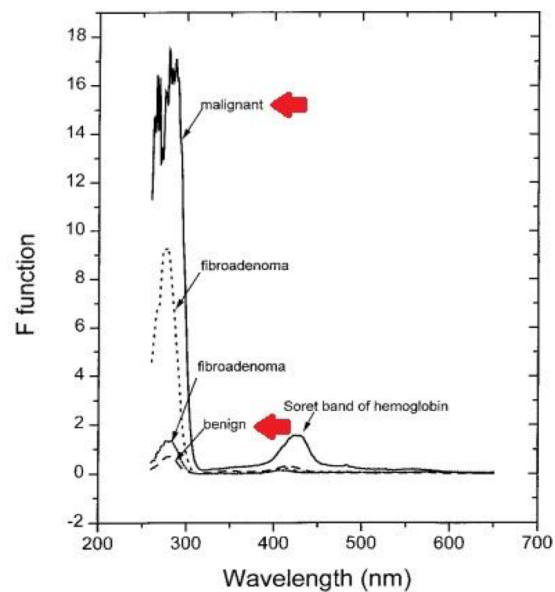
Figure 1.12: The absorbance in wavelengths around 280 and 260 nm is different for malignant and normal breast tissues. This is thought to be secondary to an increase in the DNA content of malignant tissue as compared to normal or benign breast lesion[1].
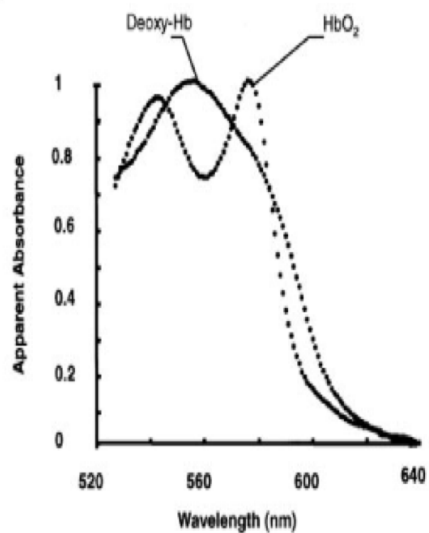
Figure 1.13: Absorbance spectra of Deoxy-hemoglobin versus oxy-hemoglobin. The differential absorption of these two forms of hemoglobin at 572 nm and 600 nm is used to determine the oxygen saturation of hemoglobin at the tip of our stylet needle [2].

1.2.2 Methods

The Monte Carlo simulations were used to calculate the backscattered light from the benign and malignant breast tissue at the desired wavelengths based on the scattering and absorption coefficients and anisotropy factors in the target tissue at these wavelengths. These parameters were calculated based on the experimental data in [2, 1, 16, 13].

The tissue model that was used in the simulations was a cylinder with a radius of 10 mm and thickness of 10 mm. Two fibers with 200 μm core diameter and 50 μm spacing between them were used to send the light inside tissue and detect the backscattered light. Figure 1.14 illustrates this model. The fiber tips had 35 degrees angle with respect to their surface normals. Based on the subsequent simulations, the depicted orientation of fibers in this figure resulted in the highest backscattered light at each wavelength.

To study the effect of the cutting angle at the fiber tip, on the amount of the backscattered light, the fluence of photons in the breast tissue at two 593 nm and 525 nm wavelengths was simulated. The percentage of the incident photons that entered the detecting fiber out of the total lunched photons was calculated for 15°- 60° cutting angle at the fiber tips.

1.2.3 Results

Figure 1.15 shows examples of the simulation results for calculating the fluence map of photons at benign and malignant tissues at the desired visible wavelengths. From these simulations, the percentage of the photons entering the detecting fiber out of the total number of photons inserted into the tissue is calculated. To differentiate the benign from the malignant breast tissue the ratios of the detected backscattered light, $R(\lambda)$, at 525 nm to 575 nm, at 593 nm to 575 nm and at 260 nm to 288 nm were calculated. Table 1.3 shows the ratios of the calculated backscattered light for the visible wavelengths and
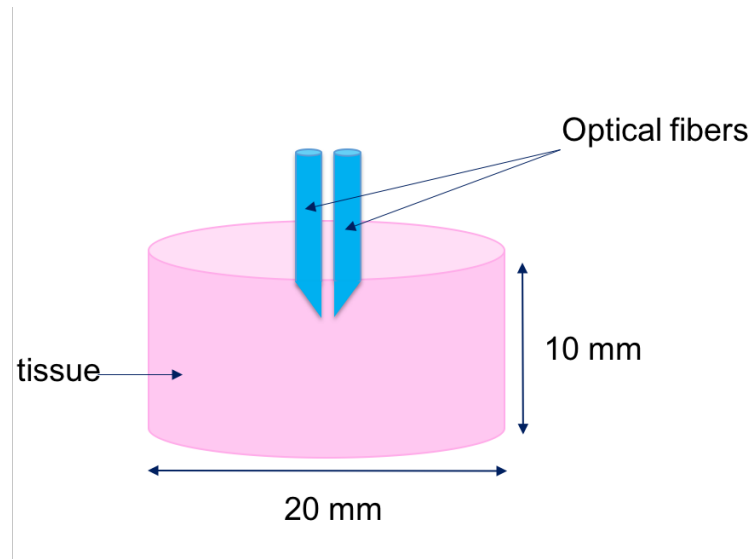
Figure 1.14: The tissue and fiber model used for Monte Carlo simulations.

Table 1.4 shows these ratios for the UV wavelengths.

The results of simulations for examining the effect of cutting angles at the fiber tips on the amount of backscattering light that entered the detecting fiber is shown in Figure 1.16.

Table 1.3: Simulated reflectance ratio at different visible wavelengths for benign and malignant breast tissues.

	Benign breast tissue	Malignant breast tissue
R(575nm) / R(593nm)	1.18	0.91
R(593nm) / R(525nm)	0.88	1.12
R(575nm) / R(525nm)	1.17	1.07

Wavelength	Benign breast tissue	Malignant breast tissue
525 nm		
575 nm		
593 nm		
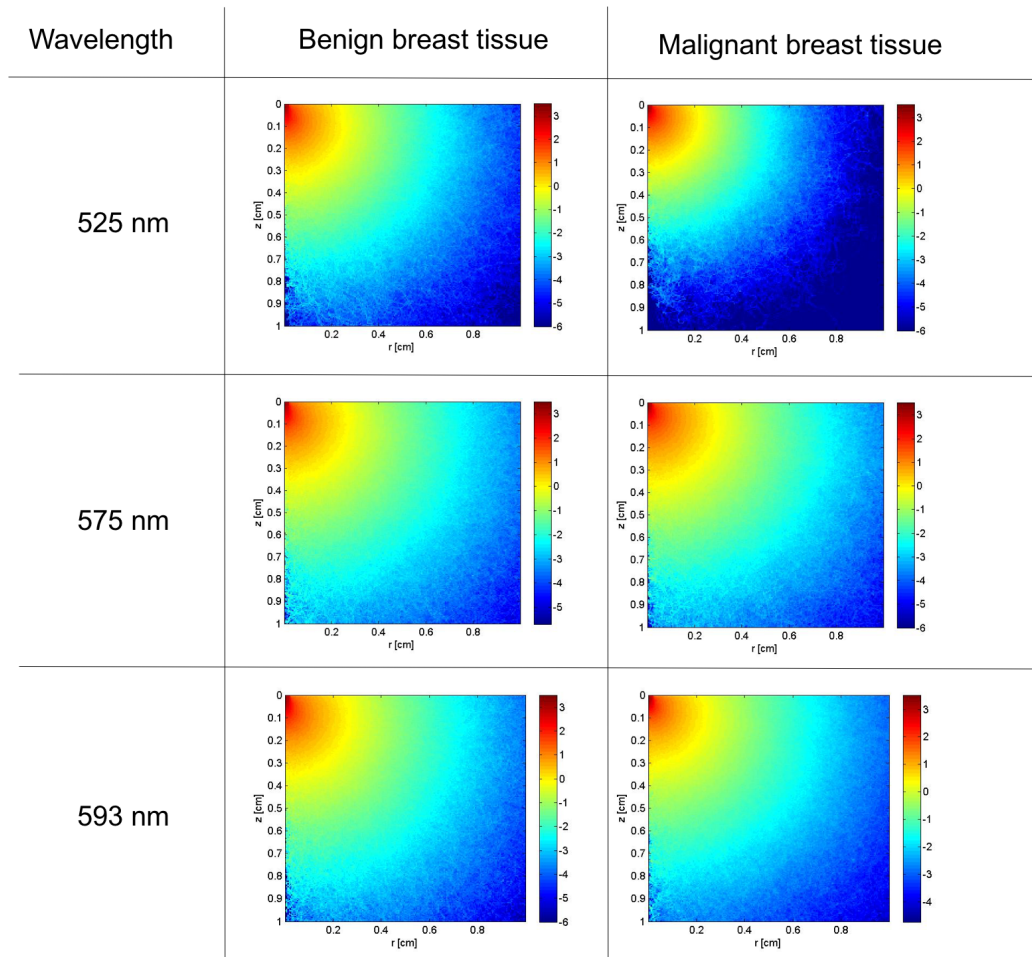
Figure 1.15: The simulated fluence map of photons in the benign and malignant breast tissues at 525 nm, 575 nm and 593 nm.

1.2.4 Conclusions

According to the results provided in Table 1.4, the amount of the backscattered light from the benign tissue at 260nm is greater than the malignant tissue which is in agreement with the results of studies indicating that the N/C ratio in the benign tissues is less than the malignant ones. As a result, the ratio of the backscattered light at 260 nm to 280 nm at the benign tissue is less than this ratio for the case of the malignant tissue. As can be seen in Table 1.3, in the normal breast tissue, the ratio of the backscattered light at

Percentage of the detected light at 593 nm

Cutting angle at the fiber tip

A

Percentage of the detected light at 525 nm

Cutting angle at the fiber tip
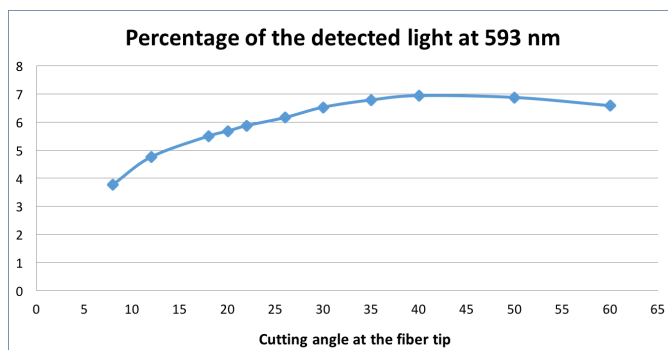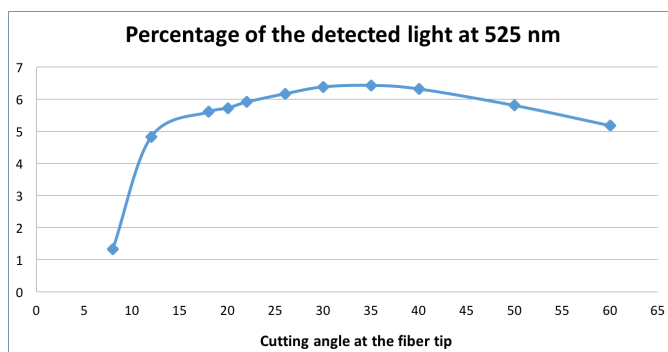
B

Figure 1.16: The effect of the cutting angle at the fiber tip on the percentage of the incident photons entering the detector fiber out of the total lunched photons at 593 nm (panel **A**) and 525 nm (panel **B**).

575 nm to 593 nm is greater than 1, and the ratio of the backscattered light at 593 nm to 525 nm is less than 1. In contrary, for the malignant tissue the ratio of the backscattered light at 575 nm to 593 nm is less than 1, and the ratio of the backscattered light at 593 nm to 525 nm is greater than 1. The results of the MC simulations suggest that the ratios of the backscattered light intensity at the proposed wavelengths can be used to differentiate the benign from malignant breast tissue.

As can be seen in the graphs in panel A and B of Figure 1.16 cutting the fiber tips

Table 1.4: Simulated reflectance ratio at different UV wavelengths for benign and malignant breast tissues.

	Benign breast tissue	Malignant breast tissue
R(260nm)	0.651	0.479
R(280nm)	0.789	0.869
R(280nm) / R(260nm)	1.213	1.813

at 35°- 40° would result in a higher percentage of the detected photons at the desired wavelengths.

Aknowledgement

1.3 Detection and activation of a light activatable prodrug using a dual fiber optic System

Abstract

One of the major challenges in controlling the administration of light-activatable chemotherapy prodrugs is the difficulty of monitoring the activation of the prodrug and the release of pure drug within tumor tissue in near real-time. Measuring the accumulation and activation rates of the prodrug are essential to understanding the pharmacokinetics of this unique delivery system. To address this challenge a new dual fiber optic system has been developed that can both deliver the activating wavelength of light for releasing the drug and monitor that release by detecting shifts in the fluorescence spectra of the prodrug. These fibers are embedded in a commonly used biopsy needle, which allows them to be inserted into the tumor in a minimally invasive manner. The drug activation and fluorescence excitation light is delivered through one fiber and the second collects fluorescent photons. We demonstrate this technique with a natively fluorescent photocleavable chemotherapy prodrug of doxorubicin that was activated in a tissue phantom. The use of the system for therapeutic drug monitoring was also demonstrated by showing that pure doxorubicin could be detected in a 1% intralipid tissue phantom at 0.1 $\mu g/ml$ which is seven times below the drug's IC-50 level indicating that it can detect doxorubicin within the clinically relevant range. The performance of this delivery and sensing system in tissue phantoms makes it promising for use in future *in-vivo* experiments to determine drug content as well as to activate and monitor light-activatable prodrugs.

1.3.1   Introduction

The cytotoxic drugs used in chemotherapy affect both healthy cells and tumor cells throughout the body. It is the toxic effect from the interaction of the drugs with the off-target healthy tissue that results in adverse dose-limiting side effects from chemotherapy agents [17, 18, 19]. Restricting the exposure of the active drug to just the tumor tissue itself could potentially help reduce these side effects. One way to achieve this localization of active drug is to chemically modify the drug to create a prodrug which is designed to have a low level of toxicity in healthy tissue but can be triggered to release the drug in tumor tissue for full therapeutic effect [20, 21, 22]. A promising approach to trigger the conversion of the prodrug into active drug is through light activation [23]. A prodrug that is activated only upon exposure to the delivered light would pass through healthy tissue including the liver with almost no effect, but would be triggered to release the drug within the illuminated tumor tissue [23, 24]. Light can be successfully delivered to the center of a tumor using a single optical fiber system and can trigger a photocleavable prodrug [23]. However, this single fiber system cannot monitor both the accumulation of the prodrug over time within the tumor tissue and the controlled release of drug with light exposure. This missing information is critical for understanding the pharmacokinetics of the prodrug delivery to the tumor and determining the optimum light exposure dosing for therapeutic efficacy.

To address this challenge we have developed a new needle-encased dual optical fiber system that is capable of delivering the activating wavelength of light to trigger conversion of the prodrug into active drug and also measure this conversion using a fluorescence quantification technique. Several commonly used chemotherapy agents are inherently fluorescent such as doxorubicin (DOX) [25, 26] and lend themselves well to fluorescence monitoring.

The first setting of the dual fiber system is for prodrug activation where one fiber

delivers the activating wavelength of light from an LED light source. This cleaves the prodrug releasing active compound. The second setting of the system is fluorescence detection where the LED used for photocleavage is switched to a the other LED that delivers the fluorescence excitation light. The second optical fiber then collects the fluorescence light from within the tissue and sends it to a spectrometer for quantification. In the *in-vivo* setting, the ends of the two fibers could be inserted into the center of the tumor tissue with minimally invasive techniques [23] to achieve both drug monitoring and activation.

This dual fiber system opens the way for longitudinal monitoring of prodrug accumulation and active drug release in the same tumor in the same mouse which is critical information to study the pharmacokinetics of the prodrug and its activation. In previous studies, *in-vivo* experiments demonstrating the activation of prodrug to pure drug in the mouse model were endpoint experiments where monitoring the prodrug accumulation and subsequent DOX release over time within the same individual was not possible. Mice were sacrificed after light delivery. The tumor was removed and sectioned followed by an extensive tissue extraction protocol to quantify the conversion of the prodrug to pure drug [27].

For these experiments we used a photocleavable prodrug of DOX known as DOX-PCB [24]. DOX is commonly used in a wide range of different cancer treatments and is known to have cardiotoxic effects which can result in cardiomyopathy and congestive heart failure [21, 26, 28]. This significant side effect restricts the cumulative patient dose. The DOX-PCB prodrug is formed by covalently attaching a photocleavable biotin group to the active amine on the DOX molecule. This molecule takes on a specific hairpin conformation in water that sequesters the active region of DOX and prevents it from intercalating into DNA. The DOX-PCB prodrug has been shown to have 200 times less toxic than the unmodified drug but can be restored to full therapeutic toxicity upon light

exposure at 365nm [23, 24].

Light activation is a unique way to trigger prodrug release. Previous chemotherapy prodrugs have been designed to activate in response to environmental differences between the tumor and healthy tissue such as low pH [29, 30] or elevated enzymatic activity [31, 32, 33]. The reduction in off-target prodrug activation relies on the magnitude of the difference between the tumor and healthy tissue with respect to the activating property. The challenge has been that there is a low contrast between the tumor and healthy tissue [34, 35], especially with regard to the high enzymatic activity of the liver.

This dual fiber system also opens up the possibility of using the system for therapeutic drug monitoring of non-prodrug compounds not just in blood circulation but in the actual tissue in which they are meant to be accumulating. Assessing the concentration of chemotherapy agent within a tumor in real time could provide essential information about how the drugs are behaving in an individual patient. This information can influence physician's decisions about changes to the treatment regime and can be made much sooner in the process than now, which is to wait several weeks or months to see if there are any bulk changes to the tumor mass itself.

We first demonstrate the ability of the system to detect the conversion of the DOX-PCB prodrug into active DOX in DMSO which is not optically scattering. Using the trends detected in DMSO we then demonstrate the same ability in a light-scattering tissue phantom. Finally, we show the ability of the system to detect DOX itself in a scattering medium as a demonstration of its application to therapeutic drug monitoring.

1.3.2 Methods and materials

Materials

Doxorubicin hydrochloride (DOX) was purchased from Sigma (St. Louis, MO, USA) and Qventas (Branford, CT , USA). The photocleavable biotinNHS (PCB) was purchased from Ambergen (Watertown, MA, USA). The fetal bovine serum (FBS) was purchased from Hyclone (Logan, UT, USA). The water was filtered with the Milli-Q Plus System (Millipore Corporation, Bedford, USA). Intralipid 20% was purchased from Sigma (St. Louis, MO, USA). Fiber optics cables (M92L01) with 200 μm core diameters and 0.22 numerical aperture were purchased from Thorlabs. The biopsy needle was purchased from BD (BD 405211 Quincke Spinal Needle, 600 μm inner diameter). Two LED light sources at 365 nm and 470 nm (Mic-LED-365 and Mic-LED-470), a beam combiner and a fiber coupling adaptor were purchased from Prizmatix. An Ocean Optics USB4000-UV-VIS was used as the spectrometer. The 12.5 mm diameter, dichroic longpass filter at 550 nm was purchased from Edmund Optics.

DOX-PCB Prodrug

The DOX-PCB prodrug has been described and fully characterized by Ibsen et al [24].Briefly, the prodrug was created by covalently bonding a photocleavable nitrophenol group to the amine on the sugar group of the DOX molecule. Attached to the other side of the nitrophenol group is a short PEG chain attached to a biotin molecule at the end. The prodrug molecule takes a hairpin conformation in water blocking the conjugated ring structure of DOX from intercalating into the DNA double helix which is a main therapeutic property. The nitrophenol group absorbs light at 365 nm and causes the release of pure DOX from the molecule. This released DOX has been shown to have full biological and therapeutic activity against cancer cells. The prodrug molecule itself is

resistant to enzymatic cleavage making light activation the main mode of DOX release.

Dual Fiber Optic Activation and Detection System

In order to locally excite the fluorescent DOX or activate the DOX-PCB and to measure the fluorescence signal we have used our previously developed fiber optic based biopsy needle [36]. In this setup, two fiber optic cables with 200 μm core were integrated into a biopsy needle with 600 μm inner core diameter. Before inserting the fibers into the needle, we removed the jacket and the buffer of the fibers up to the length of the needle. We removed the coating of one of the fibers inside the needle and inserted the other fiber with the coating on. This was done to avoid light coupling between the fibers and to properly fit them inside the needle. After inserting the fibers into the needle, under a microscope, we applied a black epoxy in between the fiber tips and around them to ensure no light couples between the two fibers. One of the fibers inside the needle was used to send the light to the sample solution and the other one was used to transmit the fluorescence light to the detector. The 470 nm LED was used to excite DOX and the 365 nm LED was used to photoactivate the DOX-PCB molecules. The beam combiner and fiber coupling adaptor were used to combine the beams from two LEDs and couple them to the multimode fiber. For the detection, we used an Ocean Optics USB4000-UV-VIS spectrometer to monitor the fluorescence spectrum of the excited DOX as well as the activated DOX-PCB. The Edmund Optics longpass filter was placed directly in front of the spectrometer to reject the excitation light. Because of the low signal level, we wanted to minimize the number of optical elements between the spectrometer and the filter. The intensity of the fluorescence signal was much lower than the excitation light, hence, using the dichroic filter was necessary. Figure 1 shows a schematic of the needle with the embedded fibers, the excitation and fluorescence light path in the solution along and the illumination and detection setups. In the experimental setup, the needle was

mounted on a micro positioning stage to be vertically inserted into the tube of the sample solution as can be seen in Figure 1. The excitation light traveled through one of the fibers and entered the media sample that contained either DOX or DOX-PCB. This fiber carried either the activation wavelength of 365 nm or the fluorescence excitation wavelength of 470 nm. The excitation light generate fluorescence photons some of which were coupled into the second fiber optic that channeled them to the spectrometer for detection. A dichroic mirror filtered out stray excitation photons that also coupled into the second fiber. Images of the LEDs, the beam combiner, the fiber coupling adaptor, the spectrometer, and the dichroic mirror at its input and shown at the bottom of Figure 1.17.
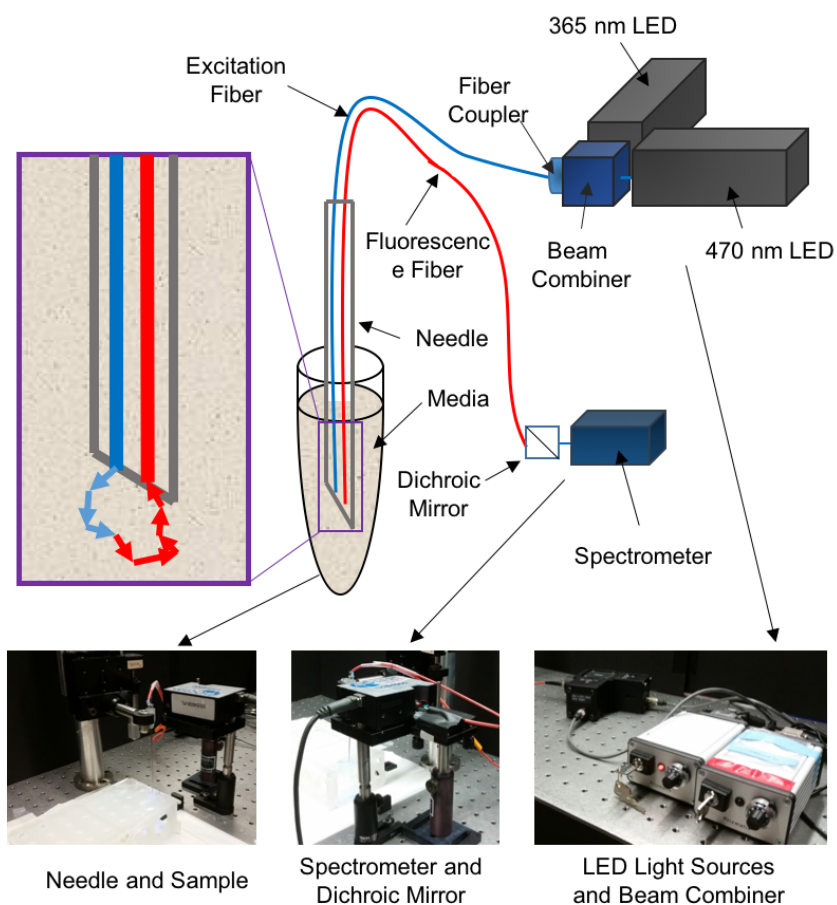
Figure 1.17: A schematic of the fibers embedded in the biopsy needle and the excitation and fluorescence light path. The media solution contained DOX or DOX-PCB and also contained 1% intralipid to make it a scattering tissue phantom. The images show the actual setup components including the biopsy needle vertically mounted onto the stage with optical fibers inside it, the two 365 nm and 470 nm LEDs with their current drivers, the beam combiner and fiber coupler, and the spectrometer with the dichroic mirror to reject the excitation light.

Detection Limit of DOX in the Liquid Tissue Phantom

An aqueous tissue phantom was created using 1% Intralipid in water (diluted from a solution of Intralipid 20%) to mimic the scattering effect of tissue. To test the detection limit of DOX in water and in the scattering media three different concentrations of DOX were used (0.1 $\mu g/\mu l$, 1 $\mu g/\mu l$ and 20 $\mu g/\mu l$). These three concentrations were

created with the 1% intralipid. Solutions at these concentrations were created without the intralipid for comparison. In total, six DOX solutions were studied. A sample of 50 μl of the solution was placed into a micro-centrifuge tube for analysis. The end of the fiber optic needle was inserted into the center of the liquid and the readings taken. The emission peak of the excited DOX is approximately at 594 nm. To account for slight variability in the actual peak location from reading to reading the intensity of the signal between 590 nm to 598 nm was averaged and used as the fluorescence intensity at each recording. In all of the experiments, the integration time on the spectrometer was set to 10 seconds. The entire spectrum was collected three times and averaged for each recording to reduce the high frequency fluctuations on the signal. To examine the repeatability of the measurements, three sets of spectral recordings were performed on each solution.

Activation of DOX-PCB and Detection of the Released DOX

In the subsequent experiments, the use of the dual fiber optic system to photo-trigger and measure the conversion of DOX-PCB to DOX was studied. The DOX-PCB prodrug has low solubility in water and so these activation experiments were first carried out in pure DMSO. It had been shown previously that the activation of DOX-PCB in DMSO results in the same formation of pure DOX as it does in cell culture media [24] and tissue [23]. The experimental solutions contained 0.061 mM of DOX-PCB and the control solutions contained 0.061 mM of DOX. A sample of 50 μl of the test solution were placed inside a micro-eppendorf tube and the end of the fiber optic needle was placed into the center of the solution for activation and monitoring. The solutions were exposed to the activation light for 30 min at which point the activation LED was switched out for the fluorescence excitation LED. The fluorescence signal of the solution was acquired following the previously mentioned protocol. The LED's were switched again and the solution was exposed for another 30 min time period. The activation and monitoring of

the DOX-PCB solution with no scattering material continued for a total of 6 hours.

A liquid tissue phantom was created using water/fetal bovine serum (FBS)/DMSO (89:9:2 vol%) with 1% Intralipid to keep the DOX-PCB soluble throughout the experiment. As before the experimental solutions contained 0.061 mM of DOX-PCB and the control solutions contained 0.061 mM of DOX. The activation and monitoring protocol as described above was used and conducted in this tissue phantom for a total of 7 hours.

1.3.3   Results

Light Activation of DOX-PCB in DMSO

The fluorescence emission spectra collected by the dual fiber system at different exposure times for DOX-PCB and DOX in DMSO is shown in Figure 1.18. When DOX-PCB was exposed to the activating 365 nm light for increasing durations (Figure 1.18A), a spectral shape change was observed in the 565 nm region. This shape change and the appearance of a new 565 nm peak is especially evident when the spectra are normalized to the major emission peak characteristic of DOX at 594 nm (Figure 1.18B). No change in the spectral shape is seen when DOX is exposed to the same intervals of 365 nm light. The DOX-PCB spectral change coincides with the creation of 18.5 ng of DOX after 7 hours of light exposure as determined by mass spectrometry.

Light Activation of DOX-PCB in Liquid Tissue Phantom

DOX-PCB and DOX fluorescence emission spectra collected in the aqueous optical tissue phantom are shown in Figure 1.19. A DOX-PCB spectral change with 365 nm activating light exposure was also seen under these optically-scattering conditions. Increasing durations of the activating light exposure resulted in the appearance of a shoulder peak in the DOX-PCB spectra (Figure 1.19A, B) which grew in size with longer
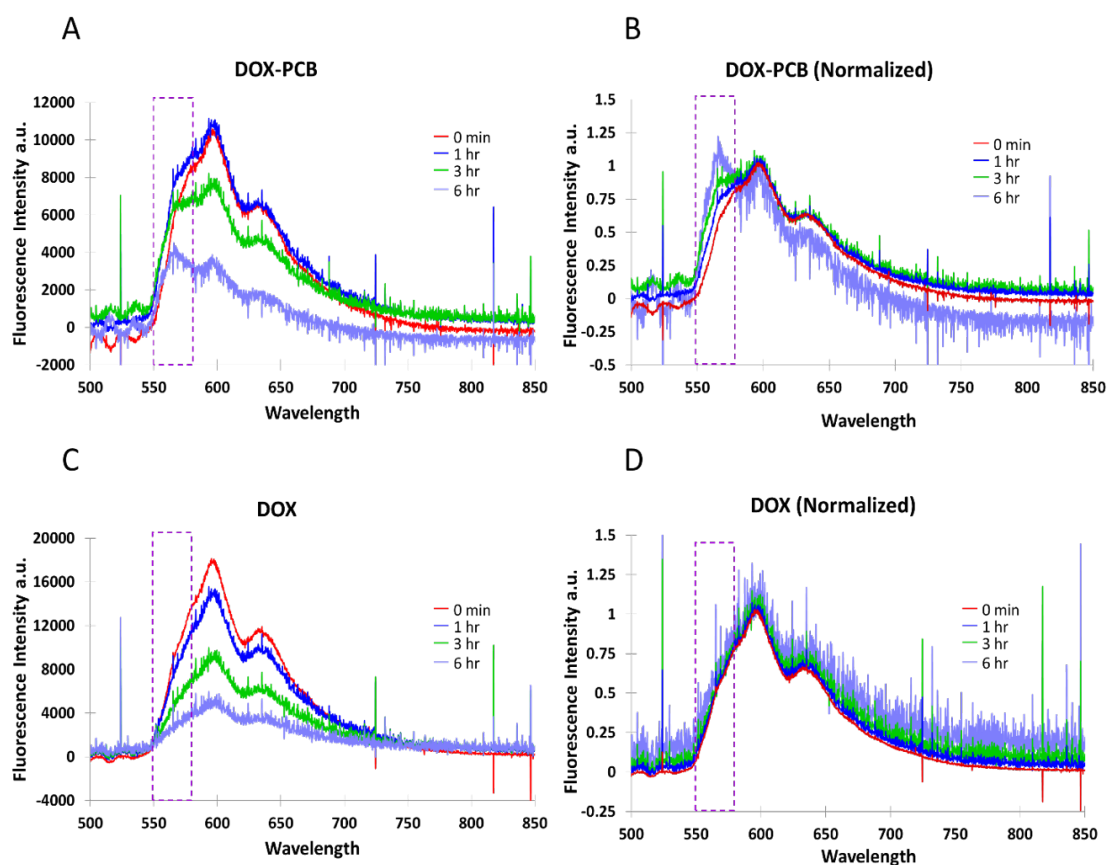
Figure 1.18: Fluorescence emission spectra (excitation at 470 nm) of DOX-PCB and DOX in DMSO (0.061 mM) with increasing exposure to 365 nm light. In panels B and D all spectral values have been normalized to the fluorescence intensity value at 594 nm to allow for direct comparison of spectral shape. **(A, B)** Upon increasing exposure of DOX-PCB to 365 nm light, a unique peak appears at approximately 565 nm as shown in the dashed box. **(C, D)** The appearance of the 565 nm peak is not seen when unmodified doxorubicin is exposed to the same intervals of 365 nm light.

exposures. No change in spectral shape was seen for DOX with equivalent 365 nm light exposures (Figure 1.19C, D). The emergence of the shoulder peak in the DOX-PCB spectra most likely coincides with the creation of DOX after 7 hours of light exposure. The presence of DOX was confirmed by mass spectrometry however quantification was not possible due to interference from the other components in the tissue phantom mixture.
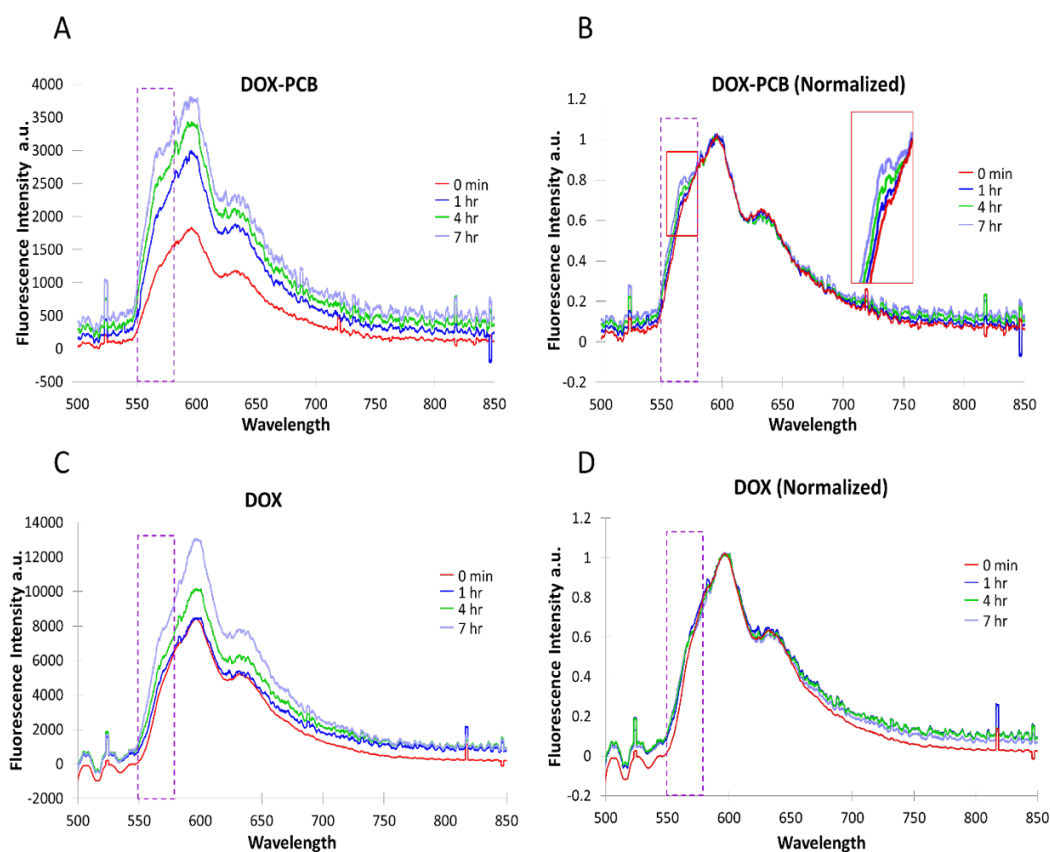
Figure 1.19: Fluorescence emission spectra (excitation at 470 nm) of DOX-PCB and DOX (0.15 mM) in an aqueous optical tissue phantom with increasing exposure to 365 nm light. The aqueous tissue phantom consisted of water/FBS/DMSO (89:9:2 vol%) containing 1% intralipid. In panels B and D all spectral values have been normalized to the fluorescence intensity value at 594 nm to allow for direct comparison between the different spectral shapes. **(A, B)** With increasing DOX-PCB exposure to 365 nm light, an elevated shoulder peak appears at approximately 565 nm as shown within the dashed box. The inset in panel B shows a magnified view of the increasing shoulder peak **(C, D)** The 565 nm shoulder peak is not observed when unmodified doxorubicin is exposed to the same light intervals.
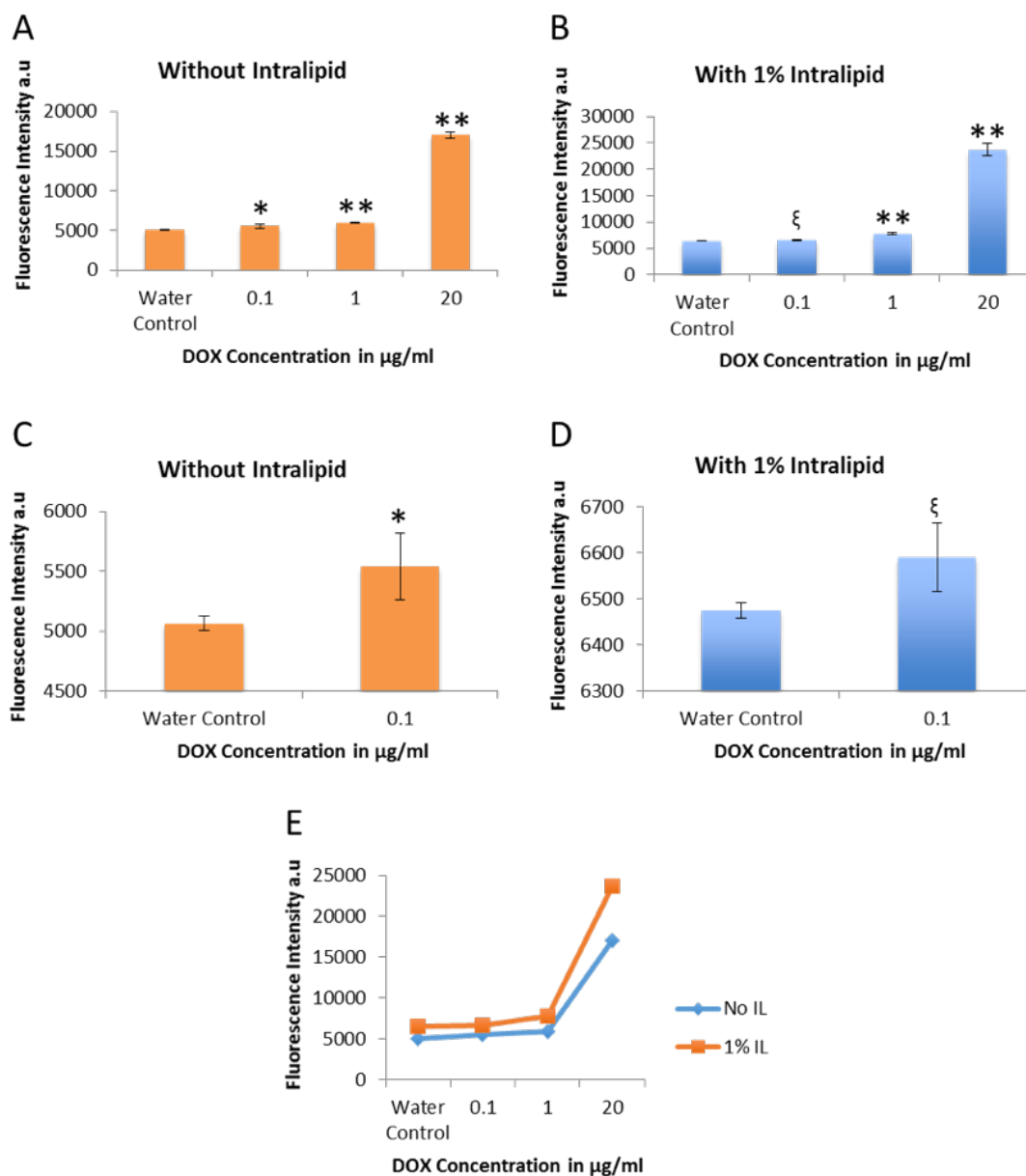
Figure 1.20: Peak fluorescence intensities at 594 nm from three DOX concentrations with and without scattering material compared to the water reference. **(A)** Peak fluorescence intensities without intralipid compared to water and **(B)** Peak fluorescence intensities with 1% intralipid added to the DOX solutions and the water reference. **(C and D)** Zoomed in graphs from panels A and B to show specifically the comparison between peak fluorescence intensities of the water reference and the 0.1 $\mu g/ml$ DOX solution with and without the presence of 1% intralipid. **(E)** Peak fluorescence intensities of the 6 DOX solutions and the two water references compared to each other. The fluorescence signal level is higher in samples that contain the scattering material. $*$P$\leq$0.05 and $**$P$\leq$0.01 using a two-sample t-test (two-sided) performed at the 5% significance level compared to the water control sample (n=3). ξ denotes p=0.0586 compared to the water control which is trending towards significance.

Detection Limit of DOX in Water and the Liquid Tissue Phantom

The measured intensity of peak fluorescence at 594nm for the three concentrations of DOX solutions with and without 1% Intralipid are shown in Figure 1.20A and 1.20B. The solutions contained 0.1 $\mu g/\mu l$, 1 $\mu g/\mu l$, 20 $\mu g/\mu l$ of DOX. A pure water sample was used as the reference. A zoomed in comparison between water and the lowest concentration of DOX with and without the scattering material is illustrated in Figure 1.20C and 1.20D and demonstrates the ability of the dual fiber system to detect and differentiate the low concentration of DOX at 0.1 $\mu g/\mu l$ from the background water. This is seven times below the IC-50 level of DOX (0.7 $\mu g/\mu l$) even in presence of highly scattering media. The water control was found to be significantly different from each of the DOX samples in the non-intralipid experiment. The water control was also found to be significantly different from the 1 and 20 $\mu g/\mu l$ samples in the intralipid experiment. The 0.1 $\mu g/\mu l$ sample was found to have a p-value slightly higher than 0.05 and so was trending towards significance. It indicates that the two values can be resolved allowing for a successful detection of DOX in the scattering media down to 0.1 $\mu g/\mu l$.

1.3.4   Discussion

The dual fiber system has been demonstrated to both activate the photocleavable prodrug as well as monitor that activation through detection of shifts in the prodrug's fluorescence spectra.

These shifts in florescence spectra were independent of photobleaching. One observation in the DMSO tissue phantom was the reduction of the DOX fluorescence intensity with increasing exposure to the 365nm activation light as shown in Figure 1.18C and D. However, when you normalize each of these spectra to directly compare their spectral shapes we see no change. This indicates that over the course of hours the DOX

photobleached from the exposure but that no chemical modifications occurred to the DOX that would shift spectral output. In Figure 1.18D the final DOX spectra at the 6 hr time point has a greater amount of noise that has been magnified by the normalization process due to the low intensity of the overall spectra, but it does not show any fundamental change in the underlying shape of the spectra.

This is in contrast to the behavior of the DOX-PCB upon increasing levels of light exposure. We see the shoulder peak at 565 nm increase in intensity relative to the major peak at 594 nm with increasing light exposure. This change is evident when we normalize the spectra to the 594 nm peak. This change in the peak height ratios indicates that there is a chemical change that is occurring with the DOX-PCB prodrug along with photobleaching. The presence of pure DOX was confirmed using HPLC in these exposed samples meaning that the spectral shape change is likely due to the release of DOX.

In the case of the solvent solution water/FBS/DMSO (89:9:2 vol%) containing 1% intralipid the interaction between the 365 nm light and the DOX and DOX-PCB molecules produced the opposite effect with an observed increase in fluorescence intensity with increasing light exposure. It is likely that this increase resulted from differences in the way the DOX and DOX-PCB interacted with the solvent solution which can have a very significant effect on the fluorescence spectra of a compound. FBS is a complicated solution containing many different proteins that can form complexes with DOX and DOX-PCB including albumin. This helped to keep the drugs in solution, especially DOX-PCB which has low solubility in pure water. There is also the possibility that the DOX and DOX-PCB can form complexes with the intralipid molecules as well. These interactions appear to have a protective effect preventing the same photobleaching observed in pure DMSO. The enhancement of the fluorescence signal could be caused by these interactions or possibly by changes over time in the scattering properties of the intralipid.

An important trend seen with these tissue phantom samples is the increase in prominence of the shoulder peak at 565 nm with increasing light exposure for the DOX-PCB samples where the DOX samples do not show any difference. This is the same trend observed for the more simple DMSO solvent solution although the size and shape of the shoulder peak is different between the DMSO and the intralipid tissue phantom solutions. This is probably caused by interactions with the proteins and intralipid in the tissue phantom sample. The changes that are seem in the 565 peak with increasing 365 nm light exposure are likely not due the DOX portion of the molecule since the spectral shape of the DOX control was shown to not have any change with light exposure. The spectral changings are likely from the nitrophenol/PEG leaving group that is also released along with the pure DOX as a byproduct of the DOX-PCB molecule cleavage. The increase in the concentration of the freed nitrophenol/PEG leaving group likely increased the fluorescence at 565 nm giving us an indicator for prodrug activation.

This dual fiber system has also been shown to detect the chemotherapy agent DOX down to a concentration of 0.1 $\mu g/ml$ within a tissue phantom that mimics the light scattering properties of tissue. That is 7 times lower than the IC50 for cell culture experiments which puts the lower limit of detection well into what could be clinically relevant concentrations within a tissue. This makes it a promising platform technology to detect the accumulation of DOX by itself *in-vivo* with minimal invasiveness. Inserting the dual fiber optic needle into the center of the tumor allows for multiple readings from the same tumor to be made over time without causing significant damage to the tissue. Currently the state of the art method to determine DOX accumulation in tumor tissue over time is to excise tumors from different individuals at different time points after drug administration. The tumors must be sectioned and the drug extracted to measure on HPLC/Mass Spec. This does not give an accurate picture of what happens at the individual level over time but rather gives a general trend in a population. This device

would make it possible for the first time to get an estimate of DOX concentration in the same tumor as it is accumulating giving us a better understanding of what happens in an individual tumor over time. The application of this device to monitor prodrug activation over time *in-vivo* would be a major step forward especially in this new field of light activatable prodrugs. Future work will look into correlating the intensity increase in the 565nm peak with the concentration of the released DOX to allow for localized dosing information.

In-vivo tissue is highly scattering which limits the tissue volume in which the dual fiber system will be able to collect photons. However, obtaining drug content from deep within a tumor even over a small volume, can give important insights into how drug is being delivered to the tumor especially in the hard to reach interior. This type of data could be invaluable in the clinical setting to give physicians additional information needed to make dosing regimens personalized to individual patients. This information will also be important during the drug development process as well when designing and optimizing a drug or prodrug formulation and delivery system. This provides a potentially powerful alternative to costly and time consuming end-point experiments where large numbers of individual tumors are used to piece together the time course of drug accumulation without providing time course information on an individual tumor level.

1.3.5   Conclusions

The dual fiber optic based system developed here has the ability to detect the presence of the naturally fluorescent chemotherapy agent doxorubicin in pure water and in a liquid tissue phantom down to levels of 0.1 $\mu g/ml$. This is 7 times below the IC50 for DOX in cell culture conditions which indicates that it should be able to detect therapeutically relevant concentrations of DOX in a real tissue. This was accomplished

by using the first fiber to deliver the excitation wavelength of light to the tissue phantom sample while the second fiber collected the fluorescent photons and delivered them to a detector. A dichroic mirror was used to filter out the excitation photons from the fluorescent photons in the collection fiber. The needle based casing of the dual fibers allows it to be easily inserted into tissue allowing it to be used for future *in-vivo* studies.

The ability of the dual fiber system to deliver the activating wavelength of light to the light-activatable prodrug DOX-PCB has also been demonstrated in a scattering tissue phantom. This delivered light, successfully released DOX from the DOX-PCB prodrug as confirmed by HLPC analysis. The system was then used to detect the shifts in fluorescence spectrum, in particular an increase in the 565 nm shoulder peak relative to the intensity of the main 594 nm peak, which indicates successful activation of the prodrug. This spectral change likely comes from a release of the nitrophenol/PEG chain leaving group that is produce as the DOX-PCB molecule in cleaved.

Future work will study the use of this system to obtain actual drug concentration information from tumor tissue in-vivo which can be very useful for clinical dosing applications as well as research and development of new chemotherapy agents and prodrugs.

Acknowledgment

Chapter 1, in part, is currently being prepared for submission for publication of the material. Baghdadchi, Saharnaz; Esener, Sadik; Mattrey, Robert; Eghtedari, Mohammad.

"Fiber sensor assisted in-vivo needle guidance for minimally invasive procedures" and Schutt, Carolyn; Baghdadchi, Saharnaz; Ibsen Stuart; Esener, Sadik. "Detection and activation of a light activatable prodrug using a dual fiber optic System". The dissertation author was the primary investigator and author of this material.

Chapter 2

Innovative systems for spatial imaging in clinical settings

2.1　A novel system for endoscopic imaging of upper airway tumor

Abstract

One of the major issues with successful screening of throat cancer is the availability of the specialists to perform tests with high sensitivity and specificity for early disease detection. Although endoscopic techniques have been developed for detection of upper airway tumors, their sensitivity and specificity are highly dependent on the operator's experience. To address this challenge, a simple to use imaging system is developed that is capable of focusing on different parts of the throat and generating clear pictures. We have used a tunable lens with a miniature camera for this purpose and designed and 3D printed adaptor to couple the lens and camera together. The performance of this system on manikin's throat makes it promising for use in future clinical imaging of upper airway

tumor.

2.1.1   Introduction

Having a close-up view of inside the throat is one of the initial steps that specialists take in diagnosing problems with larynx and potential upper airway tumor. In indirect laryngoscopy (Figure 2.1A), a mirror is inserted into the throat to explore the area. This method provides a good depth perception, however, in patients with strong gag reflex it is difficult to observe the anterior commissure [37]. To provide a close view of the larynx, direct laryngoscopy is required which is performed with a handheld curved or straight blade (Figure 2.1B). Extreme care must be taken so the blade is not inserted too far as it will not let the vocal cords be fully exposed. The direct laryngoscopy is usually performed under complete sedation by a specialist with the aid of skilled assistants to manipulate the external laryngeal. In both of the methods, the optimal position is often unpredictable due to the individual variations in anatomy, however, the proper head and neck positioning is critical. An improper head positioning during the intubation can potentially cause cervical spinal cord injury [38]. In addition, injuries to the airway and hemodynamic-related complications have been reported in direct laryngoscopy [39]. In this work we present a proof of concept novel system for endoscopic imaging of upper airway tumor. Our setup uses a tunable lens with an endoscopic camera and an open source software to generate all-in-focus images of throat. The setup can be used by non-professional personal to generate clear pictures of the throat tumors.
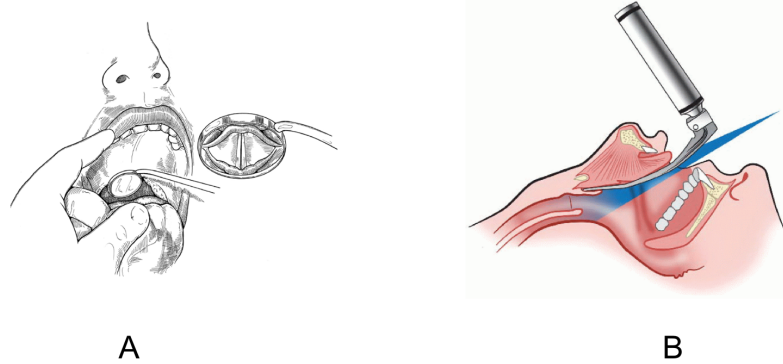
Figure 2.1: Laryngoscopy. The indirect method with a mirror **(A)**, the direct method with a mackintosh blade **(B)**.[40, 41]

2.1.2   Methods and materials

A fast electrically tunable lens (Part No. EL-6-18-VIS-LD) was purchased from Optotune. The lens has a 18mm×18mm×5mm cubic shape, with the ability to change the focal distance between 50mm to 120mm by applying current to it. It is accompanied by a USB powered lens driver (Electrical lens driver 4), purchased from Optotune. Its Labview driver was obtained from the Optotune company to program the current increments applied to the tunable lens. A small USB powered endoscopic camera (CrazyFire 2.0MP HD 720P Coms 6 LEDs) was purchased from Amazon. The camera had a 6mm clear view and 30fps image capturing rate. In order to connect the camera to the tunable lens an adapter is designed in SolidWorks and 3D printed. Figure 2.2 shows the assembly of these parts and the setup being tested on a manikin.
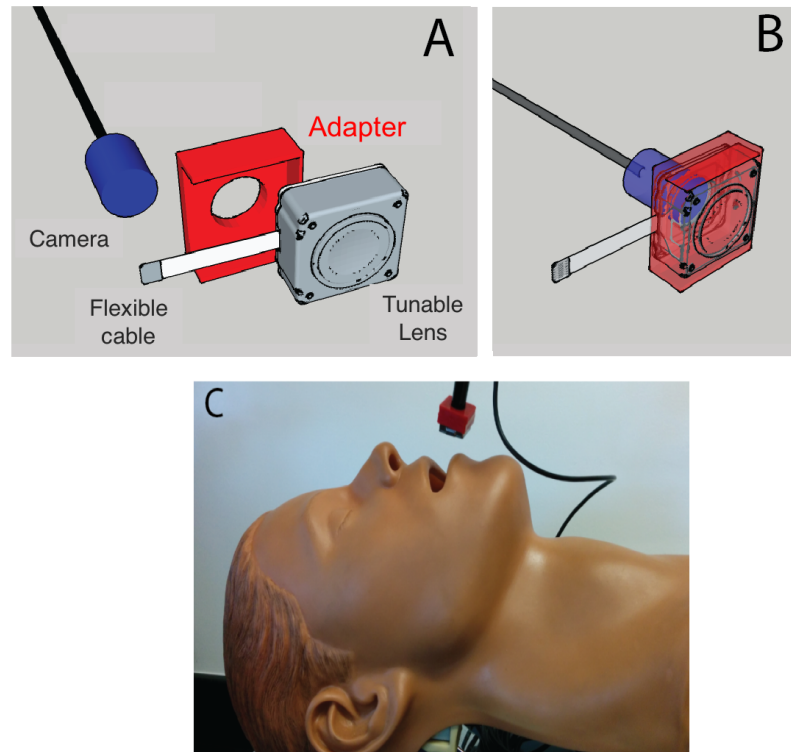
Figure 2.2: The schematic of tunable lens, 3D printed adapter and camera **(A)**. The assembly of three parts **(B)**. The setup being tested on a manikin **(C)**.

The Zemax model of the tunable lens was used to simulate the focusing ability of the lens to generate pictures of the objects located between 3 cm to 30 cm away from the lens. Since the Zemax model of The lens inside the endoscopic camera was not available, a standard Bk7 glass lens with 8 mm focal length was used in the simulations. The schematic of lens configuration used in these simulations are illustrated in Figure 2.3.
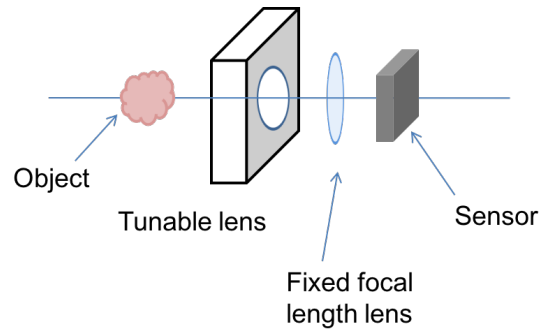
Figure 2.3: The schematic of tunable lens, 3D printed adapter and camera **(A)**. The assembly of three parts **(B)**.

The Labview code for the lens driver was changed to synchronize the lens with the camera. After each increment in the current applied to the lens, an image was taken by the camera. 30 images were taken in each set and were saved afterwards. Due to the 30 fps speed of camera, each set of images took around 1 second to finish. The speed of focus change for the tunable lens was a few milliseconds, which did not t play a role in the speed of the whole process. To generate an all-in-focus image from the set of pictures taken in each sequence, an open source focus stacking software [42] was used.

Two sets of images were taken. For the first set, a piece of paper with some text on it was used at the target. The paper was placed 50 mm away from the setup and was tilted such that the top and bottom part of it are at different horizontal distances with the setup. For the second set, the throat of a manikin was used as the target. The setup was inserted into the manikin's mouth and 30 pictures in a sequence were taken. An external handheld light flashlight was used to illuminate inside the throat. The flash light can be replaced with the forehead light that the examiner can use during the experiment.

2.1.3 Results

The results of Zemax simulations in evaluating the focusing ability of the tunable lens to generate clear pictures of the objects located at 3-30 cm away from the lens is

shown in Figure 2.4 A-D. As can be seen in this Figure, by changing the curvature of the tunable lens, it can focus the light coming from sources located at 3-30 cm away from it and hence generate in focus pictures of the objects located at these distances.

Figure 2.5 shows the images taken from the tilted paper as the target. Figure 2.5 A and B show two sample images within the sequence of 30 images. In Figure 2.5 A, the bottom part of the of the paper is in focus and in Figure 2.5 B, the top part is in focus. Figure 2.5 C shows the all-in-focus version image of the paper that is generated by stacking the 30 images in the sequence.

A. Object at 3cm

B. Object at 5cm

C. Object at 9cm

D. Object at 30cm
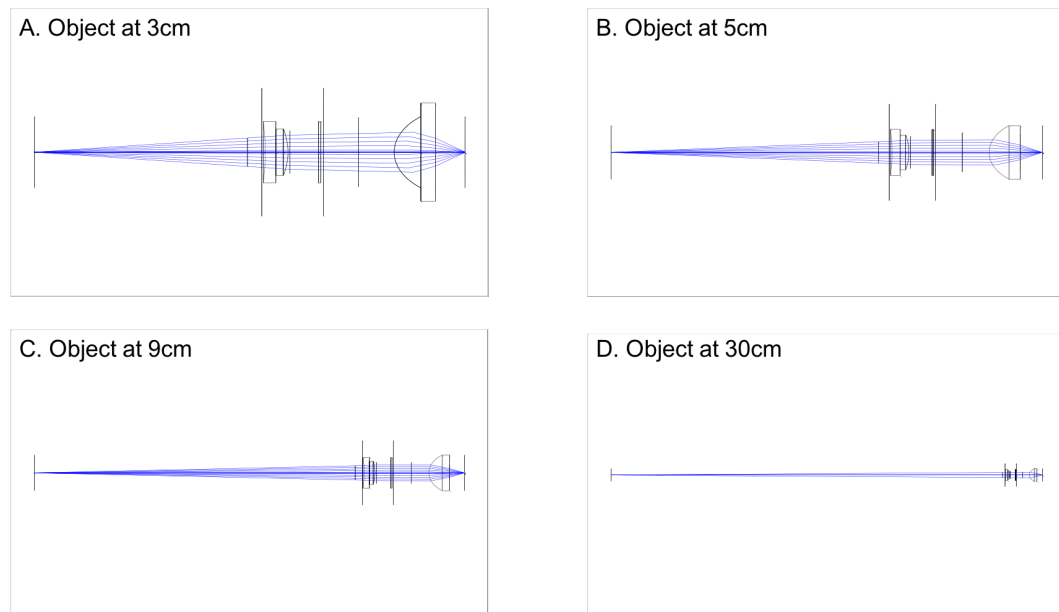
Figure 2.4: The Zemax simulations of focusing ability of the tunable lens and a fixed focal length lens for objects located 3 cm, 5 cm, 9 cm and 30 cm away from the lens.

Figure 2.6 shows three frames of the images taken from a throat in a manikin. Panel A and B are frames at witch the bottom and the top parts are in focus, respectively and panel C shows the stacked all-in-focus image.
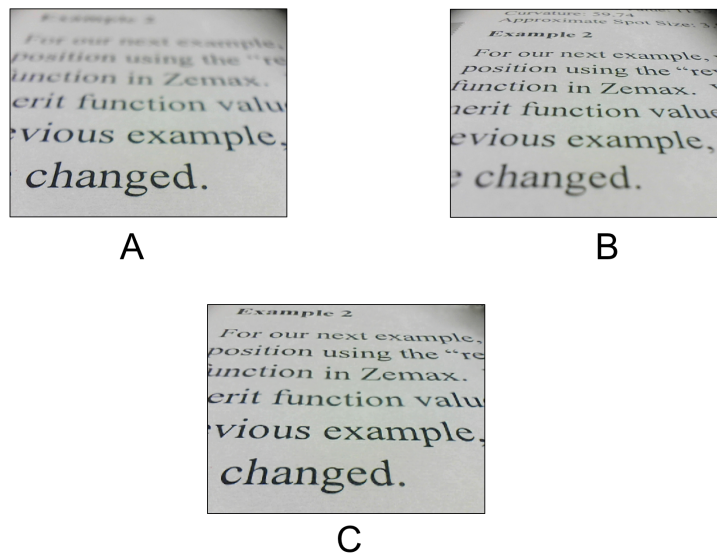
Figure 2.5: The images of a tilted paper with text on it taken with the developed setup. The bottom part of the paper is in focus (**A**). The top part of the paper is in focus (**B**). The all-in-focus image of the paper (**C**).
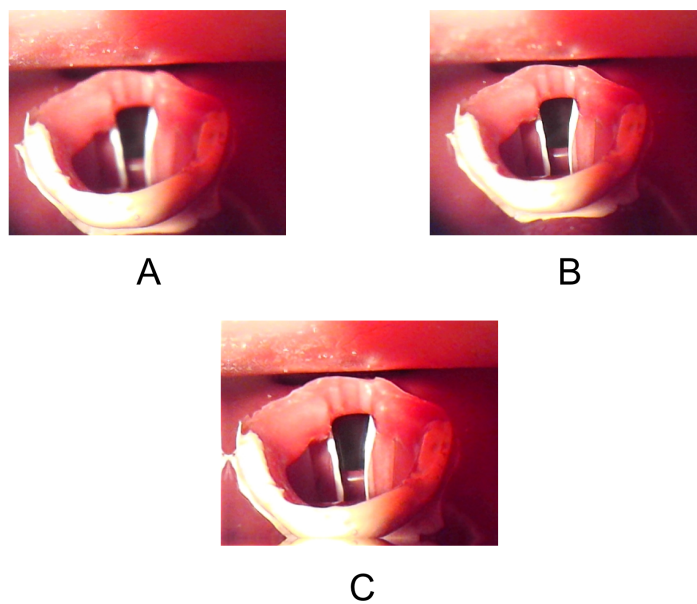
Figure 2.6: The images of a tilted paper with text on it taken with the developed setup. The bottom part of the paper is in focus (**A**).The top part of the paper is in focus (**B**). The all-in-focus image of the paper (**C**).

2.1.4   Discussion

Among applications of modern endoscopy, detection, characterization and removal of neoplastic lesions have been most frequently reported [43, 44, 45] . Despite substantial technical improvement during these years, inadequate visualization, misinterpretation, and lesion subtlety all lead to the continued suboptimal detection and evaluation of early malignancies. In addition, all current endoscopic techniques are heavily dependent on the skill and experience of the operators. Our novel endoscopic system, on the other hand, can be operated by a minimally trained operator and can generate in-focus images of the legions located at different distances from the front lens. Importantly, this imaging platform can potentially incorporate most of the new endoscopic techniques in addition to generating 3D images of upper airway tumor. In this design, we used a tunable lens along with a miniature camera and 3D printed an adapter to connect them. A custom Labview code was developed to increase the current applied to the tunable lens in equal steps, while taking a picture after each step. 30 images were taken in each set, which took around 1 second. The speed of focus change for the tunable lens was a few milliseconds compared to the 30 fps frame rate of the camera. Consequently, our camera was the only module limiting the speed of imaging.

In the future, the camera will be replaced by an imaging fiber bundle and further Zemax simulations with be performed to find a proper fixed focal length lens to be placed at the tip of the fiber bundle.

2.1.5   Conclusions

In this study, the feasibility to use a simple to operate system has been established for future clinical study to generate all-in-focus images of upper airway tumor. This novel system can also be utilized to obtain clinical photographs of other diseases.

Acknowledgment

2.2 3D clinical imaging of Kaposi's sarcoma in the resource-limited settings

Abstract

Kaposi's sarcoma (KS) is the most frequently occurring cancer in Mozambique among men and the second most frequently occurring cancer among women. Effective therapeutic treatments for KS are poorly understood in this area. There is an unmet need to develop a simple but accurate tool for improved monitoring and diagnosis in a resource-limited setting. Standardized clinical photographs have been considered to be an essential part of the evaluation. When a therapeutic response is achieved, nodular KS often exhibits a reduction of the thickness without a change in the base area of the lesion. To evaluate the vertical space along with other characters of a KS lesion, we have created an innovative imaging system with a consumer light-field camera attached to a miniature photography studio adaptor. The image file can be further processed by computational methods for quantification. With this novel imaging system, each high-quality 3D image was consistently obtained with a single camera shot at bedside by minimally trained personnel. After computational processing, all-focused photos and measurable 3D parameters were obtained. More than 80 KS image sets were processed in a semi-automated fashion. In this proof-of-concept study, the feasibility to use a simple, low-cost and user-friendly system has been established for future clinical study to monitor KS therapeutic response. This 3D imaging system can be also applied to obtain standardized clinical photographs for other diseases.

2.2.1 Introduction

It cannot be over-emphasized that high-quality images are critical for clinical decisions. The current trend of establishing electronic health record (EHR) in the resource-rich settings and mobile device-based health care system to reach patients in the resource-limited settings makes standardization and acquisition of high-quality clinical photography an imperative issue. Standardization of clinical images is not only crucial for disease diagnosis, patient follow-up, clinical communication and medical education, but also for computer-aided clinical management. While nearly all of the radiological imaging systems, e.g. plain X ray, CT, MRI and ultrasound, have standard guidelines for obtaining and interpreting images, there is little consensus or effort in clinical photography except for a few areas, such as presenting the outcome of a plastic surgery. In fact, many diseases can be diagnosed by their characteristic presentations before any further confirmation tests. Several medical journals, such as the New England Journal of Medicine (Images in Clinical Medicine and Image Challenge) [46], Journal of American Medical Association (Clinical Challenge) [47], British Medical Journal (Picture Quiz), etc., frequently publish typical diseases that may be diagnosed through the analysis of a single clear and informative image. In 1989, The AIDS Clinical Trial Group (ACTG) proposed a KS staging system using a three-tiered system that classified the extent of tumor (T) involvement, the status of a patient's immune system (I) assessed by CD4 cell count, and the severity of their systemic illness (S) as good risk or poor risk [48]. The ACTG staging system and variants that are used to assess KS therapeutic response may include lesion counts, assessment of lesion color, nodularity, ulceration and associated edema,measurement of sum of the product of the diameters of 5 marker lesions, and evaluation for oral KS and secondary effects of KS [48, 49, 50]. The color and degree of nodularity of KS lesions are difficult to quantify, but often provide important information about response to treatment [48]. While conventional

photography is probably the single most useful technique for imaging KS, it does not provide enough information about tumor nodularity and other important characteristics. In contrast to what many would think, obtaining highquality clinical photography is not trivial [51, 52, 53]. The suggestion of using professional clinical photographers in the professional studio settings to control the surrounding environment for light, angle etc. is not overstated for producing clear and informative photographs. However, a photographer cannot focus on a relevant lesion unless he or she has been told by an experienced clinician. Therefore, it would be difficult to generate informative images without knowing where to focus. To overcome this dilemma and to ease the technical hurdles, we have developed an innovative approach by taking advantage of the light-field photography in conjunction with a design of a miniaturized photography studio to control environment and standardize the image presentation. Here we present a proof-of-concept approach for developing a 3D image based system to monitor therapeutic response of Kaposis sarcoma in Mozambique. While this system is developed for clinical photography, applications exist for other areas that require collecting evidence by non-professional personnel in field, including applications for veterinary, agriculture, and even crime investigation.

2.2.2 Methods and materials

3D Imaging System Camera

A consumer light field camera, Lytro [54, 55, 56, 57], was used to develop a simple and reliable imaging system for producing 3D clinical photographs. This camera has an unconventional physical appearance that is convenient for our imaging system design. It has a rectangular prism shape (1.61x1.61x4.41 inches, 7.6 ounces) with the lens at one end and a touch screen at the other (Figure 2.7E). Instead of focusing on

a single focal plane, Lytro, a digital light field camera, samples each individual ray of light that contributes to an image [54]. To record the light field inside the Lytro camera, a microlens array is placed in front of the photosensor. This idea originated from an earlier plenoptic camera proposed by Adelson et al. [58]. In the Lytro camera, each microlens covers a small array of photosensor pixels. The microlens separates the light that strikes it, and focuses it into a tiny image on this array, forming a miniature picture of the incoming light. The raw image is not readily recognizable by human eyes. Through ray-tracing techniques, images of multiple focal planes can be generated.
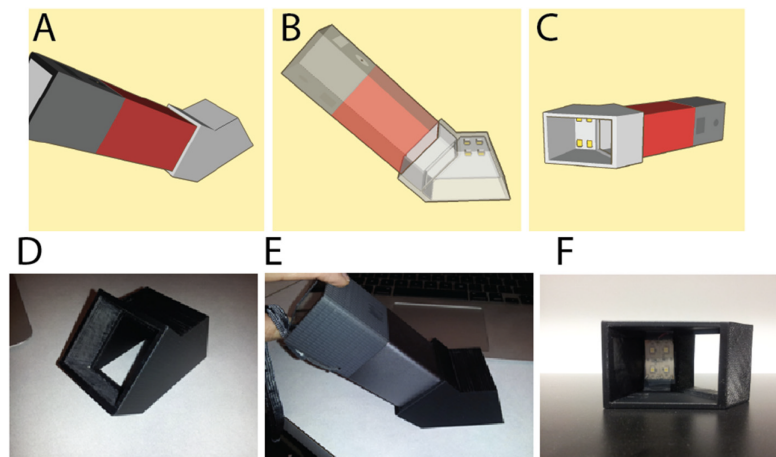
Figure 2.7: Design and Assembly of the miniature photography studio adaptor. The adapter was designed with SolidWorks CAD program (**A-C**) and was 3D printed (**D**). The adapter can be attached to a Lytro camera at 45° angle (**E**) and provides illumination through LEDs (**F**).

Miniature Photography Studio Adaptor

The adaptor was designed to create a standardized background environment for the Lytro snapshot by fulfilling the mechanical, optical and post processing requirements. It is to be placed at the front end of the Lytro camera and holds the camera at 45 degree with respect to the skin (Figure 2.7). The SolidWorks software was used to design the mechanical structure of the adaptor. It consists of two conceptual parts that are attached

together and then 3D printed as a single element. The Dimension 1200es 3D Printer from Stratasys Company was used for this purpose. The layer thickness of the printer is 0.254 mm (.010 in.) and it uses ABSplus (acrylonitrile butadiene styrene) [59] that is resistant to alcohol and is therefore suitable for sterilization purposes. Different views of the CAD (Computer-aided design) structure can be seen in Figure 2.7A-2.7C. Designed to enable optimal object illumination, the adaptor consists of a matrix of two by two strip LEDs (Figure 2.7C and 2.7F) along with a switching circuit that are installed and fitted on the adaptors top surface.

Kaposi sarcoma lesions

Anonymous clinical photographs of KS lesions were obtained from the Derma-tology Service at the Maputo Central Hospital (MCH) in Maputo, Mozambique. The great majority of patients (>90%) with KS at MCH are infected with HIV, and many are diagnosed as HIV positive at the time that they present with KS. Ten to fifteen patients with KS are admitted to the Dermatology service at MCH per month. Currently, MCH physicians document treatment response in the clinical chart using sketch diagrams and verbal descriptions.

All-focused image and 3D image model

Using a program modified from an open source python library, lfp-reader-2.0.0 [60], the original Lytro image file (.lfp) was extracted to obtain JPEG images (usually 12) of different focused depths, and a corresponding depth map was generated. We used batch processing to generate 12 JPEG files, a depth map and an all-focused image. The procedure was controlled through a graphic user interface (GUI) for ease of code execution. The final data was outputted into individual folders for each Lytro image set. Another GUI program was created for rendering the 3D model of each Lytro image

data using the aforementioned depth map and all-focused image. This program is a modification of the code from a command-line based C program [61]. We also used a computational software program, Mathematica, to perform a final 3D display with interactive rotation capabilities. As inputs, Mathematica receives the depth map, stored in ASCII format, as well as the corresponding all-focused JPEG. Our customized display script calls the Mathematica function ListSurfacePlot3D to generate the 3D shape from the depth map. Within this function, Mathematicas PlotStyle option is called to texture the rendered 3D shape with the allfocused JPEG. Once the fully textured 3D data is displayed, Mathematicas standard interactive tools may be used to rotate the object around any of the three dimensional axes.

Evaluation of relative volume change

The relative volume change was evaluated by a prototype software program that uses the projected area of a lesion to derive an average radius. The average radius is then used to approximate a three-dimensional volume. The prototype software program carries out these procedures by first counting the number of pixels, in a single 2D digital image, occupied by the object. This number of pixels represents the objects projected area, in relative units. In order to convert this into a signature radius, the program generates a hypothetical circle whose area, in pixel units, is equal to the objects projected area. Using the formula for the area of a circle, Area = $\pi(\text{radius})^2$, the program solves for a radius, in units of pixels, using the aforementioned measured area. This procedure is repeated for each unique perspective snapshot, and the radii are averaged. The camera adaptor (Figure 2.7) ensures that the distance to the object remains constant between the unique perspective snapshots. The averaged radius value is then converted into a volume, in units of cubic pixels, using the formula for a sphere, Volume = 4/3 $\pi(\text{radius})^3$. This value represents a signature relative volume, which may be used to measure fractional

relative changes between a lesion that is photographed at different points in time. A challenge for the aforementioned technique is accurately identifying, in the digital image, the visual boundary between the lesion and the background skin surface, a step that is necessary in order for the program to accurately calculate the projected area. In our current proof-of-concept program, we have successfully applied two different methods for determining this boundary: (1) by utilizing the information in the depth map to separate the lesion from the background surface through differences in depth; and (2) by visual inspection and manual input from a user who traces out the edge of the lesion on a digital touchscreen. In test cases, both strategies proved effective for a range of images, though each method has its strengths and limitations. Method (1) successfully works as long as program parameters are carefully optimized for typical depth map shapes. While proving effective for a range of lesion types, it can be a risky strategy for lesions that may represent diverse sizes, depths, and viewing angles. For example, it has particular difficulties for shallow lesions, where there is little change in height between the lesion and the skin. Despite these drawbacks, an advantage of this method is that it is fully automated, once parameters are well tuned, and therefore avoids potential errors associated with human error. Method (2), lesion boundary identification by visual inspection, has proven in our tests to be the most accurate method and the most capable method for accommodating diverse lesion sizes and shapes. Its primary disadvantage is that it requires human input and therefore adds an element of potential subjectivity, and potential human error, into the procedure.

2.2.3   Results

Miniature Photography Studio Adaptor

The adaptor is used to maintain constant geometric conditions of the environment and to provide controllable illumination. Its development was motivated by our having experienced initial difficulty to obtain a reliable 3D image using the Lytro camera alone. The adaptor simplifies the effort to generate a 3D image with a single shot and to compare the images of lesions before and after treatment.

All-focused image and 3D image model

The original Lytro files (.lfp) were computationally extracted to output a series of images with a range of focus settings (Figure 2.8A) and to output a corresponding depth for each position in the image (B, depth map) (Figure 2.8). We have consistently obtained 12 JPEG files from each file extraction after we used the adapter described earlier. Before our current system was set up, the results were inconsistent, even after we chose a well lit space to improve illumination and used a tripod to control spatial factors (angle, distance etc.). We have observed that the effective depth of a Lytro snapshot can be severely compromised when there are background objects at far distance. The simple, miniature, photography studio adaptor substantially resolved previous issues of inconsistent image quality. The concept and operation of creating the all-focused image (Figure 2.8) and 3D model (Figure 2.9) are similar. Both procedures take advantage of the image files at different focal planes and and also the depth map, but separate computational programs are applied to generate two different outputs. For clinical application, the allfocused image can be used for quick screening purposes as the size of the file is small, usually around 80 kb (30 220 kb based on 185 snapshots). The size is appropriate as an attachment through cell phone transmission. On the other hand, the

3D image model provides a more realistic view of a lesion, but is more computationally intensive. To simplify the operation, we created a custom GUI program to facilitate users with little or no training in knowing how to process image files. This is particularly important in the resource-limited settings. In addition, we use both commercial (Figure 2.7A) and open source (Figure 2.7B) software programs to meet various needs (see Methods section). The scheme in Figure 2.8 also reveals the simplicity of this system, in terms of the level of human involvement, despite very complex computational operations. The figure represents 3 Lytro snapshots, which result in 36 (12×3) JPEG images of different focal planes, with multiple angles (0, 120, and 240 degrees, horizontally from a reference point). Therefore, using our system, 36 sub-spaces were sampled close to the lesion with very little human effort.

Evaluation of relative volume change

As previously described, a useful tool to monitor therapeutic response of KS is to evaluate changes of nodular lesions by observing the lesions thickness and volume over time [48]. However, the follow-up period for each patient was very short (<2 weeks) in our proof-of-concept study (see an example in Figure 2.9A). Therefore, we chose to use a model clay system (Figure 2.9B) to demonstrate a simple measurement that may be applied in a more comprehensive clinical study. Notably, clay molding allows a more precise measurement of the correlation between the true volume and the volume derived by computational modeling. While a full 3D rendering provides the most powerful information, a measurement of a lesions volume can also be achieved using conventional 2D snapshots (taken with either a traditional digital camera or a Lytro camera) and applying a software algorithm to approximate true volume from the projected 2D shape. Multiple perspective snapshots are not absolutely required, but the overall uncertainty improves with each independent perspective. The prototype

software program, written by our group, measures the projected area of a lesion and uses that information to derive an average radius. This average radius may then be used to approximate a three-dimensional volume. Figure 2.10B demonstrates the effectiveness of the software prototype when applied to a set of digital images of randomly shaped clay models. To evaluate the uncertainty on relative volume, we measured differences between observed relative volume, as measured by the prototype program, and true relative volume, as determined by independent knowledge of the clay source. In order to include a diverse range of potential shapes in our uncertainty evaluation, we supplemented these test case images with simulated images of a wide variety of target shapes, ranging from that of symmetrical sphere-like objects to long flattened shapes with extreme differences in relative dimensions (like 10:1 ratio between height and width). After processing both true and simulated images through the prototype program, the results of these tests indicated that, when three snapshots of a target are taken from independent perspective angles, the technique can successfully measure relative changes in volume with an uncertainty of 4%, as long as the second epoch shape represents an approximately enlarged, contracted, or unchanged version of the first epoch shape; this scenario represents the vast majority of KS diagnoses. In instances where the overall shape changes completely (for instance, like from a long cigar shape to a half sphere), changes in relative volume may be measured with an uncertainty of about 34%. The information gathered from this approach may be combined with that from other diagnosis techniques in order to flag growths that may deserve further evaluation by a clinician.
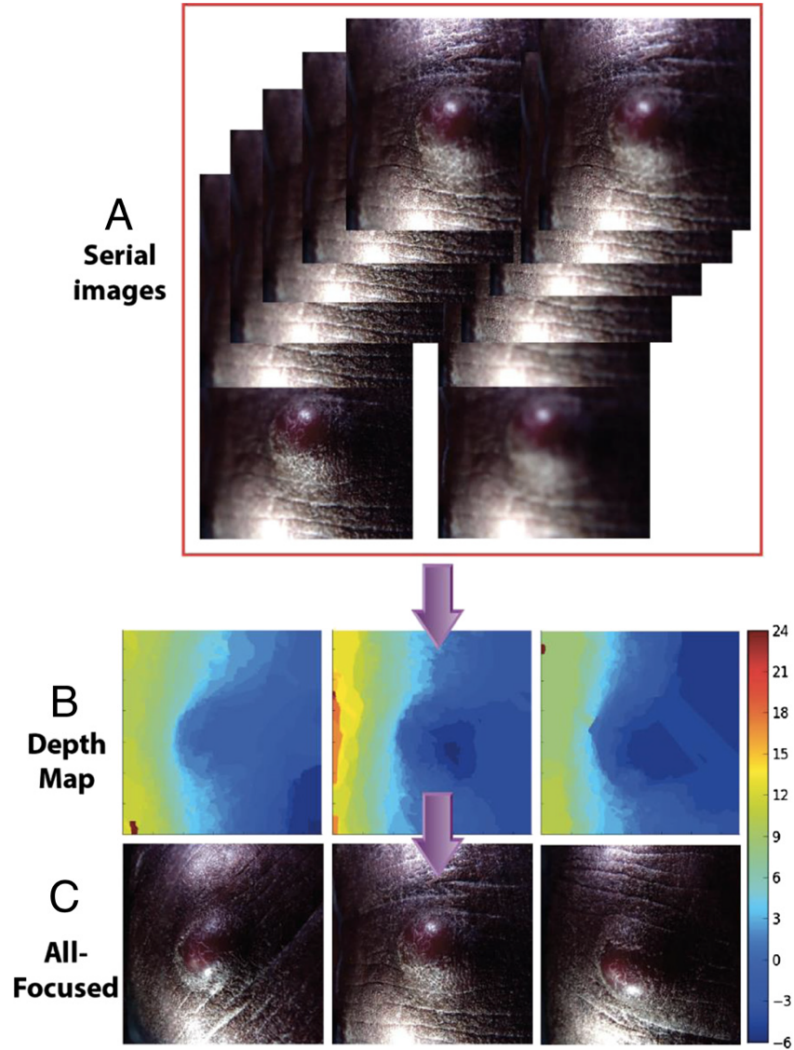
Figure 2.8: Construction of all-focused images. The original Lytro files were computationally extracted to output a series of images with a range of focus settings **(A)** and corresponding depths for each position in the image **(B**, depth map). Even with just a single Lytro snapshot (which contains 12 frames), an all-focused **(C)** image and a 3D model (Figure 2.9) can be constructed by combining the information from A and B. There are 3 all-focused images on panel C. They are derived from 3 single Lytro shots at different horizontal angles of the same KS lesion ($<$1 cm). Only one set of the serial images are shown (for the picture on the middle) in panel A.
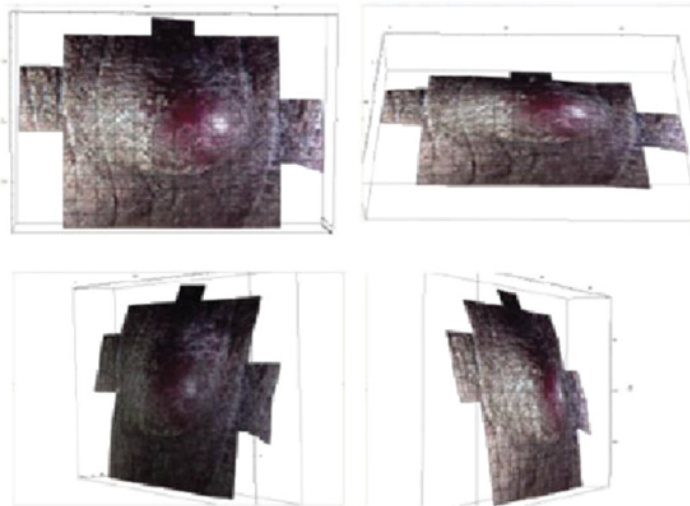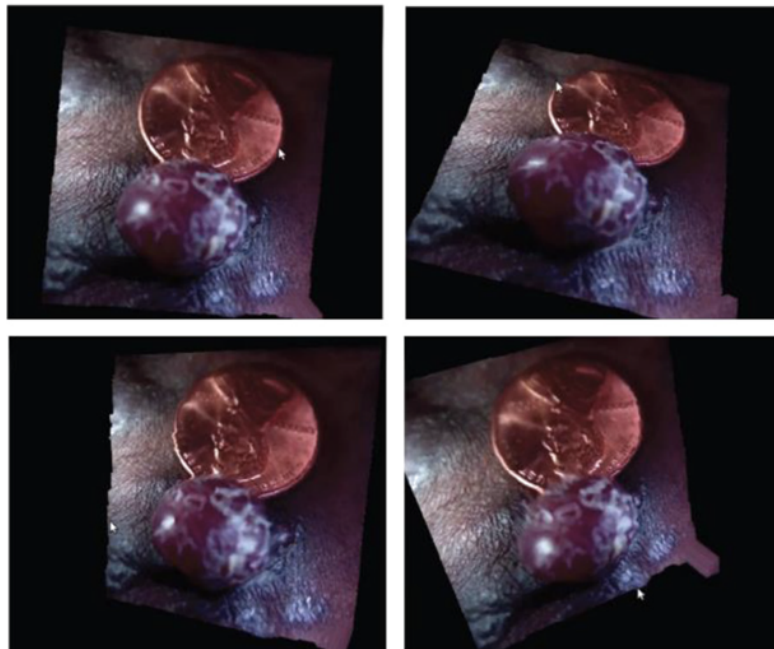
Figure 2.9: A 3D rendering of Kaposis Sarcoma, generated from a single Lytro snapshot processed by a prototype software using **(A)** commercial and **(B)** open-source platforms. Two examples are shown.
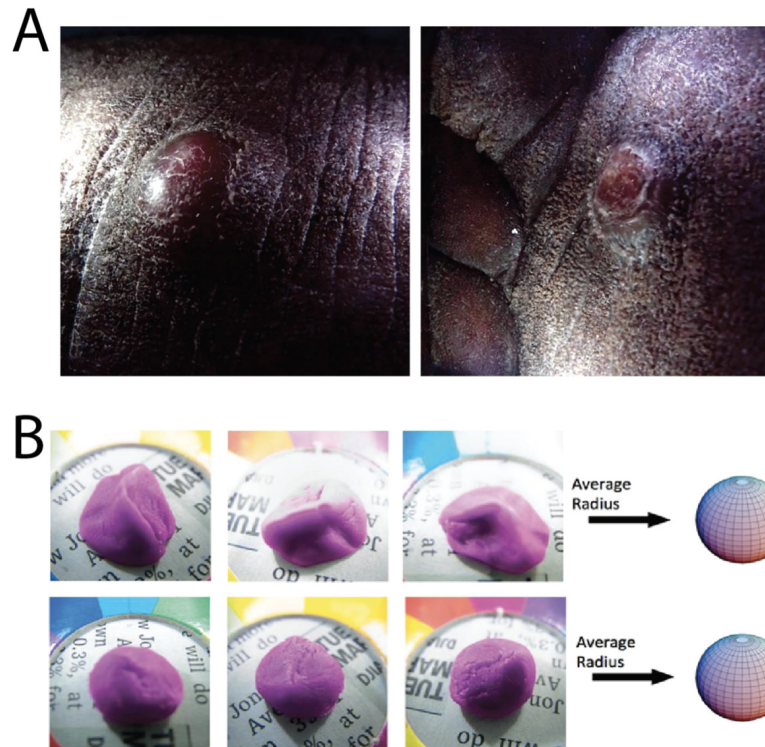
Figure 2.10: Changes of nodular KS lesions. **(A)** A pair of nodular KS lesions to demonstrate before (left) and after (right) treatment over 2 weeks. **(B)** The relative volume of two clay samples (one on top row and one on bottom row) is measured using the prototype image analysis software. Each column represents one of three independent angle perspectives. The program uses the projected 2D shape to measure an average radius. This radius is then used to determine a volume. For measuring relative changes in volume, the program can accurately deliver results with an uncertainty of 4%, as long as the changes represent solely an enlargement or diminution in an original shape, as opposed to a complete change in shape. In instances where the overall shape changes completely (for instance, like from a long cigar shape to a half sphere), changes in relative volume may be measured with an uncertainty of about 34%.

2.2.4   Discussion

An increasing number of digital technologies are being applied to promote virtual communication between patients and healthcare providers and medical specialists, without requiring face-to-face encounters. Accordingly, there has been a surging interest in utilizing mobile technology to meet the rising healthcare demand in developed countries, as well as to serve people living in a more resource-limited world.

An opportunity exists to apply a novel digital imaging technology to improve diagnosis and long-term monitoring of Kaposis Sarcoma (KS) in a resource limited setting. A recent report from Mozambique has shown that KS is the most frequent cancer among men and the second most frequent among women [62]. Remarkably, 20% (296/ 1507) of cancers diagnosed at the Maputo Central Hospital (MCH) are KS. The therapeutic response of KS may be different between this region and western countries, providing some of the motivation for effective monitoring tools [63]. Furthermore, in many cases, multiple KS lesions develop simultaneously, and may progress and regress independently. Unfortunately, relatively little is known about the varying response to treatment, and about the most effective therapeutic regimens [64]. Infrastructural inadequacies in the provisions of cancer care in sub-Saharan Africa pose great challenges for precise therapeutic monitoring. Therefore, there is an unmet need to develop a simple, but accurate, tool for improving diagnosis and long-term monitoring in such a resource-limited setting. While color and thickness of KS lesions are difficult to quantify, they provide important information about response to treatment [48]. Our simple and inexpensive imaging system and analytic software will resolve such a dilemma. Furthermore, the single processed all-focused images of the KS lesions were mostly around 80 kb (30220 kb for 185 snapshots). This file size is transmissible through a mobile phone for preliminary diagnosis or triage.

The myriad benefits of such a tool should not be underestimated. In medicine, as in many fields, a picture is often worth a thousand words. Photographs are important tools for recording and tracking the progression of visible lesions. Effective utilization of photographic techniques can help reduce the patient and physicians anxiety about adequate detection of lesion changes, help early identification and treatment of malignancy, and lead to fewer invasive procedures [65]. However, acquiring a clear, informative photo is not trivial. Apparently, one of the most obvious problems with conventional

photography is the burden of accurate focus on the target. Our recent adoption of an emerging technology, light field photography using the Lytro camera, succeeds in capturing multi-focal images with a single photo shot. However, we and others have often experienced frustrations in acquiring such ideal images [57].

Combining theoretical and experimental approaches, we were able to design an adaptor to serve as a miniature photography studio that enables reliable and predictable 3D image acquisition (Figure 2.7). Such an adaptor provides a controllable light source and enables standardized images (with a fixed camera-to-object distance and angle) for automated computational analysis. This is a very important step since, without this adaptor, image quality can suffer from day-to-day and person-to-person variations. Moreover, it makes the operation simple and intuitive, as one only needs the same level of skill required to use a smartphone or a digital camera. While our current software system is capable of producing a 3D image from a single Lytro snapshot (see Figures 2.8 and 2.9), our next-generation software should also be able to take advantage of instances where the clinical staff collects multiple snapshots to provide more comprehensive data.

We envision the light field camera as a useful general tool for clinical photography. There is no need to select focal planes because the Lytro camera records all of the light rays within a distance based on the setting. This is a very attractive function for a busy clinic that may lack trained personnel to take medical photography. Importantly, a clinician can review the images at other focal planes that may not be foreseen as necessary, but become crucial when a disease progresses. Furthermore, an all-focused image (Figure 2.8) or a 3D rotatable model can be created computationally, as shown in Figure 2.9. While we used a commercially available program (e.g. Mathematica) for fast, prototype-level, 3D image modeling, we plan to transition to an open-source, 3D modeling program. This final version is intended to integrate and streamline every aspect of the image processing, enabling a user-friendly automatic system that can be used in

the resource limited settings.

For surface volumetric analysis, we used a simple prototype software program, as previously described. There are many other computational methods for 3D volume measurement [66]. Clinically, it has been discussed whether more sophisticated medical imaging methods, such as CT and MRI, are more useful for measuring clinical outcomes [67]. It appears that the usefulness of a method is not only associated with the power of the computational algorithm, but also the limitation of the available technologies and practical requirements of standardization. Historically, the World Health Organization (WHO) proposed, more than 30 years ago, a system for obtaining cross-sectional images as a biomarker for therapeutic response [68]. For example, in this system a partial response is designated when bidimensional measurement of a single lesion shows greater than 50% reduction in cross-sectional area (as measured by perpendicular diameters). While the WHO criteria remain useful, an attempt to further simplify and standardize methods has been recently made [69, 70]. The response evaluation criteria in solid tumors (RECIST) were proposed by the European Organization for Research and Treatment of Cancer (EORTC) in collaboration with the National Cancer Institute (NCI) and the National Cancer Institute of Canada Clinical Trials Group. Interestingly, the RECIST criteria only made use of the one-dimensional measurement rather than the product of two perpendicular linear measurements. According to their system, a partial response is defined as at least a 30% decrease in the sum of the longest diameter of the target lesions. It appears that the RECIST criteria were designed to simplify the way to gather and record information, not necessarily to increase accuracy. Whether 1D, 2D or 3D models are more useful seems to be associated with the nature of lesions, and will be constantly debated [67, 70, 71, 72]. Nevertheless the variations of measurement should be reasonably small if the method is to be useful. In our study (Figure 2.10), the simple technique can successfully measure relative changes in volume (for longitudinal follow-up) with an

uncertainty of 4%, which is useful. But it would not be useful for horizontal comparison for two unrelated lesions (34uncertainty). We are currently exploring different techniques and expect to use multiple methods depending on conditions.

As described earlier, a critical factor for volume estimation is identifying the boundary of a lesion. We have applied two non-mutual exclusive approaches. A third potential method, that we have yet to test, is boundary identification through changes in color. This strategy holds some promise as either an independent technique or as a supplement to the aforementioned methods. It holds the potential to be fully automatable, but may require optimization for typical patient skin color and typical lesion color characteristics. Ultimately, the optimal technique for lesion boundary identification is an area of investigation that requires further development, perhaps in conjunction with a careful analysis of typical lesion characteristics. It may require some combination of the three described techniques. We defer such a detailed investigation for future work.

Although our report focuses on the application of our imaging system to potentially monitor therapeutic response of KS, the same approach can be applied for screening skin lesions, especially for longitudinal follow-up [65]. While early diagnosis and treatment is the best strategy for reducing cancer mortality, overuse of expensive and/or invasive procedures increases morbidity and healthcare costs in developed countries [73, 74] and is impractical in resource-limited settings. However, introduction of simple and inexpensive diagnostics and imaging devices has been proven to be useful in clinics. For example, the numberneeded- to-excise (NNE) value, a measurement for accuracy of melanoma diagnosis, has been improved only in specialized and not in non-specialized clinical settings in a multicenter study over a 10-year period [75]. The main difference has been attributed to a larger use of diagnostic techniques, especially the simple and inexpensive dermatoscope, and digital monitoring [65, 76]. As described earlier, our 3D imaging system may be especially useful in the telehelth settings as high-quality and

relevant images can be obtained without extensive training of the operator. Moreover, it is possible to have a preliminary analysis by a software system as standardized images are obtained.

2.2.5 Conclusions

In this proof-of-concept study, a feasibility to use a simple, low-cost and user-friendly system has been established for future clinical study to monitor KS therapeutic response. This innovative system can also be applied to obtain standardized clinical photographs for other diseases.

Acknowledgment

Chapter 2, in part, is a reprint of the material as it appears in the Journal of Translational Medicine, 2014, 12:169. Baghdadchi, Saharnaz; Liu, Kimberly; Knapp, Jacquelyn; Prager, Gabriel ; Graves, Susannah ; Akrami, Kevan ; Manuel, Rolanda ; Bastos, Rui ; Reid, Erin ; Carson, Dennis; Esener, Sadik; Carson, Joseph; Liu, Yu-Tsueng., "An innovative system for 3D clinical photography in the resource-limited settings". The dissertation author was the primary investigator and author of this paper.

Chapter 3

Fast vectorial incident and focused field calculations with high NA lenses

Abstract

The spin angular momentum of light has been used to rotate birefringent particles in the focal plane of optical tweezers systems. In order to achieve such rotation, circularly or elliptically polarized light is applied to a high NA objective lens. Despite light with uniform polarization in the back focal plane of a high numerical objective lens, the light at the focus is actually composed of an ensemble of polarization states that add up to give the resultant polarization in the focal plane. Correcting for this can give an optimized focal spot. Alternatively, by creating spatially varying polarizations in the back focal plane, arbitrary polarization states can be created in the focal plane. We discuss a novel method to calculate the required input field for creating beam foci with spatially varying polarization states. Such foci can be used for novel manipulation of birefringent objects. By using a spatial light modulator with the capacity to change polarization and phase, we can generate designed intensity and polarization patterns at the beam focus. Such

technology may have applications in optical nano-manipulation, optical microscopy and nano-fabrication.

3.1   Introduction

Since the pioneering work of Arthur Ashkin in designing the first optical tweezers, many researchers have used that principle to trap and manipulate small objects in the range of a few tens of nanometers to a few tens of micrometers [77, 78, 79]. Optical tweezers use tightly focused light with high intensity gradient at the focus that quickly drops as the light diverges. Particles with diameters significantly smaller than wavelength of light can be trapped when the gradient force overcomes the radiation pressure. The large particles with diameters greater than wavelength of the light, on the other hand, act like lenses. The light gets refracted when it passes through these particles and the refraction exerts gradient force due to the momentum change. In the opposite direction of the gradient force, the scattering force is applied to the particles due to the backscattered light at the particle interface. Larger particles can be trapped when the net forces on them is zero. The idea of trapping and moving inter and intra cellular sized particles in three dimensions, initiated several successful research fields and brought in promising results. For example, holographic optical tweezers were used to independently and simultaneously translate, rotate and cut semiconductor nanowires[80, 81]. Holographic kinoforms calculated by direct search algorithms were used to dynamically trap different particles and manipulate them in 3D [82]. In addition to the direct search algorithms, researchers used the Gerchberg-Saxton (GS) to rapidly calculate the required holograms to generate the desired intensity patterns in real time [83]. The GS algorithm is a phase retrieval algorithm that uses Fourier Transform to calculate the scalar complex 2D light field required to generate the target intensity pattern at the image plane of the focusing

lens. Due to its speed of convergence, the GS algorithm has been used to calculate holograms in real time at optical trapping experiments. Compared to the mentioned research groups that calculated the scalar field at the back aperture of an adjective lens to generate the desired intensity patterns at the focus, others studied the propagation and focusing of vector fields using a low or high NA objective lenses. E. Wolf [84] developed the vector diffraction theory of focusing beams and represented the vectorial electromagnetic field at the image space of optical systems with an integral. This integral was later on used as a tool to calculate the EM field at the focus for any arbitrary propagating vector field. A group of researchers used the Fast Fourier Transform to evaluate the Debye Wolf integral in calculating the vectorial field at focus of high NA lens [85] while others calculated the volumetric field distribution at the focal space of the high NA lenses using three dimensional Fourier transform [86].

In this work, we show a novel approach to calculate the required holographic phase pattern to generate the desired vectorial fields at the focus of high NA lenses. We introduce a new vectorial field design at the focus of high NA objectives that could trap nanoparticles and move them in the transverse plane. For this application, we pattern the vector field at focus with spatially varied polarizations and use the variable spin angular momentum of the focused light along with the designed intensity gradient to apply linear force on the particles trapped in three dimensions at the focus.

3.2 Methods and materials

When high NA objectives are used in an imaging setup, the paraxial approximation is not valid anymore and the field at the focus is not purely transverse, rather has a longitudinal component. To fully characterize the field at the focus of high NA objective lenses, one needs to calculate the 3D vectorial field at the focus. The vectorial field can

be calculated by numerically solving the Debye-Wolf diffraction integral. However, these calculations are time consuming and are not well suited for 3D beam shaping in real time. To increase the speed of vectorial focal field calculations, we used 2D FFTs on three components of the field in the Cartesian coordinate system. In order to take into account the effect of refraction at the interface of an objective lens, the EM components can be transformed from Cartesian into Cylindrical and then into the Spherical coordinates as illustrated in Figure 3.1. The e_ρ, e_ϕ, e_z are the unit vectors of the Cylindrical coordinate system and e_θ, e_ϕ, e_r are the unit vectors of the spherical coordinate systems. The field after the refraction, $E_{x,y,z}^1$, can be calculated from the incident field, $E_{x,y,z}^0$, by transferring it into the Cylindrical coordinate system, applying the refraction and then transferring it back to the Cartesian coordinate system. In equation Eq. 3.2.1, M is the Cartesian to Cylindrical coordinate transformation matrix and T is the matrix representing the effect of refraction at the lens interface.

$$
\begin{bmatrix} E_x^1 \\ E_y^1 \\ E_z^1 \end{bmatrix} = M^{-1}TM \begin{bmatrix} E_x^0 \\ E_y^0 \\ E_z^0 \end{bmatrix} \tag{Eq. 3.2.1}
$$

$$
T = A_0\sqrt{\cos(\theta)} \begin{bmatrix} \cos^2(\theta) - \sin^2(\theta) & 0 & 2\sin(\theta)\cos(\theta) \\ 0 & 1 & 0 \\ -2\sin(\theta)\cos(\theta) & 0 & \cos^2(\theta) - \sin^2(\theta) \end{bmatrix} \tag{Eq. 3.2.2}
$$

After applying the refraction on the EM field, the effect of focusing with lens can be represented as the Fourier Transform of each component of the field in the Cartesian coordinate system.
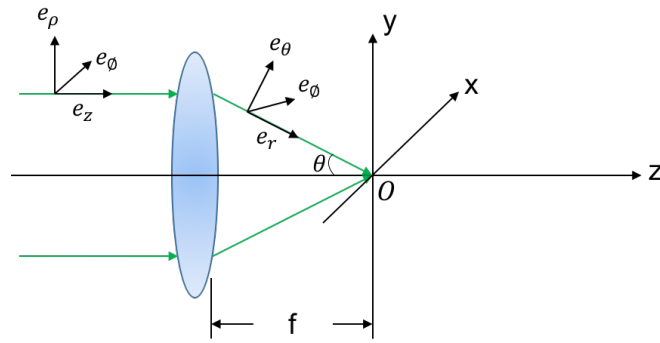
Figure 3.1: Refraction of the vector field at the interface of an objective. are the unit vectors of the Cylindrical coordinate system and are the unit vectors of the spherical coordinate systems.

Matlab Simulations

In this work, we used the proposed approach and investigated calculating the required phase distribution on the incident field that would result in the desired vector field at the focus of a high NA objective lens. For this purpose, we applied the Gerchberg Saxon phase retrieval algorithm for each Cartesian component of the field. Two sets of simulations were run in Matlab to find the required incident fields for generating the target fields with desired spatial intensity and polarization distribution at the focus. The first target field, as shown in Figure 3.2A, is a pattern of multiple Gaussian beams forming a smiley face, with eyes in x and y polarization and the lip consisting of left-handed and right-handed circular polarizations. The second target field is the pattern of UCSD ECE words illustrated in Figure 3.2B. UC letters have x polarization, SD letters have y polarization and ECE letters have circular polarization. The objective lens parameters used in these simulations were NA of 1.3 and focal length of 0.16 cm. The wavelength of the light was set to 532nm and the target fields were designed using 200×200 pixels.

As an application to the discussed technique, we proposed a novel spatial polarization distribution pattern at the focus that could apply translational movements on the trapped particles and used the developed method to calculate the required input field to
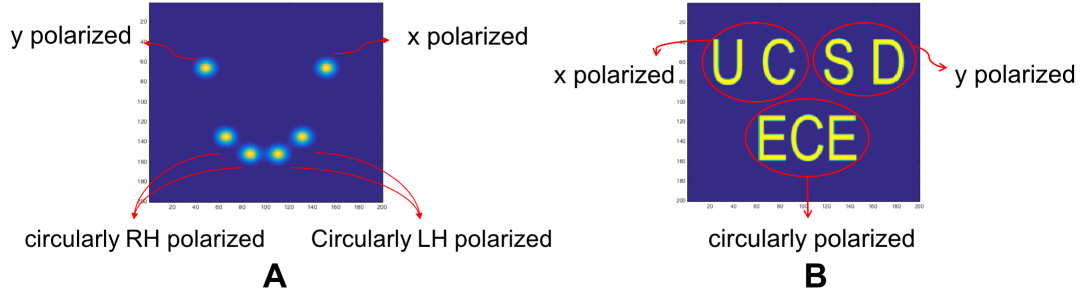
Figure 3.2: The polarization and intensity distribution at the focus for two target fields (**A** , **B**).

generate that pattern. In this design, we take advantage of the Spin Angular Momentum (SAM) of light and show that when two circularly polarized light with opposite SAMs are focused with a High NA objective to generate two line shaped intensity gradients, the resulted polarization distribution in between two lines is linear. As a result, the force applied on the particles trapped over lines is linear and will result in a translational movement on them. The intensity gradient over the lines will ensure that the particles will be trapped in the region with linear SOP. Figure 3.3 A,B and C show focusing two circularly polarized lights, the beam at the Cartesian coordinate system and the beam profile at the focus, respectively.

To examine the ability of our proposed design in generating translational movements, the field at focus was simulated by applying the phase patterns of two cylindrical lenses to each half of the input field and setting the state of polarization of each half to right and left handed circular polarization. For these simulations, 200×200 pixels input field, a laser light at 532nm and an objective lens with NA of 1.25 and focal length of 0.18 cm were used. At the next step, we used our proposed iterative algorithm to calculate the required input field to generate the designed optical field at focus. This would eliminate the need to use the fixed cylindrical phase patterns on the incident beam, providing the opportunity to dynamically control the line orientation, length and the
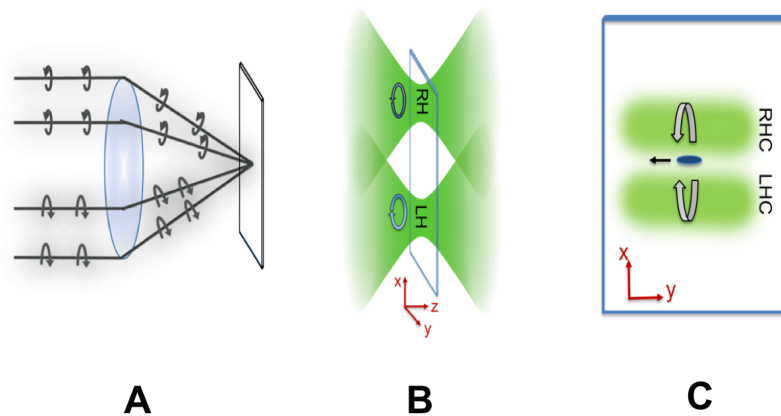
Figure 3.3: The field pattern for generating translational movement trapped at the focus. Two circularly polarized lights with opposite SAM are focused with a high NA objective (**A**). The field at the focus will have a variable polarization and intensity distribution (**B**) and (**C**).

direction of polarization.

Experimental Setup

In the experimental setup, a Verdi, 532nm CW laser and a Holoeye LC 2012 transmissive SLM along with other optical elements were used. To characterize the SLM and examine its limits in phase and polarization modulations of the incident beam, the setups in Figure 3.4 A and B were used, respectively. The polarization modulation was measured using Malus law by placing an analyzer between the SLM and the CCD camera and recording the light intensity transmitted from the SLM while displaying 0-255 gray levels on it. To measure the phase modulation, the Mach-Zehnder interferometry setup shown in Figure 3.4 B was used.

In the next step, the SLM was characterized using the Jones matrix to analyze its effect in modulating the phase and polarization angle of the incident vector beams. For this purpose, the SLM was modeled as consisting of several layers of nematic
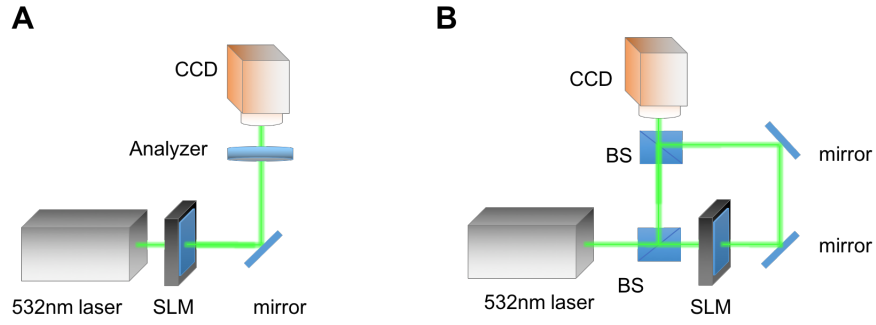
Figure 3.4: The setup to measure the polarization modulation **(A)**. The setup to measure the phase modulation **(B)**.

liquid crystals, where each layer applied a retardation and rotation modeled by separate Jones matrices [87][88] The Jones matrix of the whole SLM was represented as the multiplication of the Jones matrices of all the layers. Eq. 3.2.3 represents the Jones matrix (M) of an SLM calculated with the mentioned method. In this matrix, ϕ_1 and ϕ_2 are the phase shift on x-polarized and y-polarized light, respectively and

$$M = e^{-i\delta} \begin{bmatrix} A_1 e^{i\phi_1} & A_2 e^{i\phi_2} \\ -A_2 e^{-i\phi_2} & A_1 e^{-i\phi_1} \end{bmatrix} \qquad \text{(Eq. 3.2.3)}$$

The elements of matrix M were measured with the setup in Figure 3.5 by adjusting the half waveplate angle to 45° and 90° and the analyzer angle to 0° and 90°. The details of calculating these parameters are explained in reference [89].
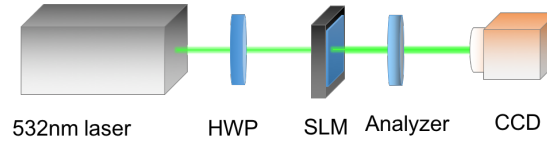
Figure 3.5: The setup to measure the Jones matrix components of the SLM.

According to the results of the characterizations, our SLM was not able to generate the whole range of 0° to 90° polarization angles. Thus, to experimentally generate two opposite handed circular polarizations, a hologram of two cylindrical lenses was applied

to each half of the SLM to generate the desired light intensity distribution at the focus for the purpose of trapping particles. To apply the circular polarization on each segment of SLM, two linear polarizers perpendicular to each other and a quarter waveplate in front of the SLM were used. Figure 3.6 shows the setup that was used for this experiment.
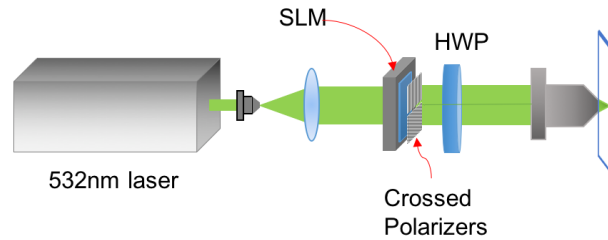
Figure 3.6: The setup to generate circularly polarized line traps.

3.3   Results

Simulation Results

The required phase to generate the polarization and intensity distributions shown in Figures 3.2 A and B, was calculated using two Gerchberg Saxon algorithms for each x and y polarization component of the incident beam. Figure 3.7 and 3.8 show the calculated phase and the resulting intensity patterns on E_x (A) and E_y (B) for the smiley face and UCSD ECE target patterns, respectively. The 200×200 pixel sized fields were used for these calculations.

The target and calculated values of (the direction of polarization) at the focal plane for the smiley face target are illustrated in Figure 3.9. The eyes of the smiley face consist of x and y polarized light, so the value of in those regions is equal to zero, while the part of the lip constructed with right handed circularly polarized light has lowest value compared to the parts with left handed polarization at highest σ value.
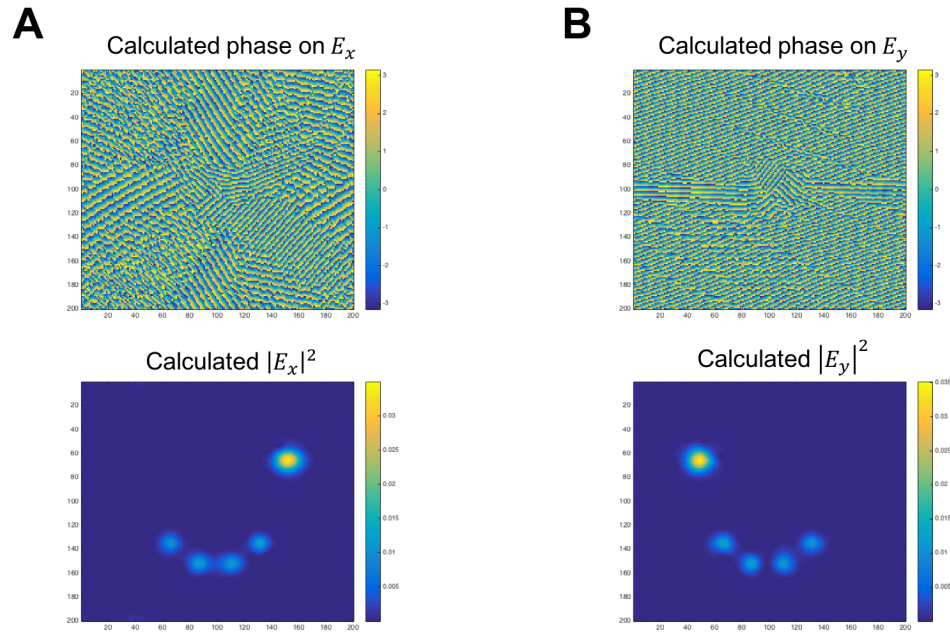
Figure 3.7: The calculated phase for the x and y polarization components of the input beam (**A , B**) and their resulting intensity patterns at the focus for the smiley face target.

Figure 3.10 shows the speed of calculating the phase of the incident light vs the number of pixels constructing the field for the smiley face pattern. The error bars show the standard deviation of calculations for each field size. A Macbook Air with 1.7 GHz intel Core i5 was used to calculate the simulations. The number of iterations in the algorithm was set to 100 so that the largest calculated filed with 1024×1024 pixels would have 90% correlation with the target field for any of the polarization states. As can be seen in this figure, fields with the size of 512×512 pixels can be calculated in less than half a second that makes this method suitable for real time calculations.

Simulations of the line intensity gradients with opposite SAM

Figure 3.11 shows the simulation results of calculating the intensity and polarization distributions at the focal plane corresponding to the implemented cylindrical phase
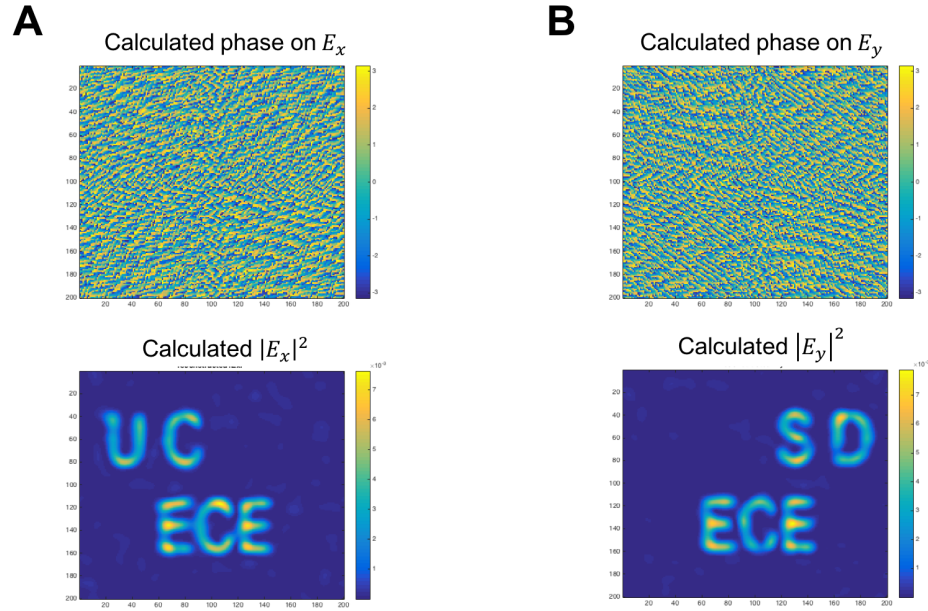
Figure 3.8: The calculated phase for the x and y polarization components of the input beam **(A , B)** for the UCSD ECE target and their resulting intensity patterns at the focus.

patterns on the input field. Figure 3.11A shows the value of , the direction of polarization, at the focal plane. Figure 3.11B shows the intensity gradient and the SOP at the focal plane. Figure 3.11C shows a closer look at the SOP over the focused lines. As can be seen in this figure, the SOP in the middle of the two lines is linear, which results in a linear force applied on a particles trapped over the lines.

Figure 3.12 shows the results of Matlab simulations for the intensity gradient and polarization distributions at a few planes below and above the focal plane in z direction corresponding to the incident beam encoded with two cylindrical phase patterns. As can be seen in this figure, since the SOP and intensity gradient follow the designed patterns at three wavelengths above and below the focal plane, the particles can be trapped in 3D at focus. Figure 3.12 A and B show the intensity gradient and polarization distribution at z = -3 times lambda to z = 3 times lambda, respectively.

To dynamically generate and control the length, orientation and polarization
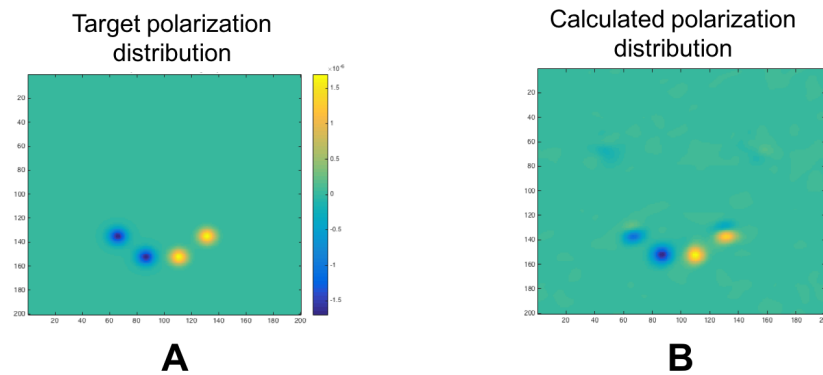
Figure 3.9: The target **(A)** and calculated **(B)** spatial polarization distribution. Right handed circularly polarized light with lowest intensity is shown by blue color and left handed polarization with highest intensity is shown by yellow color.
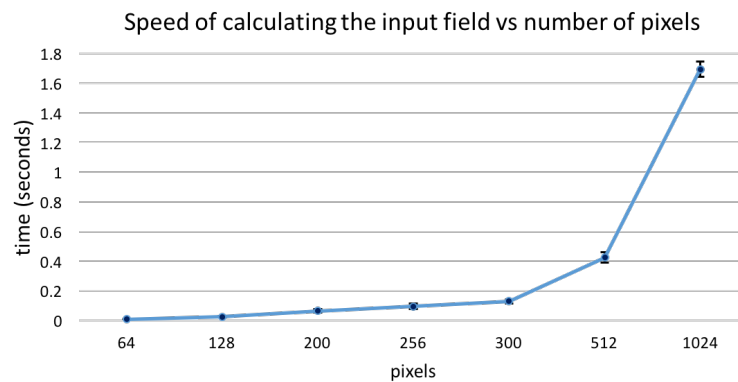
Figure 3.10: The speed of calculating the required input field to generate the target intensity and polarization distribution vs the number of pixels constructing each field.

direction of the proposed line patterns at focus, the iterative input field calculation method was used. Figure 3.13 shows the calculated phase for the input field and the resulting intensity patterns on Ex and Ey. Since the SOP on both lines is circular with opposite directions, a similar intensity distributions appear on the x and y polarization components at the focus.
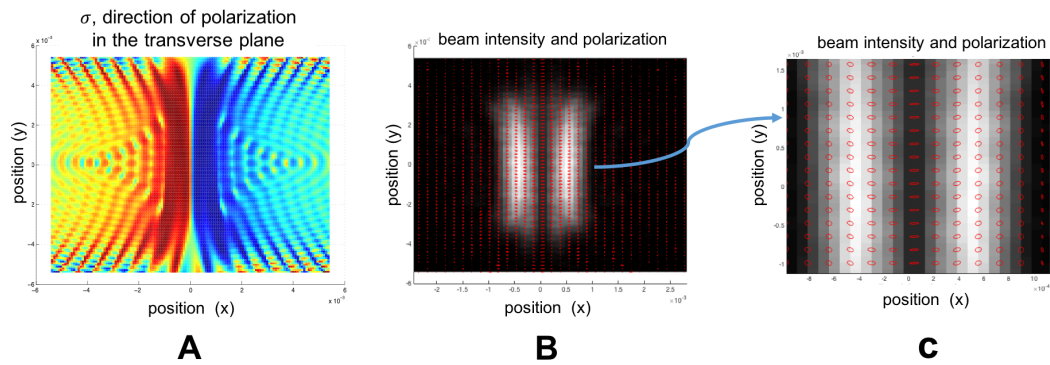
Figure 3.11: The direction of polarization at focus **(A)**. The blue color shows right handed polarization and red color shows left handed polarization. The intensity gradient and polarization ellipses at the focus **(B)**. A zoomed-in version of panel **(B)**, illustrating the linear polarization along the line trap **(C)**

Experimental Results

The Holoeye LC 2012 transmissive SLM was characterized by measuring the phase shift and the change in the polarization angle caused by each 0-255 gray level of the SLM on the incident light as shown in Figure 3.14 A and B, respectively.

Figure 3.15 shows the results of vector characterization of the SLM. Graphs A-D in this Figure represent the measured values of the elements of the Jones matrix (A_1, A_2, δ, ϕ_1 and ϕ_2) of our SLM.

To generate the line intensity gradients at two opposite handed circular polarization, the hologram of two cylindrical lenses was applied on the SLM and the SOP of the transmitted light was set to circular polarization with opposite SAMs. Figure 3.16 shows the intensity distribution at the focus generated by the experimental setup compared to the simulated field using the same beam and objective parameters.
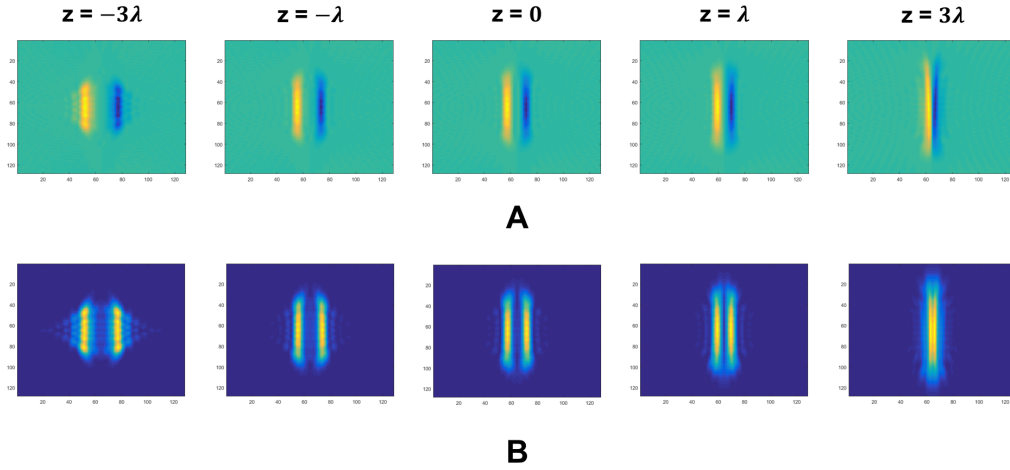
Figure 3.12: The simulation results of the intensity and polarization distributions of the proposed design at a few layers below and above the focal plane.

3.4 Discussion

High numerical aperture objective lenses are required to trap and and manipulate small sized particles at the focus. These objective lenses provide the necessary gradient force at the focus to overcome the scattering forces. However, when high NA lenses are used in an optical setup, the paraxial approximation is not valid anymore, and one needs to solve the problem of vectorial field propagation to fully define the vector field at the focus. Although the vectorial field calculations can be carried out by numerically solving the well-established Debye-Wolf integral, these calculations are time consuming and are not suitable for real time applications. In our approach to rapidly calculate the vector field at the focus and the required phase pattern on the incident light to generate the desired fields at focus, we took advantage of the in-built Fast Fourier Transform library of Matlab. To take into account the effect of refraction of the vector field at the objective lens interface, we rotated the unit vectors at the interface and calculated the projection of the vector field components on the transformed unit vectors. We then used 2D FFT functions to calculate the vector field at the focus. We integrated this method

A

Calculated phase on E_x

Calculated $|E_x|^2$

B

Calculated phase on E_y
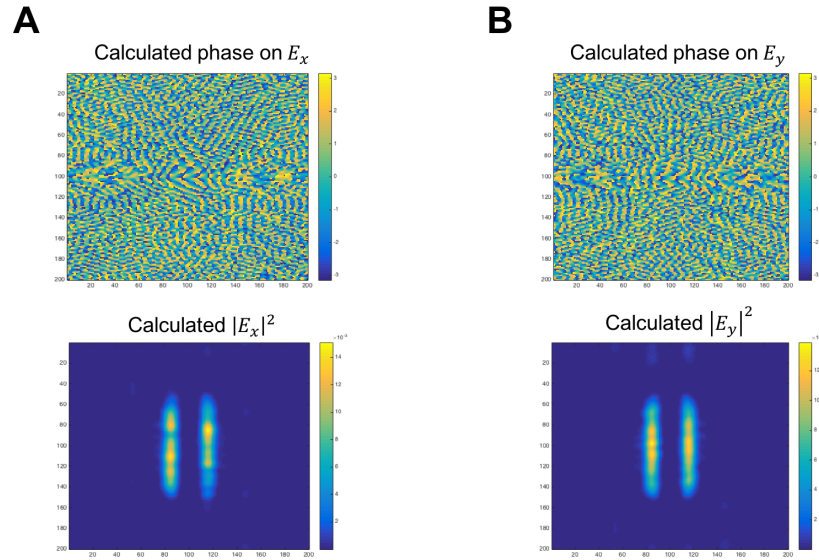
Calculated $|E_y|^2$

Figure 3.13: The required input filed phase and the resulting intensity gradient for the focused line patterns with the left and right circularly polarized light, calculated using the proposed iterative method. **(A)** The phase of the incident field and the intensity pattern at focus, calculated for the x polarized light. **(B)** The phase of the incident field and intensity pattern at focus calculated for the y polarized light.

into the Gerchberg-Saxon phase retrieval algorithm to calculate the required input field to achieve the desired polarization and intensity distributions at the focal plane of an objective. The simulation results illustrated in Figures 3.7 and 3.8, show the ability of our proposed method in calculating the required input fields to generate the test Smiley Face and UCSD ECE vector field patterns at the focus. For 200×200 pixel sized fields, the target vector fields were generated after 15 iterations. The very short time required to carry out these calculations makes our approach suitable for real time focused field shaping applications. The graph of Figure 3.10 shows that a 128×128 pixel sized field can be calculated in about 25ms.

We also proposed a novel vectorial focused field design, that could generate translational movement on the trapped particles. In this design, two patterned circularly polarized beams with opposite SAMs are focused with an objective, forming two line shaped intensity gradients at the image plane of the objective. The results of simulations
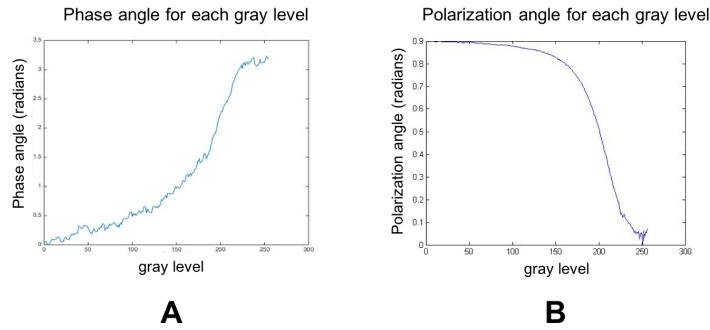
Figure 3.14: The phase modulation caused by each gray level of the SLM **(A)**. The polarization angle of the light transmitted from the SLM vs the gray levels on the SLM **(B)**.

in Figure 3.11 show that the the state of polarization in between the two lines is linear, which in turn indicates that the force applied to the trapped particles is linear hence pushing them upwards or downwards over the line taps. With the next set of simulations, illustrated in Figure 3.12, we investigated the state of polarization and intensity gradient at the vicinity of the objective focal plane along the z direction. These simulations show that both the SOP and intensity gradient will be maintained in a 3D space close to the focal plane of the objective lens. As can be seen in Figure 3.12, with the 532nm wavelength, the SOP and intensity gradient are consistent with the designed patterns in a $3\mu m$ range around the focal plane. This would ensure that particles can be trapped in 3 dimensions at the focus. Following the promising 3D SOP simulation results on the proposed line traps, we used our developed method to calculate the required input field for generating the proposed field at focus.

Performing the scalar and vectorial characterization of our SLM, we examined its limits in modulating the phase and polarization of the input light. As can bee seen in Figure 3.14, our SLM was not able to change the polarization angle by more than 0.9 radians and hence couldn't generate two orthogonal polarization angles. To compensate this, in our experimental setup, we used linear cross polarizers and a quarter waveplate to
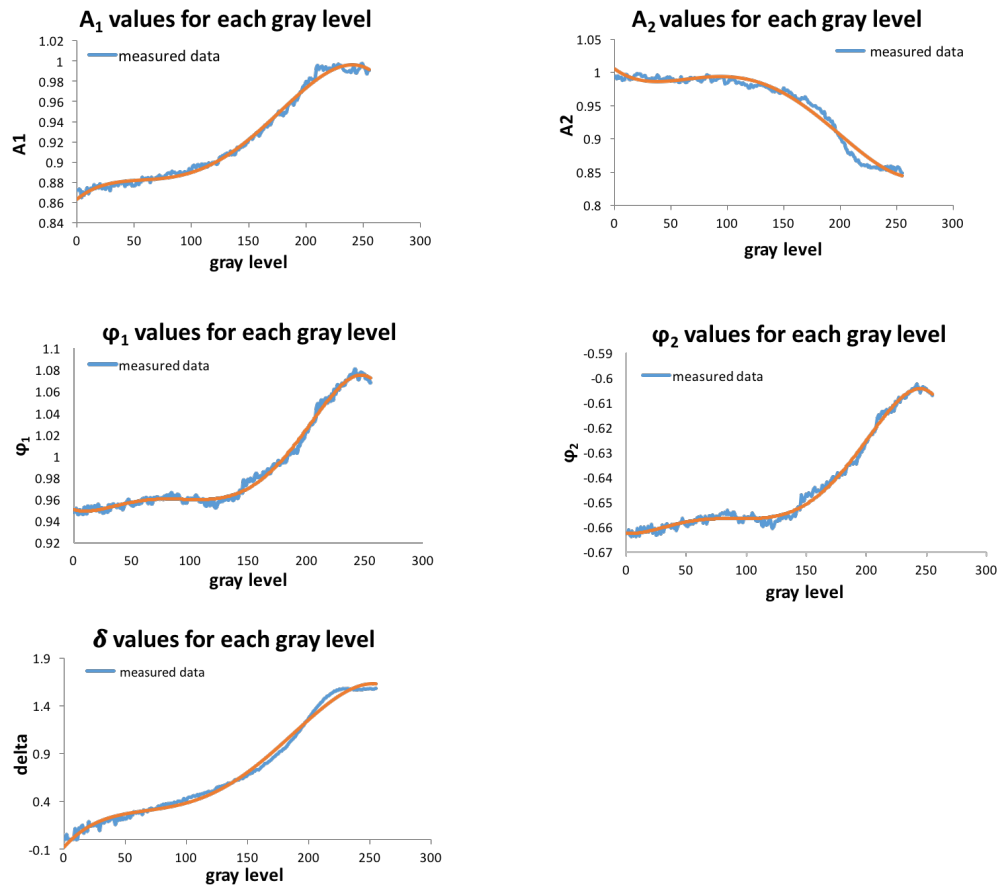
Figure 3.15: The measured values for the components of the Jones Matrix (A_1, A_2, δ, ϕ_1 and ϕ_2) for each gray level displayed on the SLM.

impose circular polarization with opposite SAMs on the light field transmitted from each half of the SLM.

3.5   Conclusions

A new method to rapidly calculate the vectorial focused fields and the required input fields to generate them is discussed here. In this method, after calculating the refracted beam at the interface of the objective lens, the FFT algorithm in Matlab was used to find the vectorial field at the focus. A vectorial format of the Gerchberg-Saxon phase retrieval algorithm was then used to find the required field to achieve the desired

Simulation Experiment

A B
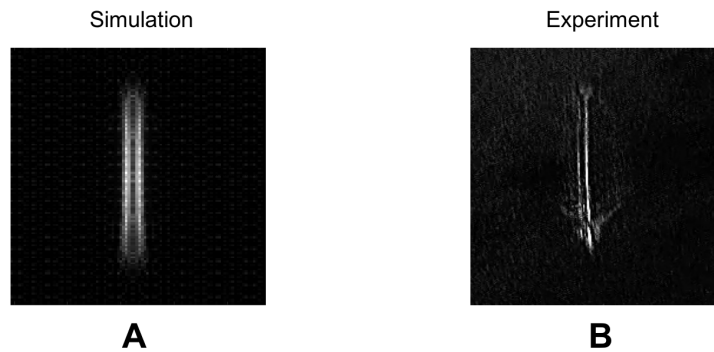
Figure 3.16: The comparison of line trap generated experimentally with the simulated one.

focused fields. We showed that the speed of our method in calculating the desired fields with 128×128 pixel sizes are in the range of 40 Hz, which makes this method suitable for dynamically shaping the field at focus in real time.

We also proposed a novel focused field, encoded with spatially varied polarization and intensity distributions and showed that the SOP over the central region of this design is linear, which would apply a linear force and generate translational movements on the trapped particles.

Future work will study the ability of this design in moving nanoparticles in an experimental setting and the size limit on the particles that can be trapped with this design.

Acknowledgment

Chapter 3, in full, is currently being prepared for submission for publication of the material. Baghdadchi, Saharnaz; Preece, Daryl; Esener, Sadik. The dissertation author was the primary investigator and author of this material.

Chapter 4

Imaging through scattering using spatially encoded optical beams

Abstract

One of the major challenges in imaging biological tissues is the scattering of the incident photons inside inhomogeneous media, which limits the number of image bearing ballistic photons reaching the recording device. Our single pixel imaging device takes advantage of a new set of spatially encoded projection patterns and generates an image of the objects hidden behind scattering materials by recording the backscattering diffused photons with a photodetector. It is a reflective imaging setup which makes it suitable for use in majority of biological image acquisition settings. The number of required measurements to reconstruct an image of the target behind a scattering material is very small and makes the approach suitable for live tissue imaging.

4.1 Introduction

When the light enters an inhomogeneous material, some of the photons, namely ballistic photons, preserve their direction of propagation and their phase information. In contrast, other photons get scattered as the light diffuses inside the medium. The standard image formation requires the ballistic photons to generate a clear picture of the target while the presence of the diffused photons results in a blurry picture. In extreme cases, when the thickness of the scattering material is much larger than its transport mean free path, obtaining a clear picture of the target with traditional imaging systems is not possible. Among the scattering materials, biological tissues are extensively studied substances [90, 91, 92, 93]. To overcome the problem of light scattering in tissues, several imaging techniques such as confocal imaging [94, 95], scanning multi-photon imaging, time-resolved detection [96, 97] and polarization sensitive imaging [98, 99] have been implemented in the past. These techniques rely on filtering out the diffused photons from all the transmitted or reflected photons received by the detectors and consequently are limited by the thickness of the the material that they can image through. For thicker tissues, the intensity of the ballistic part of the transmitted or reflected light will become too low that it cannot be used to generate an image. Some other techniques [100, 101, 101] based on speckle correlations have been implemented to generate images of the objects hidden behind scattering materials. These techniques use both the diffused photons and the ballistic photons to form an image. Despite their promising results, these techniques are limited by sub-millimeter thick scattering materials.

Recently, another promising technique is reported that is capable of imaging objects embedded in a few millimeters thick scattering material [102]. In this technique a single pixel camera [103, 104, 105] is used to record the scattered light from an object illuminated by a sequence of structured light patterns. Both coherent [106] and

incoherent [107, 108] light sources have been used for illumination. Single pixel imaging is quite similar to the computational ghost imaging [109] in that they both project random illumination patterns onto the object and record the transmitted or reflected photons using a photodetector. In both techniques, in contrast to transmission matrix measurement methods [110], no prior information about the target is required and the correlation of the incident light pattern and the recorded signal is used to infer the scene. However, in the computational ghost imaging technique, two copies of the incident light pattern are generated using a beam splitter and a CCD camera is used to record the illumination patterns. In case of single pixel imaging, a DMD (Digital Micromirror Device) or a SLM (Spatial Light Modulator) in coherent illumination and a projector in incoherent illumination are used to illuminate the target. In both cases, the incident light patterns are predefined by the user and they do not need to be recorded during the experiment. To improve the correlation efficiency, the light patterns based on Walsh-Hadamard matrices are used in these setups. In the image reconstruction part of the single pixel imaging techniques, CS (Compressive Sensing) algorithm [111] is often used. Compared to the raster scanning in which N single measurements are taken to calculate an N pixel image, in CS, M$\leq$ N measurements are taken for the image reconstruction. CS relies on the fact that many pictures are sparse in nature. It measures the inner product between the target and a set of projection patterns and recovers the image from the measurements using l1 optimization. One of the major advantages of the CS algorithm is that it reduces the data acquisition load, compensating it at the post-processing stage. This is in particular beneficial in applications like dynamic bio-imaging where high speed imaging is desired.

Although promising results are reported on imaging objects hidden inside scattering materials utilizing the single pixel imaging technique and CS image recovery algorithm, these results are limited to transmissive imaging and require a large number of measurements [102]. On the contrary, many biological tissues can only be imaged in a

reflective mode. Furthermore, minimizing the image acquisition time by reducing the number of the required illumination patterns is required in imaging the live samples.

Here, we present our work in designing projection patterns consisting of optical modes with phase singularities used along with a bucket detector and CS algorithm for imaging the objects hidden in scattering media. We show that our method substantially lowers the number of illumination patterns required to generate an image of the hidden object.

4.2 Methods and materials

The projection patterns

The resilience of optical modes with phase singularities against turbulence has been studied in the past [112]. Although the physics behind this resistance is still being investigated [113], it has been experimentally shown that optical modes such as Laguerre Gaussian (LG) modes [114] with helical phase fronts retain their ring shaped intensity pattern for a longer distance when they propagate inside scattering materials [115, 113]. In our method, we structured the illuminating light using LG modes in random locations within each illumination pattern. The intensity distribution of LG modes was calculated from Eq. 4.2.1.

$$u(r,\varphi,z) = \frac{A}{w(z)} \left\{ \frac{\sqrt{2}r}{w(z)} \right\}^2 L_p^l \left(\frac{2r^2}{w(z)^2} \right) e^{\frac{-r^2}{w(z)^2}} e^{\frac{ikr^2}{2q(z)}} e^{il\varphi} e^{i\varphi_{pl}(z)} \qquad \text{(Eq. 4.2.1)}$$

where

$$A = p! \left(\frac{2}{\pi p!(|l|+p)!} \right)^{\frac{1}{2}} \qquad \text{(Eq. 4.2.2)}$$

and

$$r = \sqrt{x^2 + y^2} \qquad \text{(Eq. 4.2.3)}$$

Matlab Simulations

Matlab simulations using the open source CS algorithm developed by [116] were performed to sample the target picture with the designed projection patterns and reconstruct the image of the target both in presence of a scattering material and without it. A 32×32 pixel smiley face picture was used as the target for the simulations. In order to take into account the effect of scattering material on the incident light and the sampled object located inside the material, projection patterns were blurred by applying a Gaussian lowpass filter with the sigma value of 0.5. The target picture was also blurred with the same lowpass filter and was sampled by the blurred projection patterns. Figure 4.1 shows a schematic of this process.

Projection pattern   Scattering material and the target   Blurred projection pattern   Blurred target
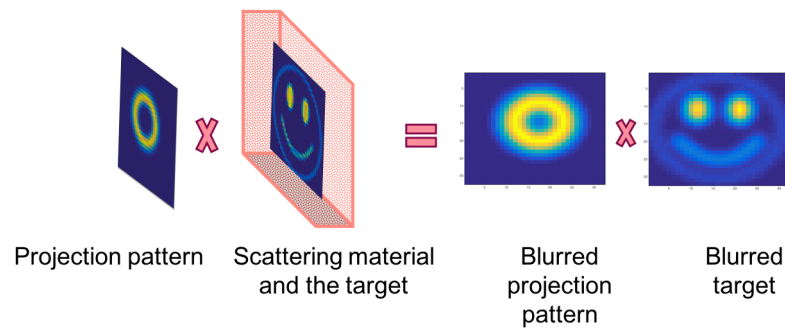
Figure 4.1: The schematic of the model used for the simulations. The projection patterns and the image of the target embedded inside an scattering material are blurred with a Gaussian lowpass filter and then multiplied to each other to model sampling the object with those patterns.

The 32×32 pixel sized intensity patterns consisting of LG modes were built using Eq. 4.2.1. Initial simulations showed that using concentric modes consisting of the modes with l =1:30 and p =0:20 orders in illumination patterns would result in ghost images

after the reconstruction. In order to solve this problem, the location of the modes in the projection patterns was randomized using a script that detects the the location of each mode and moves the center of the mode to a random location within each frame. The total of 6000 projection patterns were made using p = 0 and l = 1:30 modes with 200 displacements for each mode. Figure 4.2 shows three example projection patterns that were used in the simulations.

With 0.35 sub-sampling rate, 358 projection patterns out of the total generated ones were used for sampling the 32×32 pixel sized smiley face target. The matrices of the pattern intensities were multiplied to the matrix of the target intensity using the element-wise multiplication in Matlab and the sum of the total elements of the result matrix was used as the intensity of the backscattered light.
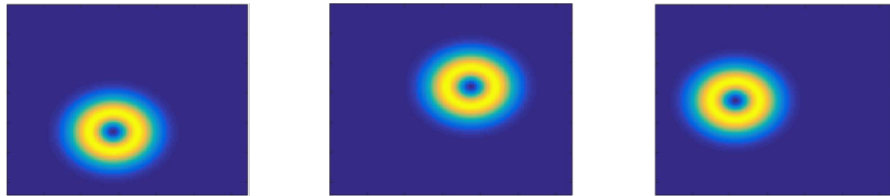
Figure 4.2: Three examples of the projection patterns used in the image reconstruction simulations.

Experimental setup

A diode-pumped solid-state (DPSS) crystal laser (DL633-050, CrystaLaser) at 633 nm wavelength with 50 mW output power was used for the illumination. The output of the laser light was spatially filtered with a pinhole and collimated with a converging lens. A polarizer was used as an attenuator on the beam path to adjust the intensity of the incident light. A reflective Liquid Crystal on Silicon (LCOS) spatial light modulator (Holoeye, LC-R 720) with 1280 x 768 resolution was used for the purpose of beam shaping. The reflected light from the SLM was spatially filtered using an iris to transmit

only the first order mode that contained the projection patterns. Each pattern consisted of a first order LG mode that was generated by applying the corresponding helical phase pattern on the SLM. A grating was also applied on the SLM to transmit the first order mode to the location of the iris for spatial filtering. Figure 4.3 shows the schematic of the illumination setup in panel A and the elements used in this setup in panel B. Figure 4.3 C shows a close up view of the laser and the spatial filtering system.
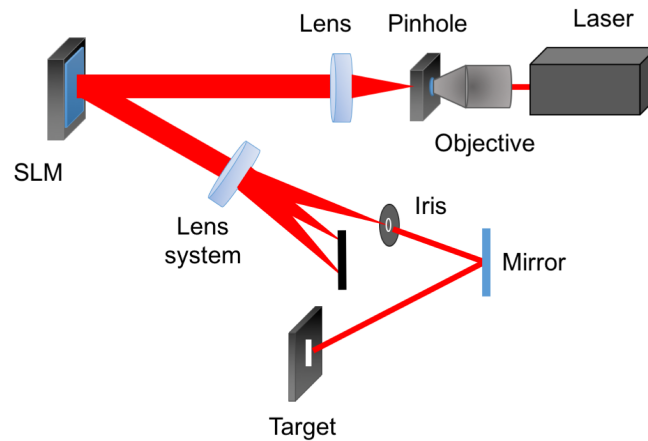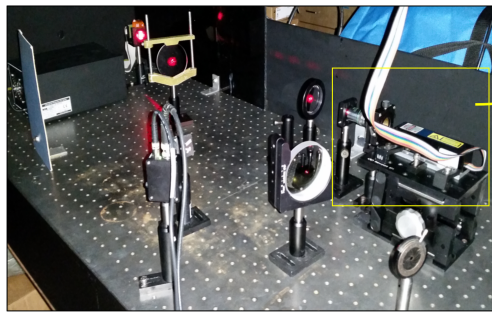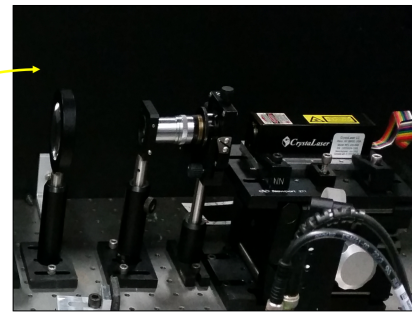
Figure 4.3: The schematic of the illumination setup consisting of a laser, spatial filtering system, collimating lens, SLM, the lens system, an iris, a motorized rotating mirror and the target **(A)**. The elements used in this setup **(B)** and a closeup view of the laser and the elemenst used for collimating its output light **(C)**.

A motorized mirror was used to project the incident light onto the object. To rotate the mirror, a Newport motion controller (ESP300) with linear actuators (CONEX-TRB25CC) was used. The manual knobs of the mirror were replaced with two actuators to rotate the mirror using the motion controller and consequently steer the beam on the target. To record the backscattered light from the target, a Si-Avalanche photodetector (Thorlabs, APD 120A2) along with a NI USB-6000 DAQ device were used. Since the computer interfaces on the discontinued ESP300 motion controller did not properly work, the beam steering was done manually using the front panel interface. As a result, a camera was used to image each pattern projected on the target. Figure 4.4 shows the location of the object, photodetector and the camera in the setup.

Selection of the target and the scattering materials

Several experiments with different targets were performed to test the validity of the proposed method in generating an image of the objects with and without the presence of a scattering material. The first set of experiments were performed using a white 6×19 mm^2 rectangular paper taped on a black background frame with 25×25 mm^2 dimensions shown in Figure 4.5 A. The second target was a white circle shaped paper with diameter of 1 mm taped to another black frame with the same dimensions as depicted in Figure 4.5 B. For the third object a T-shaped letter made with a white paper was used. The thickness of the letter was 1mm and the same black frame was used for the third target. The other dimensions of this target is indicated in Figure 4.5 C.
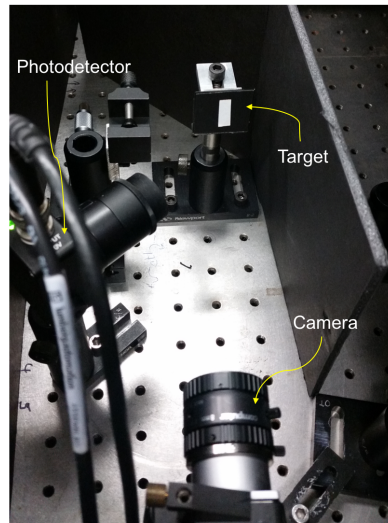
Figure 4.4: The detection setup including a photodetector, a camera and the target.
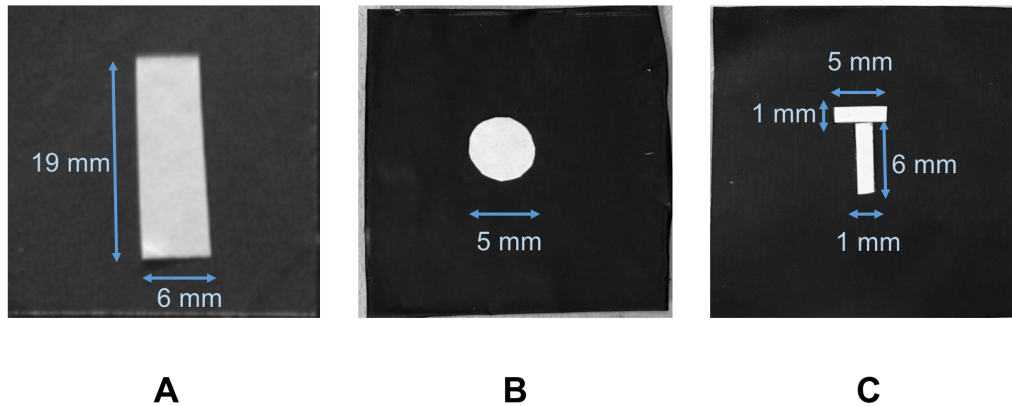
Figure 4.5: The three objects used as targets in the experiments. All three of the objects are made with white paper, cut in different shapes.

To mimic the effect of scattering, a clear light diffuser was used for the experiments with the rectangular object. Figure 4.6 shows the diffuser in panel A and the diffused beam over the object placed behind the diffuser in panel B. For the T-shaped objects, 60 cc diluted milk at 1.7% concentration was poured inside a 10 mm thick clear container and placed in front of the T-shaped target. This concentration corresponds to

the transport mean free path length of the whole milk that is about about 1 mm[117, 118]. Figure 4.7 A and B shows the diluted milk inside the container and the concealed target behind it, respectively. As shown in panel A of this figure, the target is completely concealed behind the milk and cannot be seen with a regular camera.

A   **B**
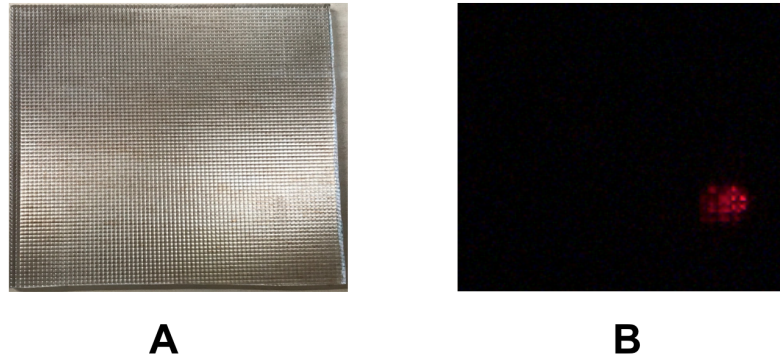
Figure 4.6: The clear diffusion glass used as the scattering material for the rectangular-shaped target (**A**). The diffused beam that is projected over the target (**B**).

A   **B**
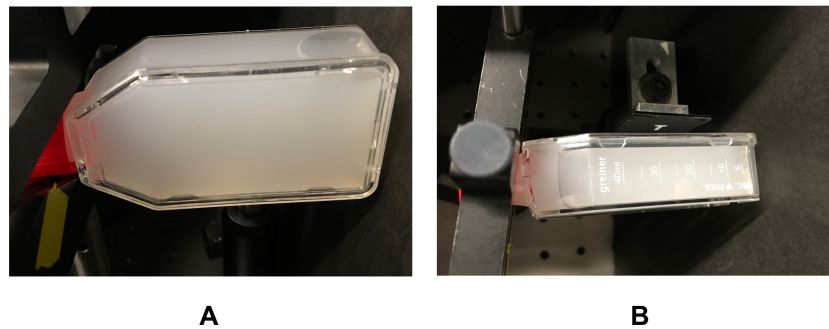
Figure 4.7: The diluted milk used as the scattering material for the T-shaped target (**A**). The target is located behind the milk container (**B**).

4.3 Results

Simulation Results

Figure 4.8 B and C shows the reconstructed images of the 32×32 pixel smiley face target with and without the presence of turbulence, respectively. In panel A of this Figure, the original target is included for comparison. In total, 358 projection patterns corresponding to the sampling rate of 0.35 were used for these reconstructions. The 2D correlation function in Matlab was used to compare the reconstructed images with the original image of the target taken by a camera without the presence of scattering. The reconstructed smiley face (Figure 4.8B) in absence of scattering had 94% correlation with the original picture and the image reconstructed from the measurements taken with blurred projection patterns and the blurred original picture, had 93% correlation.

A **B** **C**
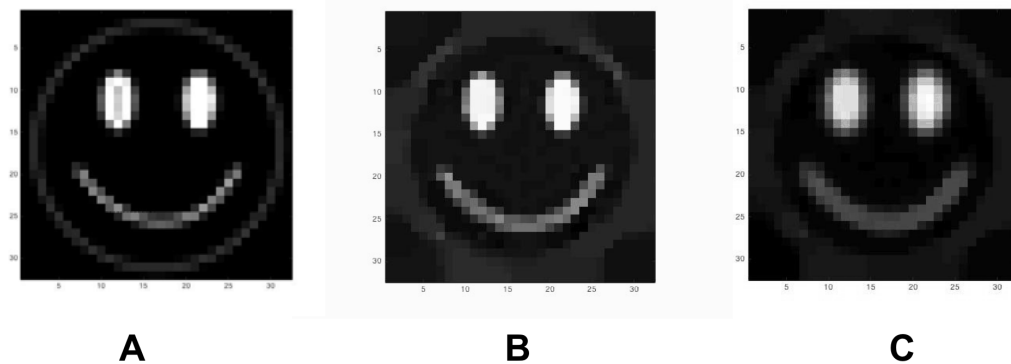
Figure 4.8: The original target used in the simulation tests **(A)**. The reconstructed images with no blur **(B)** and with blurred picture of the target sampled by blurred projection patterns **(C)**.

Experimental Results

Due to the limitations in communicating with the motion controller via the computer interface, different number of measurements were taken for each one of the

targets by manually operating the motion controller and to change the location of the beam over the target. Figure 4.9C shows the reconstructed image of the rectangular object in panel A of this Figure with no scattering material in the optical path. To sample this target, 65 measurements were taken and the reconstructed image has 67×67 pixels. This corresponds to the 1.4% sampling rate. To compare the reconstructed image and the original target, the picture of the rectangular object in Figure 4.5A was resized to 67×67 pixels to match the dimensions of the reconstructed image (Figure 4.9B). The reconstructed image of the rectangular target had 92% correlation with the original picture of this target taken by a regular camera.

A

B   **C**
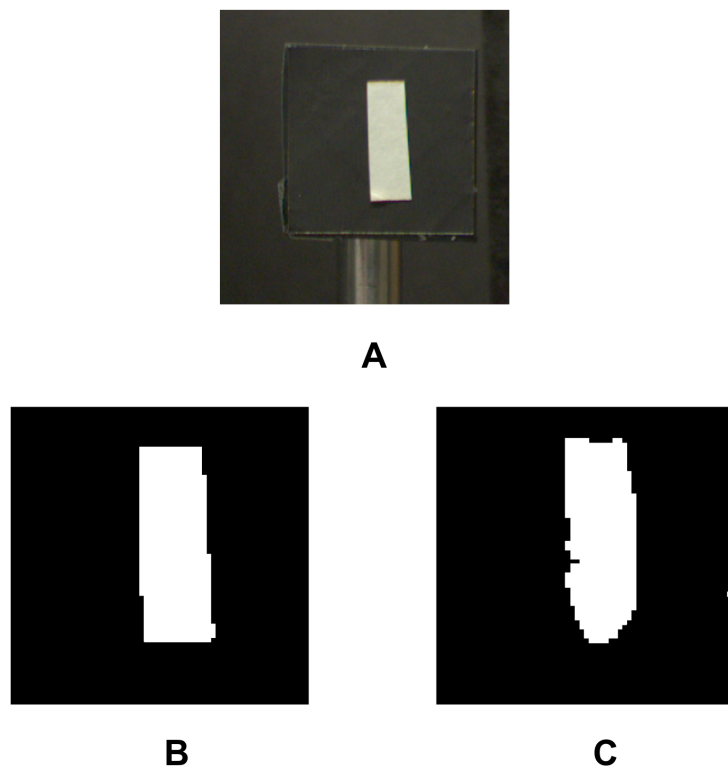
Figure 4.9: The rectangular object used as the target (**A**). The resized 67×67 pixel picture of the rectangular target taken by a regular camera (**B**) and the reconstructed image of this target without the presence of any scattering material (**C**). The reconstructed image in panel C has 92% correlation with the picture in panel B.

To sample the same rectangular object placed behind the clear light diffuser (Figure 4.10 B), 100 measurements corresponding to 4.9% sampling rate were taken to reconstruct a 45×45 image of the target. The reconstructed image and the resized picture of the original target are shown in Figure 4.10 C and D, respectively. The correlation for this reconstruction was 86%.
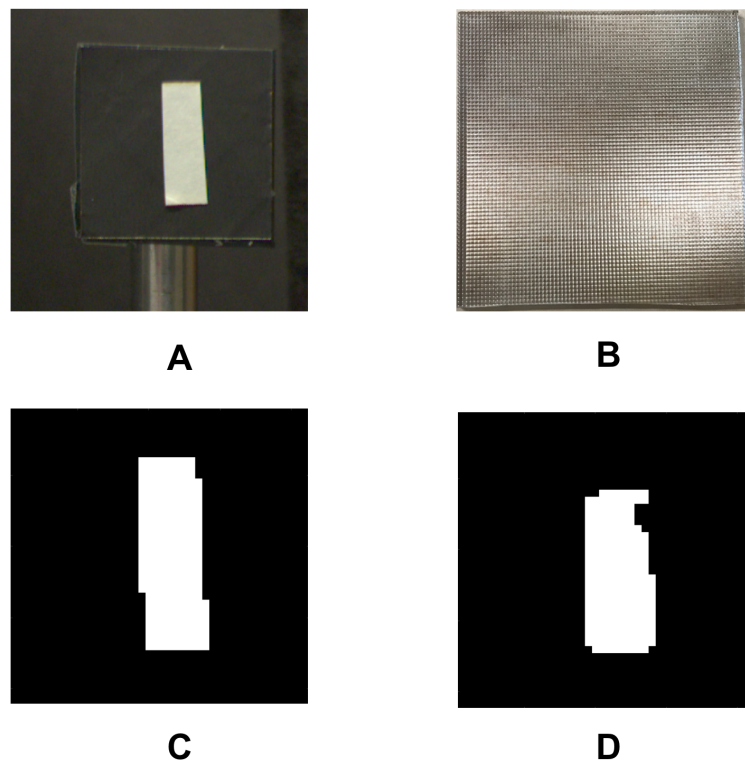
Figure 4.10: The rectangular object used as the target (**A**). The clear light diffuser used as scattering material (**B**). The resized 45×45 pixel picture of the rectangular target (**C**) and the reconstructed image of this target with presence of the scattering material (**B**). The reconstructed image has 86% correlation with the picture in panel C.

The second object that was used as a target, was the circle shaped object with the radius of 2.5 mm shown in Figure 4.11 A. Panel B in this Figure shows the image of this object taken by a regular camera and resized to 54×54 pixels to match the reconstructed image size. With 4.5% sampling rate, 122 measurements were taken to reconstruct the

image in panel C of the Figure 4.11. The images in panel B and C have 72% correlations.

A

B   **C**
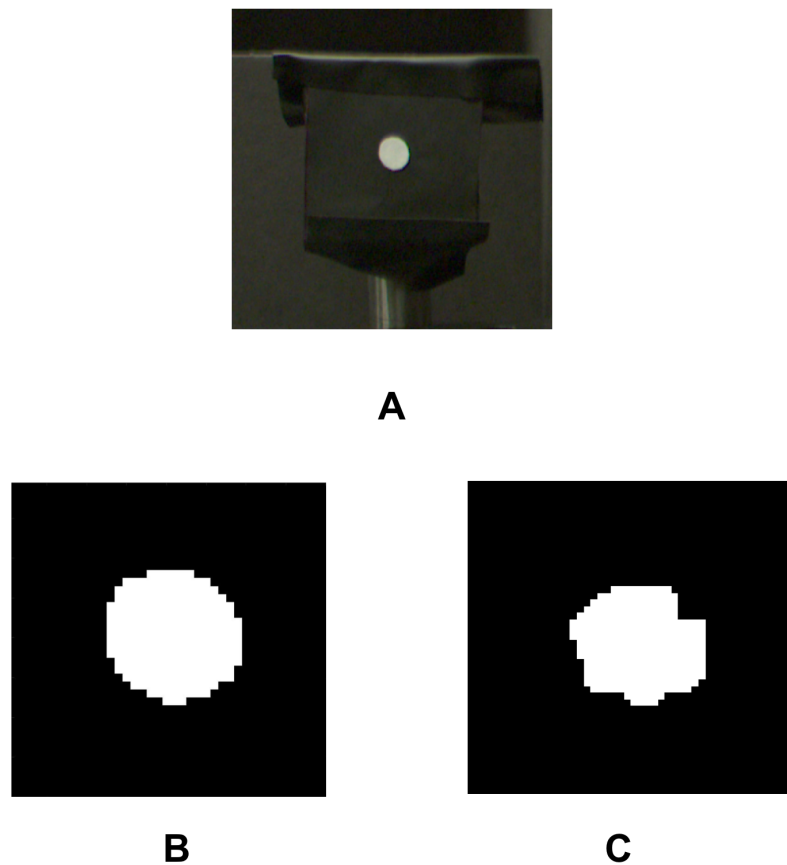
Figure 4.11: The circle shaped object used as the target (**A**). The resized 54×54 pixel picture of the circle shaped target taken by a regular camera (**B**) and the reconstructed image of this target without the presence of any scattering material (**C**). The reconstructed image in panel C has 72% correlation with the image in panel B.

The object with letter T as the third target was concealed behind a milk solution and sampled with the total of 120 projection patterns. Figure 4.12 A and B shows the target and the milk solution placed in front of the target. The image in panel C of this Figure shows the resized image with 61×61 pixels taken by the regular camera to be compared with the reconstructed image in panel D. The reconstructed image has 37% correlation with the original image of the target.
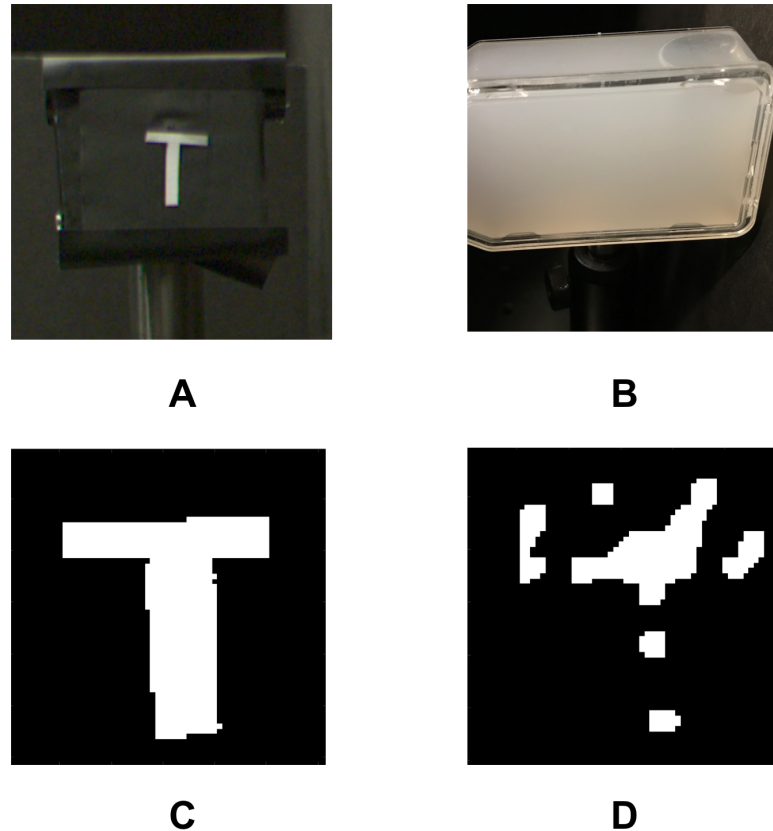
Figure 4.12: The T shaped object used as the target **(A)**. The milk solution used as the scattering material located in front of the target **(B)**. The resized 61×61 pixel picture of the target **(C)** and the reconstructed image of this target with presence of the scattering material **(B)**. The reconstructed image has 37% correlation with the image in panel C.

4.4   Discussion

The reconstructed images from the data acquired by projecting the new set of spatially encoded light fields on the objects both in presence of a scattering material and without it, shows promising proof of concept results. Furthermore, these results show the advantage of using light fields encoded by the Laguerre Gaussian modes as projection patterns to image through scattering in the reflective mode. Currently, the imaging through scattering using the diffused light is performed in transmissive mode, due to the low signal to noise ratio in the measured backscattered light. The spatially

encoded projection patterns were selected, in part, due to the resilience of the dark zone in the middle of these modes to diffusion in an inhomogeneous material. Consequently, the signal to noise ratio in the recorded backscattered light is higher when these modes are used in the projection patterns.

For the 6×19 mm^2 rectangular target, the reconstructed images had 92% and 86% correlation with the original picture of target taken by a regular camera with and without presence of the scattering material, respectively. For the circle shaped target with about 1/6 of the area of the rectangular target, the reconstructed image without the presence of a scattering material had 72% correlation with the original image of the target compared to the 92% for the case of the bigger rectangular target. The sampling rate for both of these measurements were very close; 4.9% corresponding to 100 measurements for the rectangular target and 4.5% corresponding to 122 measurements for the circle shaped target. The results prove the ability of the proposed projection patterns to generate an image of the object in the reflective mode. In addition, the number of measurements with this set of patterns are considerably less than the reported numbers for the case of using Hadamard matrix based projection patterns and CS image reconstruction algorithms [102]. The reconstructed image of the T shaped target with smaller feature sizes (1 mm compared to 6 mm in the rectangular target) and sampled in presence of a scattering material had 37% correlation with the original image of this target. This image was reconstructed under 3.2% sampling rate.

The effect of different photodetector signal integration times ranging from 1 to 8 seconds on the reconstructed images were tested and no solid improvement on the correlation of the reconstructed image and the original target was seen for longer integration times. The integration time was adjusted in the Labview program developed for controlling the photodetector and the camera.

In the future experiments, the authors will integrate different combination of the

LG modes into the projection patterns in order to improve the quality of the reconstructed images and image objects with smaller feature sizes. Since the LG modes are orthogonal to each other, a random combination of these modes in the projection patterns is expected to improve the quality of the image reconstructed by the compressive sensing algorithm [111].

4.5   Conclusions

A new set of projection patterns were proposed and utilized in sampling objects hidden behind scattering materials. In the reflective mode of imaging, the backscattered light was registered by a photodetector and the recorded signals were processed using l_1 magic compressive sensing recovery algorithm to reconstruct an image of the target. The reconstructed image of the target with 6 mm minimum feature size hidden behind a clear light diffuser had 86% correlation with the original image of the object taken by a regular camera without the presence of scattering. For the target with detail as small as 1 mm and hidden behind the milk container, the reconstructed image had 37% correlation with its original image taken by a regular camera with no scattering.

To further enhance the quality of the reconstructed images and to construct images of objects with smaller details, in the future, a random combination of different orders of LG modes will be incorporated in the projection patterns.

Acknowledgment

Chapter 5

Dissertation Conclusions and Future Directions

5.1 Final Conclusions

This dissertation develops and demonstrates the applications of the newly developed fiber optic based *in-vivo* sensor in spectral tissue detection and drug delivery. In addition, it demonstrates the design, development and application of spatially encoded light fields for generating 3D images of cancerous legions, reconstructing images of objects hidden inside scattering materials and optical trapping.

Optical detection of tissues in the percutaneous binary drainage procedure

The results of the Monte Carlo simulations and the experimental data collectively showed that the backscattering light from the target tissues sampled with spectrally encoded modulated light could reveal the nature of these tissues. A fiber optic based system was designed composed of two multimode fibers embedded in a biopsy needle that

is commonly used in the minimally invasive percutaneous binary drainage procedures. One of the fibers was used to transmit the modulated light into the tissue and the other one was used to record the backscattered light.

In the initial experiments, a broadband xenon light source was used to identify the light wavelengths that would result in distinct backscattering intensities from each of the tissues under study. In the subsequently developed prototype, the xenon light source was replaced with two red and green low power laser diodes. It was demonstrated that the ratios of backscattered intensities at these two wavelengths could be used to identify the tissue that the needle tip was located at. In addition, the developed prototype was able to detect an approaching interface with blood or bile while the needle advanced inside the liver parenchyma.

Spectral biopsy to seek areas with high breast tumor content

The fluence map of photons in the benign and malignant breast tissues was simulated using the Monte Carlo method at three wavelengths of light in the visible range and two wavelengths in the UV region. In the proposed system, one of the fiber optic cables embedded into the biopsy needle could be used to detect the backscattered photons reaching the tip of the needle inserted into the breast tissue. The wavelengths in the visible range were selected based on the distinctive absorption properties of the oxy and deoxy-hemoglobin in these wavelengths and the decrease in the hemoglobin oxygen saturation due to the excess need of oxygen by the tumor. On the other hand, the wavelengths in the UV region were chosen based on the useful criteria of the greater nucleus to cytoplasm ratio (N/C ratio) in malignant lesions, which imposes different absorption and scattering properties compared to the benign tissues in UV wavelengths.

The results of the simulations showed that the ratio of back scattered light at visible wavelengths and the UV region are different for a malignant legion and the benign

breast tissue. These distinctive ratios could be used to differentiate the high tumor content area and reduce the number of non viable biopsies.

Optical detection and activation of the Dox-PCB prodrug

In this dissertation the ability of the developed fiber optic based system in detecting the fluorescent chemotherapy agent, doxorubicin, at concentrations as low as 0.1 $\mu g/\mu l$ in pure water and in a liquid tissue phantom is demonstrated. This concentration is 7 times below the IC50 level for this drug in cell culture conditions, which indicates the developed system could detect therapeutically relevant concentrations of doxorubicin in tissue.

In addition, it has been demonstrated that the developed system can deliver the activating wavelength of light to the photocleavable prodrug DOX-PCB in a scattering tissue phantom and detect the shift in the spectrum of the activated prodrug indicating the release of the drug. The spectra of recorded fluorescent signals showed that the intensity of 565 nm peak increased relative to the 594 nm peak as the exposure time to the activating light increased. The ability of the system in releasing Dox from the Dox-PCB prodrug in a tissue phantom was confirmed by the subsequent HLPC analysis.

Using a biopsy needle in the developed system allows the fibers to be easily inserted into tissues for delivering the activating light and detecting the fluorescence signal at the tumor site, which makes it suitable for the future *in-vivo* studies.

Clinical imaging of tumors in resource-limited settings

In this dissertation the feasibility of using low-cost and user friendly systems for monitoring KS therapeutic response and upper airway tumor is investigated. The prototype for monitoring KS legion included a custom designed adaptor, the Lytro

commercial light field camera and an analytic software. The adaptor was designed such that it would allow a standardized setting with a fixed camera-to-object distance and angle to image the legions at different time points eliminating the day-to-day and person-to-person variations in image quality and to further facilitate monitoring the therapeutic response. To quantify the thickness of KS lesions as a means to study the response to treatment, a software was developed that was able to successfully measure relative changes in volume (for longitudinal follow-up) with an uncertainty of 4%. In the system for imaging an upper airway tumor, the Lytro Light Field camera was replaced by a tunable lens and a miniature camera with the control unit located outside the mouth. It has been demonstrated that the developed system was able to generate all-in focus images of legions located at different distances from the front lens in the upper airway regions.

Vectorial incident and focused field calculations

In this dissertation a novel method to rapidly calculate the phase pattern on the incident light fields required to generate the desired vectorial fields at the focus of high NA lenses is demonstrated. In this method a vectorial format of the Gerchberg-Saxon algorithm was introduced that was able to successfully calculate the required input fields for generating arbitrary polarization and intensity distributions at the foci of high NA lenses. The fast speed of this method; 25 ms for calculating a 128×128 pixel incident field, makes it suitable to dynamically change the focused field pattern in real-time.

In addition, in this work a novel focused field pattern encoded with spatially varying polarization and intensity distributions is introduced that could be used to generate translational movements on the trapped particles. The results of simulations demonstrated a linear state of polarization over the designed line at the center of the focused field indicating a potential linear force being applied on the trapped particles.

Spatially encoded optical fields to image through scattering

A reflective imaging setup is developed here that uses a novel set of spatially encoded light fields as illumination patterns to generate an image of the objects hidden behind scattering materials. The illumination patterns are encoded by optical modes with phase singularities. These modes are more robust against diffusion inside a scattering material which could increase the signal to noise ratio in the recorded backscattering light. Matlab simulations using the l_1 magic compressive sensing recovery algorithm were used to design a set of illumination patterns encoded by the Laguerre Gaussian modes that could generate an image of an object embedded inside a scattering material.

Different objects with variety of dimensions along with a few scattering materials were used to test the feasibility of the developed setup in generating an image of these objects. The reconstructed image of a 6×19 mm^2 rectangular target placed behind a clear light diffuser as the scattering material had 86% correlation with the image of this object taken with a regular camera without the presence of any scattering material. The developed setup was able to successfully reconstruct this image with only 100 measurements corresponding to the 4.9% sampling rate.

5.2   Future Directions

Future work involving the applications of the developed fiber optic based sensor will investigate the ability of this system in detecting the release of Dox-PCB prodrug *in-vivo*. In addition, the use of this system to acquire information on the concentration of the drug accumulated near a tumor site will be studied.

Future work involving the vectorial focused and incident field calculation will look at solving the reverse problem of estimating the required gray intensity level on the spatial light modulator to generate the calculated phase patterns for both components of the

incident light field without segmentation of the SLM. Moreover, nanoscale polarization probes will be developed to analyze the state of polarization at the objective focal plane. The ability of the proposed polarization variant focused line trap design in generating translational movements on the trapped nanoparticles and the size limit of these particles will be experimentally investigated.

Future work in the area of imaging objects embedded in a scattering material will look at improving the accuracy of the reconstructed pictures by using a combination of different orders of LG modes in each incident light pattern. In addition, the limit of sampling rate for generating images of objects with smaller feature sizes will be tested. The feasibility of generating 3D images by adding more photodetectors to the setup will be investigated. Furthermore, in the future, the photodetectors will be replaced by optical fibers to transform the developed setup to an endoscopic setup for *in-vivo* imaging.

Bibliography

[1] Y. Yang, E. J. Celmer, J. A. Koutcher, and R. Alfano, "Uv reflectance spectroscopy probes dna and protein changes in human breast tissues," *Journal of clinical laser medicine & surgery*, vol. 19, no. 1, pp. 35–39, 2001.

[2] K. J. Zuzak, M. D. Schaeberle, M. T. Gladwin, R. O. Cannon, and I. W. Levin, "Noninvasive determination of spatially resolved and time-resolved tissue perfusion in humans during nitric oxide inhibition and inhalation by use of a visible-reflectance hyperspectral imaging technique," *Circulation*, vol. 104, no. 24, pp. 2905–2910, 2001.

[3] R. A. Baum and S. Baum, "Interventional radiology: a half century of innovation," *Radiology*, vol. 273, no. 2S, pp. S75–S91, 2014.

[4] D. Broermann, S. Xie, K. Nephew, and W. Pope, "Effects of the oviduct and wheat germ agglutinin on enzymatic digestion of porcine zona pellucidae," *Journal of animal science*, vol. 67, no. 5, pp. 1324–1329, 1989.

[5] C. Lubawy and N. Ramanujam, "Endoscopically compatible near-infrared photon migration probe," *Optics letters*, vol. 29, no. 17, pp. 2022–2024, 2004.

[6] A. M. Zysk, F. T. Nguyen, E. J. Chaney, J. G. Kotynek, U. J. Oliphant, F. J. Bellafiore, P. A. Johnson, K. M. Rowland, and S. A. Boppart, "Clinical feasibility of microscopically-guided breast needle biopsy using a fiber-optic probe with computer-aided detection," *Technology in cancer research & treatment*, vol. 8, no. 5, pp. 315–321, 2009.

[7] J. R. Mourant and I. J. Bigio, "Elastic-scattering spectroscopy and diffuse reflectance," in *Biomedical Photonics Handbook*, CRC Press, 2003.

[8] S. A. Prahl, M. Keijzer, S. L. Jacques, and A. J. Welch, "A monte carlo model of light propagation in tissue," *Dosimetry of laser radiation in medicine and biology*, vol. 5, pp. 102–111, 1989.

[9] J.-P. Ritz, A. Roggan, C. Isbert, G. Müller, H. J. Buhr, and C.-T. Germer, "Optical properties of native and coagulated porcine liver tissue between 400 and 2400 nm," *Lasers in surgery and medicine*, vol. 29, no. 3, pp. 205–212, 2001.

[10] D. J. Faber, E. G. Mik, M. C. Aalders, and T. G. van Leeuwen, "Oxygen saturation dependent index of refraction of hemoglobin solutions assessed by oct," in *Biomedical Optics 2003*, pp. 271–281, International Society for Optics and Photonics, 2003.

[11] Z. Qian, S. S. Victor, Y. Gu, C. A. Giller, and H. Liu, "look-ahead distance of a fiber probe used to assist neurosurgery: Phantom and monte carlo study," *Optics express*, vol. 11, no. 16, pp. 1844–1855, 2003.

[12] C. E. DeSantis, S. A. Fedewa, A. Goding Sauer, J. L. Kramer, R. A. Smith, and A. Jemal, "Breast cancer statistics, 2015: Convergence of incidence rates between black and white women," *CA: a cancer journal for clinicians*, vol. 66, no. 1, pp. 31–42, 2016.

[13] D. Jelovac and L. A. Emens, "Her2-directed therapy for metastatic breast cancer," *Oncology*, vol. 27, no. 3, p. 166, 2013.

[14] N. Pathmanathan and R. L. Balleine, "Ki67 and proliferation in breast cancer," *Journal of clinical pathology*, pp. jclinpath–2012, 2013.

[15] S. Fantini and A. Sassaroli, "Near-infrared optical mammography for breast cancer detection with intrinsic contrast," *Annals of biomedical engineering*, vol. 40, no. 2, pp. 398–407, 2012.

[16] P. Held, "Application note for nucleic acid purity assessment using a260/a280 ratios," 1995.

[17] A. Gabizon, H. Shmeeda, and Y. Barenholz, "Pharmacokinetics of pegylated liposomal doxorubicin," *Clinical pharmacokinetics*, vol. 42, no. 5, pp. 419–436, 2003.

[18] A. Bao, B. Goins, R. Klipper, G. Negrete, and W. T. Phillips, "Direct 99mtc labeling of pegylated liposomal doxorubicin (doxil) for pharmacokinetic and non-invasive imaging studies," *Journal of Pharmacology and Experimental Therapeutics*, vol. 308, no. 2, pp. 419–425, 2004.

[19] I. Judson, J. A. Radford, M. Harris, J.-Y. Blay, Q. Van Hoesel, A. Le Cesne, A. Van Oosterom, M. Clemons, C. Kamby, C. Hermans, and J. Whittaker, "Randomised phase ii trial of pegylated liposomal doxorubicin (doxil®/caelyx®) versus doxorubicin in the treatment of advanced or metastatic soft tissue sarcoma: a study by the eortc soft tissue and bone sarcoma group," *European Journal of Cancer*, vol. 37, no. 7, pp. 870–877, 2001.

[20] W. A. Denny, "Prodrug strategies in cancer therapy," *European journal of medicinal chemistry*, vol. 36, no. 7, pp. 577–595, 2001.

[21] W. A. Denny, "Tumor-activated prodrugsa new approach to cancer therapy," *Cancer investigation*, vol. 22, no. 4, pp. 604–619, 2004.

[22] G. Minotti, P. Menna, E. Salvatorelli, G. Cairo, and L. Gianni, "Anthracyclines: molecular advances and pharmacologic developments in antitumor activity and cardiotoxicity," *Pharmacological reviews*, vol. 56, no. 2, pp. 185–229, 2004.

[23] S. Ibsen, E. Zahavy, W. Wrasidlo, T. Hayashi, J. Norton, Y. Su, S. Adams, and S. Esener, "Localized in vivo activation of a photoactivatable doxorubicin prodrug in deep tumor tissue," *Photochemistry and photobiology*, vol. 89, no. 3, pp. 698–708, 2013.

[24] S. Ibsen, E. Zahavy, W. Wrasdilo, M. Berns, M. Chan, and S. Esener, "A novel doxorubicin prodrug with controllable photolysis activation for cancer chemotherapy," *Pharmaceutical research*, vol. 27, no. 9, pp. 1848–1860, 2010.

[25] R. S. Cvetković and L. J. Scott, "Dexrazoxane," *Drugs*, vol. 65, no. 7, pp. 1005–1024, 2005.

[26] P. K. Singal and N. Iliskovic, "Doxorubicin-induced cardiomyopathy," *New England Journal of Medicine*, vol. 339, no. 13, pp. 900–905, 1998.

[27] S. Ibsen, Y. Su, J. Norton, E. Zahavy, T. Hayashi, S. Adams, W. Wrasidlo, and S. Esener, "Extraction protocol and mass spectrometry method for quantification of doxorubicin released locally from prodrugs in tumor tissue," *Journal of Mass Spectrometry*, vol. 48, no. 7, pp. 768–773, 2013.

[28] R. D. Olson and P. S. Mushlin, "Doxorubicin cardiotoxicity: analysis of prevailing hypotheses.," *The FASEB journal*, vol. 4, no. 13, pp. 3076–3086, 1990.

[29] L. F. Tietze, M. Neumann, T. Möllers, R. Fischer, K.-H. Glüsenkamp, M. F. Rajewsky, and E. Jähde, "Proton-mediated liberation of aldophosphamide from a nontoxic prodrug: a strategy for tumor-selective activation of cytocidal drugs," *Cancer research*, vol. 49, no. 15, pp. 4179–4184, 1989.

[30] J. M. Brown and W. R. Wilson, "Exploiting tumour hypoxia in cancer treatment," *Nature Reviews Cancer*, vol. 4, no. 6, pp. 437–447, 2004.

[31] K. Breistøl, H. Hendriks, D. Berger, S. Langdon, H. Fiebig, and O. Fodstad, "The antitumour activity of the prodrug n-l-leucyl-doxorubicin and its parent compound doxorubicin in human tumour xenografts," *European Journal of Cancer*, vol. 34, no. 10, pp. 1602–1606, 1998.

[32] A. Gopin, S. Ebner, B. Attali, and D. Shabat, "Enzymatic activation of second-generation dendritic prodrugs: conjugation of self-immolative dendrimers with poly (ethylene glycol) via click chemistry," *Bioconjugate chemistry*, vol. 17, no. 6, pp. 1432–1440, 2006.

[33] M. Shamis, H. N. Lode, and D. Shabat, "Bioactivation of self-immolative dendritic prodrugs by catalytic antibody 38c2," *Journal of the American Chemical Society*, vol. 126, no. 6, pp. 1726–1731, 2004.

[34] J. W. Park, K. Hong, D. B. Kirpotin, G. Colbern, R. Shalaby, J. Baselga, Y. Shao, U. B. Nielsen, J. D. Marks, D. Moore, and D. Papahadjopoulos, "Anti-her2 immunoliposomes," *Clinical Cancer Research*, vol. 8, no. 4, pp. 1172–1181, 2002.

[35] P. Vaupel, F. Kallinowski, and P. Okunieff, "Blood flow, oxygen and nutrient supply, and metabolic microenvironment of human tumors: a review," *Cancer research*, vol. 49, no. 23, pp. 6449–6465, 1989.

[36] S. Baghdadchi, C. Chao, S. Esener, R. F. Mattrey, and M. A. Eghtedari, "Fiber sensor assisted in-vivo needle guidance for minimally invasive procedures (conference presentation)," in *SPIE BiOS*, pp. 100600X–100600X, International Society for Optics and Photonics, 2017.

[37] E. A. Chu and Y. J. Kim, "Laryngeal cancer: diagnosis and preoperative work-up," *Otolaryngologic Clinics of North America*, vol. 41, no. 4, pp. 673–695, 2008.

[38] C. H. Shatney, R. D. Brunner, and T. Q. Nguyen, "The safety of orotracheal intubation in patients with unstable cervical spine fracture or high spinal cord injury," *The American journal of surgery*, vol. 170, no. 6, pp. 676–680, 1995.

[39] T. C. Mort, "Emergency tracheal intubation: complications associated with repeated laryngoscopic attempts," *Anesthesia & Analgesia*, vol. 99, no. 2, pp. 607–613, 2004.

[40] laryngoscopy, "indirectlaryngoscopy."

[41] laryngoscopy, "directlaryngoscopy."

[42] combinezm Inc., "combinezm."

[43] A. Swager, W. Curvers, and J. Bergman, "Diagnosis by endoscopy and advanced imaging," *Best Practice & Research Clinical Gastroenterology*, vol. 29, no. 1, pp. 97–111, 2015.

[44] R. Kiesslich, M. Goetz, A. Hoffman, and P. R. Galle, "New imaging techniques and opportunities in endoscopy. nature reviews gastroenterology and hepatology, vol. 8, no. 10," 2011.

[45] P. Urquhart, R. DaCosta, and N. Marcon, "Endoscopic mucosal imaging of gastrointestinal neoplasia in 2013," *Current gastroenterology reports*, vol. 15, no. 7, p. 330, 2013.

[46] J. P. Kassirer, "Images in clinical medicine," 1992.

[47] H. J. Chang and P. B. Fontanarosa, "Introducing the jama clinical challenge," *JAMA*, vol. 305, no. 18, pp. 1910–1910, 2011.

[48] S. E. Krown, C. Metroka, and J. Wernz, "Kaposi's sarcoma in the acquired immune deficiency syndrome: a proposal for uniform evaluation, response, and staging criteria. aids clinical trials group oncology committee.," *Journal of Clinical Oncology*, vol. 7, no. 9, pp. 1201–1207, 1989.

[49] T. S. Uldrick, K. M. Wyvill, P. Kumar, D. O'Mahony, W. Bernstein, K. Aleman, M. N. Polizzotto, S. M. Steinberg, S. Pittaluga, V. Marshall, and D. Whitby, "Phase ii study of bevacizumab in patients with hiv-associated kaposi's sarcoma receiving antiretroviral therapy," *Journal of Clinical Oncology*, vol. 30, no. 13, pp. 1476–1483, 2012.

[50] D. O'Mahony, A. H. Gandjbakche, M. Hassan, A. Vogel, and R. Yarchoan, "Imaging techniques for kaposi's sarcoma," *Journal of HIV therapy*, vol. 13, no. 3, pp. 65–71, 2008.

[51] J. Nayler, "Clinical photography: a guide for the clinician," *Journal of postgraduate medicine*, vol. 49, no. 3, p. 256, 2003.

[52] P. Persichetti, P. Simone, M. Langella, G. F. Marangi, and C. Carusi, "Digital photography in plastic surgery: how to achieve reasonable standardization outside a photographic studio," *Aesthetic plastic surgery*, vol. 31, no. 2, pp. 194–200, 2007.

[53] C. Barut and H. Ertilav, "Guidelines for standard photography in gross and clinical anatomy," *Anatomical sciences education*, vol. 4, no. 6, pp. 348–356, 2011.

[54] R. Ng, M. Levoy, M. Brédif, G. Duval, M. Horowitz, and P. Hanrahan, "Light field photography with a hand-held plenoptic camera," *Computer Science Technical Report CSTR*, vol. 2, no. 11, pp. 1–11, 2005.

[55] T. Georgiev, Z. Yu, A. Lumsdaine, and S. Goma, "Lytro camera technology: theory, algorithms, performance analysis," in *Proc. SPIE*, vol. 8667, p. 86671J, 2013.

[56] T. E. Bishop and P. Favaro, "The light field camera: Extended depth of field, aliasing, and superresolution," *IEEE Transactions on Pattern Analysis and Machine Intelligence*, vol. 34, no. 5, pp. 972–986, 2012.

[57] B. I, "A machine that makes cameras: The aesthetics of the lytro," 1999.

[58] E. H. Adelson and J. Y. Wang, "Single lens stereo with a plenoptic camera," *IEEE transactions on pattern analysis and machine intelligence*, vol. 14, no. 2, pp. 99–106, 1992.

[59] L. Novakova-Marcincinova, J. Novak-Marcincin, J. Barna, and J. Torok, "Special materials used in fdm rapid prototyping technology application," in *Intelligent Engineering Systems (INES), 2012 IEEE 16th International Conference on*, pp. 73–76, IEEE, 2012.

[60] lfp reader, "lfp-reader 2.0.0."

[61] lfpviewer, "Simple opengl lfp viewer," 1999.

[62] C. Carrilho, J. Ferro, C. Lorenzoni, T. Sultane, C. Silva-Matos, and N. Lunet, "A contribution for a more accurate estimation of the incidence of kaposi sarcoma in mozambique," *International journal of cancer*, vol. 132, no. 4, pp. 988–989, 2013.

[63] E. Letang, J. J. Lewis, M. Bower, A. Mosam, M. Borok, T. B. Campbell, D. Naniche, T. Newsom-Davis, F. Shaik, S. Fiorillo, and J. Miro, "Immune reconstitution inflammatory syndrome associated with kaposi sarcoma: higher incidence and mortality in africa than in the uk," *Aids*, vol. 27, no. 10, pp. 1603–1613, 2013.

[64] S. E. Krown, "Treatment strategies for kaposi sarcoma in sub-saharan africa: challenges and opportunities," *Current opinion in oncology*, vol. 23, no. 5, p. 463, 2011.

[65] S. Menzies, J. Emery, M. Staples, S. Davies, B. McAvoy, J. Fletcher, K. Shahid, G. Reid, M. Avramidis, A. Ward, and R. Burton, "Impact of dermoscopy and short-term sequential digital dermoscopy imaging for the management of pigmented lesions in primary care: a sequential intervention trial," *British Journal of Dermatology*, vol. 161, no. 6, pp. 1270–1277, 2009.

[66] B. Preim and C. P. Botha, *Visual Computing for Medicine: Theory, Algorithms, and Applications*. Newnes, 2013.

[67] M. A. Gavrielides, L. M. Kinnard, K. J. Myers, and N. Petrick, "Noncalcified lung nodules: Volumetric assessment with thoracic ct 1," *Radiology*, vol. 251, no. 1, pp. 26–37, 2009.

[68] A. Miller, B. Hoogstraten, M. Staquet, and A. Winkler, "Reporting results of cancer treatment," *cancer*, vol. 47, no. 1, pp. 207–214, 1981.

[69] P. Therasse, S. G. Arbuck, E. A. Eisenhauer, J. Wanders, R. S. Kaplan, L. Rubinstein, J. Verweij, M. Van Glabbeke, A. T. van Oosterom, M. C. Christian, and S. Gwyther, "New guidelines to evaluate the response to treatment in solid tumors," *Journal of the National Cancer Institute*, vol. 92, no. 3, pp. 205–216, 2000.

[70] E. Eisenhauer, P. Therasse, J. Bogaerts, L. Schwartz, D. Sargent, R. Ford, J. Dancey, S. Arbuck, S. Gwyther, M. Mooney, and L. Rubinstein, "New response evaluation criteria in solid tumours: revised recist guideline (version 1.1)," *European journal of cancer*, vol. 45, no. 2, pp. 228–247, 2009.

[71] T. Tirkes, M. A. Hollar, M. Tann, M. D. Kohli, F. Akisik, and K. Sandrasegaran, "Response criteria in oncologic imaging: review of traditional and new criteria," *Radiographics*, vol. 33, no. 5, pp. 1323–1341, 2013.

[72] N. Petrick, H. J. G. Kim, D. Clunie, K. Borradaile, R. Ford, R. Zeng, M. A. Gavrielides, M. F. McNitt-Gray, Z. J. Lu, C. Fenimore, and B. Zhao, "Comparison of 1d, 2d, and 3d nodule sizing methods by radiologists for spherical and complex nodules on thoracic ct phantom images," *Academic radiology*, vol. 21, no. 1, pp. 30–40, 2014.

[73] J. M. McGinnis, L. Stuckhardt, R. Saunders, and M. Smith, *Best care at lower cost: the path to continuously learning health care in America.* National Academies Press, 2013.

[74] A. Qaseem, P. Alguire, P. Dallas, L. E. Feinberg, F. T. Fitzgerald, C. Horwitch, L. Humphrey, R. LeBlond, D. Moyer, J. G. Wiese, and S. Weinberger, "Appropriate use of screening and diagnostic tests to foster high-value, cost-conscious care," *Annals of internal medicine*, vol. 156, no. 2, pp. 147–149, 2012.

[75] G. Argenziano, L. Cerroni, I. Zalaudek, S. Staibano, R. Hofmann-Wellenhof, N. Arpaia, R. M. Bakos, B. Balme, J. Bandic, R. Bandelloni, and A. Brunasso, "Accuracy in melanoma detection: a 10-year multicenter survey," *Journal of the American Academy of Dermatology*, vol. 67, no. 1, pp. 54–59, 2012.

[76] P. Carli, V. De Giorgi, E. Crocetti, F. Mannone, D. Massi, A. Chiarugi, and B. Giannotti, "Improvement of malignant/benign ratio in excised melanocytic lesions in the dermoscopy era: a retrospective study 1997–2001," *British Journal of Dermatology*, vol. 150, no. 4, pp. 687–692, 2004.

[77] A. Ashkin, J. M. Dziedzic, J. E. Bjorkholm, and S. Chu, "Observation of a single-beam gradient force optical trap for dielectric particles," *Opt. Lett.*, vol. 11, pp. 288–290, May 1986.

[78] M.-y. Wu, D.-x. Ling, L. Ling, W. Li, and Y.-q. Li, "Stable optical trapping and sensitive characterization of nanostructures using standing-wave raman tweezers," *Scientific Reports*, vol. 7, 2017.

[79] Y.-C. Li, H.-B. Xin, H.-X. Lei, L.-L. Liu, Y.-Z. Li, Y. Zhang, and B.-J. Li, "Manipulation and detection of single nanoparticles and biomolecules by a photonic nanojet," *Light: Science & Applications*, vol. 5, no. 12, p. e16176, 2016.

[80] R. Agarwal, K. Ladavac, Y. Roichman, G. Yu, C. M. Lieber, and D. G. Grier, "Manipulation and assembly of nanowires with holographic optical traps," *Optics Express*, vol. 13, no. 22, pp. 8906–8912, 2005.

[81] M. Padgett and R. Bowman, "Tweezers with a twist," *Nature Photonics*, vol. 5, no. 6, pp. 343–348, 2011.

[82] J. E. Curtis, B. A. Koss, and D. G. Grier, "Dynamic holographic optical tweezers," *Optics communications*, vol. 207, no. 1, pp. 169–175, 2002.

[83] G. Sinclair, P. Jordan, J. Courtial, M. Padgett, J. Cooper, and Z. J. Laczik, "Assembly of 3-dimensional structures using programmable holographic optical tweezers," *Optics Express*, vol. 12, no. 22, pp. 5475–5480, 2004.

[84] E. Wolf, "Electromagnetic diffraction in optical systems. i. an integral representation of the image field," in *Proceedings of the Royal Society of London A: Mathematical, Physical and Engineering Sciences*, vol. 253, pp. 349–357, The Royal Society, 1959.

[85] M. Leutenegger, R. Rao, R. A. Leitgeb, and T. Lasser, "Fast focus field calculations," *Optics express*, vol. 14, no. 23, pp. 11277–11291, 2006.

[86] J. Lin, O. Rodríguez-Herrera, F. Kenny, D. Lara, and J. Dainty, "Fast vectorial calculation of the volumetric focused field distribution by using a three-dimensional fourier transform," *Optics express*, vol. 20, no. 2, pp. 1060–1069, 2012.

[87] E. J. Haellstig, L. Sjoeqvist, and M. Lindgren, "Characterization of a liquid crystal spatial light modulator for beam steering," in *High-Power Lasers and Applications*, pp. 187–196, International Society for Optics and Photonics, 2002.

[88] R. L. Eriksen, P. C. Mogensen, and J. Glückstad, "Elliptical polarisation encoding in two dimensions using phase-only spatial light modulators," *Optics communications*, vol. 187, no. 4, pp. 325–336, 2001.

[89] U. Ruiz-Corona and V. Arrizon-Peña, "Characterization of twisted liquid crystal spatial light modulators," in *Sixth Symposium Optics in Industry*, pp. 642215–642215, International Society for Optics and Photonics, 2007.

[90] W.-F. Cheong, S. A. Prahl, and A. J. Welch, "A review of the optical properties of biological tissues," *IEEE journal of quantum electronics*, vol. 26, no. 12, pp. 2166–2185, 1990.

[91] G. Jarry, S. Ghesquiere, J. Maarek, F. Fraysse, S. Debray, and D. Laurent, "Imaging mammalian tissues and organs using laser collimated transillumination," *Journal of biomedical engineering*, vol. 6, no. 1, pp. 70–74, 1984.

[92] L. Jofre, M. S. Hawley, A. Broquetas, E. de Los Reyes, M. Ferrando, and A. R. Elias-Fuste, "Medical imaging with a microwave tomographic scanner," *IEEE Transactions on Biomedical Engineering*, vol. 37, no. 3, pp. 303–312, 1990.

[93] C. Hoyt, R. Richards-Kortum, B. Costello, B. Sacks, C. Kittrell, N. Ratliff, J. Kramer, and M. Feld, "Remote biomedical spectroscopic imaging of human artery wall," *Lasers in surgery and medicine*, vol. 8, no. 1, pp. 1–9, 1988.

[94] J. White, W. Amos, and M. Fordham, "An evaluation of confocal versus conventional imaging of biological structures by fluorescence light microscopy.," *The Journal of cell biology*, vol. 105, no. 1, pp. 41–48, 1987.

[95] K. Carlsson and N. Åslund, "Confocal imaging for 3-d digital microscopy," *Applied Optics*, vol. 26, no. 16, pp. 3232–3238, 1987.

[96] J. C. Jung and M. J. Schnitzer, "Multiphoton endoscopy," *Optics letters*, vol. 28, no. 11, pp. 902–904, 2003.

[97] D. R. Rivera, C. M. Brown, D. G. Ouzounov, I. Pavlova, D. Kobat, W. W. Webb, and C. Xu, "Compact and flexible raster scanning multiphoton endoscope capable of imaging unstained tissue," *Proceedings of the National Academy of Sciences*, vol. 108, no. 43, pp. 17598–17603, 2011.

[98] V. V. Tuchin and V. Tuchin, *Tissue optics: light scattering methods and instruments for medical diagnosis*, vol. 13. SPIE press Bellingham, 2007.

[99] J. F. De Boer, T. E. Milner, M. J. van Gemert, and J. S. Nelson, "Two-dimensional birefringence imaging in biological tissue by polarization-sensitive optical coherence tomography," *Optics letters*, vol. 22, no. 12, pp. 934–936, 1997.

[100] A. P. Mosk, A. Lagendijk, G. Lerosey, and M. Fink, "Controlling waves in space and time for imaging and focusing in complex media," *Nature photonics*, vol. 6, no. 5, pp. 283–292, 2012.

[101] O. Katz, P. Heidmann, M. Fink, and S. Gigan, "Non-invasive single-shot imaging through scattering layers and around corners via speckle correlations," *Nature photonics*, vol. 8, no. 10, pp. 784–790, 2014.

[102] V. Durán, P. Clemente, E. Irles, F. Soldevila, E. Tajahuerce, A. Rodríguez, P. Andrés, and J. Lancis, "Structured illumination enables image transmission through scattering media," in *Proc. SPIE*, vol. 9335, p. 93350V, 2015.

[103] M. F. Duarte, M. A. Davenport, D. Takbar, J. N. Laska, T. Sun, K. F. Kelly, and R. G. Baraniuk, "Single-pixel imaging via compressive sampling," *IEEE signal processing magazine*, vol. 25, no. 2, pp. 83–91, 2008.

[104] R. G. Baraniuk, "Compressive sensing [lecture notes]," *IEEE signal processing magazine*, vol. 24, no. 4, pp. 118–121, 2007.

[105] J. Ma, "Single-pixel remote sensing," *IEEE Geoscience and Remote Sensing Letters*, vol. 6, no. 2, pp. 199–203, 2009.

[106] J. H. Shapiro, "Computational ghost imaging," *Physical Review A*, vol. 78, no. 6, p. 061802, 2008.

[107] Z. Zhang, X. Ma, and J. Zhong, "Single-pixel imaging by means of fourier spectrum acquisition," *Nature communications*, vol. 6, p. 6225, 2015.

[108] S. S. Welsh, M. P. Edgar, R. Bowman, P. Jonathan, B. Sun, and M. J. Padgett, "Fast full-color computational imaging with single-pixel detectors," *Optics express*, vol. 21, no. 20, pp. 23068–23074, 2013.

[109] B. Sun, M. P. Edgar, R. Bowman, L. E. Vittert, S. Welsh, A. Bowman, and M. Padgett, "3d computational imaging with single-pixel detectors," *Science*, vol. 340, no. 6134, pp. 844–847, 2013.

[110] S. Popoff, G. Lerosey, R. Carminati, M. Fink, A. Boccara, and S. Gigan, "Measuring the transmission matrix in optics: an approach to the study and control of light propagation in disordered media," *Physical review letters*, vol. 104, no. 10, p. 100601, 2010.

[111] E. J. Candès and M. B. Wakin, "An introduction to compressive sampling," *IEEE signal processing magazine*, vol. 25, no. 2, pp. 21–30, 2008.

[112] W. Wang, R. Gozali, T. A. Nguyen, and R. Alfano, "Propagation and transmission of optical vortex beams through turbid scattering wall with orbital angular momentums," in *SPIE BiOS*, pp. 931805–931805, International Society for Optics and Photonics, 2015.

[113] W. Wang, R. Gozali, L. Shi, L. Lindwasser, and R. Alfano, "Deep transmission of laguerre–gaussian vortex beams through turbid scattering media," *Optics letters*, vol. 41, no. 9, pp. 2069–2072, 2016.

[114] L. Allen, M. W. Beijersbergen, R. Spreeuw, and J. Woerdman, "Orbital angular momentum of light and the transformation of laguerre-gaussian laser modes," *Physical Review A*, vol. 45, no. 11, p. 8185, 1992.

[115] B. Cochenour, K. Morgan, K. Miller, E. Johnson, K. Dunn, and L. Mullen, "Propagation of modulated optical beams carrying orbital angular momentum in turbid water," *Applied optics*, vol. 55, no. 31, pp. C34–C38, 2016.

[116] E. Candes and J. Romberg, "l1magic: a collection of matlab routines for solving the convex optimization programs central to compressive sampling," *Avaliable: www. acm. caltech. edu/l1magic*, 2006.

[117] L. Shi and R. R. Alfano, *Deep Imaging in Tissue and Biomedical Materials: Using Linear and Nonlinear Optical Methods*. CRC Press, 2017.

[118] S. G. Narasimhan, M. Gupta, C. Donner, R. Ramamoorthi, S. K. Nayar, and H. W. Jensen, "Acquiring scattering properties of participating media by dilution," in *ACM Transactions on Graphics (TOG)*, vol. 25, pp. 1003–1012, ACM, 2006.

[119] R. Pijnappel, M. Van den Donk, R. Holland, W. T. M. Mali, J. Peterse, J. Hendriks, and P. Peeters, "Diagnostic accuracy for different strategies of image-guided breast intervention in cases of nonpalpable breast lesions," *British journal of cancer*, vol. 90, no. 3, p. 595, 2004.

[120] M. Joshi, S. J. Reddy, M. Nanavidekar, J. P. Russo, A. V. Russo, and R. Pathak, "Core biopsies of the breast: Diagnostic pitfalls," *Indian Journal of Pathology and Microbiology*, vol. 54, no. 4, p. 671, 2011.

[121] K. K. Shung and G. A. Thieme, *Ultrasonic scattering in biological tissues*. CRC press, 1992.

[122] O. J. J. Y.-S. Shao, Y.-W. Q. X.-S. Hua, and H.-Q. W. Dong-Hai, "Scattering of the laguerre-gaussian beam by a homogeneous spheroid," *Acta Physica Sinica*, vol. 11, p. 036, 2013.

[123] J. Romberg, "L1-magic," 2008.

[124] N. Ghosh, S. Mohanty, S. Majumder, and P. Gupta, "Measurement of optical transport properties of normal and malignant human breast tissue," *Applied Optics*, vol. 40, no. 1, pp. 176–184, 2001.